Intermittency in reversible martensitic transformations

Noemi Barrera

N° d'ordre : D. U : 2562
E D S P I C : 693

UNIVERSITÉ BLAISE PASCAL - CLERMONT II

ECOLE DOCTORALE
SCIENCES POUR L'INGÉNIEUR DE CLERMONT-FERRAND

T h è s e

Présentée par

NOEMI BARRERA

pour obtenir le grade de

DOCTEUR D'UNIVERSITÉ

SPECIALITE : MÉCANIQUE DU SOLIDE

Intermittency in Reversible Martensitic Transformations

Soutenue publiquement le 26 Mars 2015 devant le jury :

Prof. Eduard Vives, Universitat de Barcelona, Président
Dir. Rech. François Hild, CNRS, LMT Cachan, Rapporteur
Dr. HDR Giuseppe Puglisi, Politecnico di Bari, Rapporteur
Prof. Giovanni Zanzotto, Università di Padova, Examinateur
Prof. Xavier Balandraud, IFMA, Directeur de thèse
Prof. Michel Grédiac, Université Blaise Pascal, Co-encadrant
Prof. Paolo Biscari, Politecnico di Milano, Directeur de thèse

Abstract

This thesis deals with the characterization of Martensitic Transformations (MT) that are first order phase transitions among different solid states with different crystalline structures. These transitions are at the basis of the behavior of a class of smart materials, called *Shape Memory Alloys* (SMA).

This work combines an experimental study of a mechanically-induced martensitic transformation in a Cu-Al-Be single crystal and a macroscopic model for the reproduction of permanent effects in cyclic temperature-induced and stress-induced transitions.

From the experimental point of view, the novelties are in the device that has been built and used for the test and in the full-field measurement technique at the basis of the data treatment. The especially designed gravity-based device allows for a uni-axial and uni-directional tensile test with slow loading rates. Simultaneously, the full-field measurement technique, known as *grid method*, provides high-resolution two-dimensional strain maps during all the transformation.

With all the data collected during the test, we characterize for the first time the two-dimensional strain intermittency in a number of ways, showing heavy-tailed distributions for the strain avalanching over almost six decades of magnitude.

In parallel, we develop a macroscopic mathematical model for the description of fatigue and permanent effects in several kinds of martensitic transformations. We show an easy way to calibrate the model parameters in the simple one-dimensional case. Moreover, we compare the numerical results with experimental data for different tests and specimens and obtain a good qualitative agreement.

Summary

Martensitic Transformations (MT) are solid-to-solid first order phase transitions between different crystalline microstructures that characterize an interesting class of smart materials called Shape Memory Alloys (SMAs). These metallic alloys were discovered around 1930s for the first time and are particularly interesting since they combine two peculiar effects: the *Shape Memory Effect* and the *Pseudo-Elasticity*. The Shape Memory Effect consists in storing the memory of a particular configuration and recover it after thermal or mechanical cycles. Conversely, Pseudo-Elasticity is the capability to reach high strain levels that are usually typical of rubbers and not of metals.
In this thesis we deal with the characterization of martensitic transformations by analyzing them from different points of view. The comprehension of how SMAs work is fundamental for many industrial applications and is still a wide open field of analysis.

Chapter 1 provides an idea of the theoretical basis for mathematical models of shape memory alloys. It starts with a short introduction on SMAs and on the basic ideas on martensitic transformations. Then, two different theoretical approaches are shown. On one hand, Crystallographic Theory of martensitic transformations is introduced. This theory is the starting point for several mathematical models that are interested in the microscopic scale of the material and some of the results of this theory will be used in Chapter 3 for a more detailed data analysis. On the other hand, SMAs can also be studied as macroscopic continua: this kind of approach is introduced at the end of the first chapter by explaining the Rajagopal's theory of dissipative processes.

In Chapter 2 we start dealing with the experimental part of the thesis. This chap-

ter explains the experimental setting and the methods used during our test, carried out at IFMA (Institut Français de Mécanique Avancée) laboratories in Clermont-Ferrand, France. The basic idea was to perform an experiment with simple external loading conditions and to obtain a significant amount of good resolution data. Indeed, our aim was to go deep into the analysis of the transformation, by measuring the details of the advancement of the transition, not only the macroscopic behavior. In order to do so, we decided to perform a tensile uni-axial and uni-directional test with free rotation allowed. We realized this goal by using an in-house designed device that guaranteed a constant loading direction with the use of slow loading rates, thus reducing inertial effects. Moreover, we employed a full-field measurement technique, known as *grid method*, to obtain two-dimensional high-resolution strain maps during all the test.
As regards the specimen that we tested, we had a quite complete crystallographic description of the material. This knowledge allowed us to analyze it deeply and to compare our results with previous tensile tests that had been carried out by using different loading devices.

In Chapter 3 we started the analysis of the strain maps obtained during the test, by looking at the overall behavior of the material. First of all, the comparison of our results with previous tests on the same specimen allowed us to point out some features of our testing device. Second, we can compare some experimental results with the theoretical estimates obtained in the first chapter and make some observation on the microscopic structure of the specimen during the test. Third, after a qualitative description of the transformation and of its different phases, we can start deducing some characteristic quantities, like the percentage of martensite or the vertical strain. These quantities are the first example of signal that seem to be continuous on the macroscopic scale but whose variation shows spikes and jumps.
This kind of behavior leads us to the main topic of this thesis, that is the presence of intermittency in the martensitic transformation.

What do we mean by using the term *intermittency*? We consider a phenomenon as intermittent when it takes place in a non-periodic or non-predictable way. In particular, the kind of intermittency in which we are interested is the one that is present for many different scales in the same phenomenon. This feature is called *self-similarity*. As it is possible to imagine, a self-similar phenomenon is such that it is similar to itself but on various scales. For example, this happens for earthquakes, from the biggest ones to the small movements of the earth crust, for fractals, landscapes, neuronal networks, lung

inflation and a really long list of phenomena in different fields and at different scales. Self-similarity can be very useful. On one hand, within the same phenomenon it enables us to focus on the overall behavior, instead of considering small and precise details that become negligible at bigger scales. On the other hand, it allows some comparisons among phenomena that are apparently very different but whose statistical behavior is the same. In this sense, we can think about understanding the phenomenon of earthquakes, whose spatial and temporal scales are very big, by studying a simpler and faster self-similar phenomenon.
Among all the phenomena which have been found to display intermittency and self-similarity there are also martensitic transformations in shape memory alloys (together with many other materials like superconductors, ferromagnets or porous media). This feature is particularly interesting because martensitic transitions are usually described as continuous phenomena while in practice it seems that, when looking at the details, the transition is not continuous but obtained as a sum of several avalanches of different dimension. The question is whether in our data there is this sort of intermittent behavior or not and, in case of positive answer, if we are able to quantitatively analyze it.

In Chapter 4 we characterize the martensitic transformation in our sample from a statistical viewpoint. We start by looking at the quantities that we introduced in the previous chapter, that is the martensite phase fraction and the vertical strain. We then continue by defining the concept of *avalanches* in two-dimensional strain maps and we statistically analyze their properties. We thus prove that the transformation actual occurs through intermittent events that span on several scales.
We provided a comparison between magnitude and size of the avalanches and a characterization of their statistical behavior by using also the Maximum Likelihood method. Moreover, we analyzed the non-stationarity of the transformation, by showing different statistical behaviors for different parts of the transformation.

We concluded the thesis by dealing with another kind of analysis of the martensitic transformation in SMAs. Instead of focusing on the intermittent behavior of the material, we focused on the presence of fatigue and plastic effects in the MT. Actually, many applications of shape memory alloys, like actuators or coronary stents, require a cyclical behavior which remains stable for quite long times. Thus, we abandoned the microscopic scale and we looked at the material as a macroscopic continua, by exploiting the theoretical background provided in the first chapter for Rajagopal's theory. We thus developed a model that is able to take into account for the arising of permanent effects

during the transformation without going into detail of the microstructure. We tested our numerical results, obtained by solving the model equations in the one-dimensional approximation, by comparing them with experimental results for temperature-induced and stress-induced transformations. Moreover, we showed the possibility to easily calibrate the model parameters for the different cases.
Thus, we provided a different kind of analysis of the martensitic transformation through a different approach than the microscopic one used for the detection of intermittency.
All these different points of view can be used when dealing with martensitic transformations, in the attempt to enhance our knowledge in this field, that is exactly the aim of this work.

Résumé

Les Transformation Martensitiques (TM) sont des transitions du premier ordre entre des phases cristallines qui caractérisent une classe intéressante de matériaux intelligents, les Alliages à Mémoire de Forme (AMF). Ces alliages métalliques furent découverts dans les année 1930 environ. Ils sont surtout intéressants car ils combinent deux effets particuliers : l'effet de mémoire de forme et la pseudo-élasticité. L'effet mémoire de forme consiste à mémoriser une configuration particulière et la retrouver après des cycles thermiques ou mécaniques. La Pseudo-Elasticité consiste à rejoindre des niveaux de déformation très grands qui sont, en général, plus typiques du caoutchouc que des métaux.

Dans cette thèse, nous avons traité la caractérisation des transformations martensitiques en analysant points de vue différents. La compréhension du fonctionnement des AMFs est fondamentale pour plusieurs types d'applications industrielles. Elle constitue encore un domaine de recherche très ouvert.

Le Chapitre 1 donne une idée des bases théoriques pour les modèles mathématiques sous-jacents aux alliages à mémoire de forme. Il commence avec une brève introduction sur les AMFs, puis se poursuit sur les bases des transformations martensitiques. Nous montrons ensuite deux études théoriques différentes. Nous présentons d'abord la théorie crystallographique des transformations martensitiques. Cette théorie est le point de départ pour plusieurs modèles mathématiques qui sont intéressants à l'échelle microscopique du matériau. Des résultats de cette théorie sont ensuite utilisés dans le Chapitre 3 pour une analyse plus détaillée. Les AMFs peuvent aussi être étudiées

comme des continuums macroscopiques : cette stratégie est ensuite expliquée dans la partie finale du premier chapitre, avec la théorie de Rajagopal sur les processus avec dissipation.

Dans le Chapitre 2 nous commençons à traiter la partie expérimentale de la thèse. Ce chapitre explique divers réglages expérimentaux et les méthodes utilisées pendant l'essai. Cette partie du travail a été réalisée à l'IFMA (Institut Français de Mécanique Avancée) à Clermont-Ferrand, France. L'idée de base était de faire un essai avec des conditions de chargement très simples et d'obtenir en même temps une quantité significative de données avec une bonne résolution, tant spatiale, temporelle que de mesure. En fait, notre objectif était d'aller en profondeur dans l'analyse de la transformation en considérant les détails de la transition, et pas simplement d'analyser le comportement macroscopique. Pour cette raison, nous avons décidé de réaliser un essai uni-axial, avec un système de préhension de l'éprouvette qui assure un degré de liberté de rotation à ses extrémités.
Nous avons élaboré pour cela une nouvelle machine qui garantit une direction de chargement constant, avec l'application de taux de chargement très bas qui réduisent les effets inertiels. De plus, nous avons utilisé une technique de mesure de champs cinématiques appelée *méthode de la grille* pour obtenir des cartes bi-dimensionnelles des composantes planes du tenseurs des déformations pendant toute la transformation.
En ce qui concerne l'échantillon qui a été étudié, nous avions une description cristallographique presque complète du matériau. Cette connaissance nous a permis de réaliser une analyse en profondeur des données et de comparer nos résultats avec d'autres essais qui avaient été réalisés précédemment avec le même échantillon, mais avec des machines d'essai différentes.

Dans le Chapitre 3 nous analysons les cartes de déformation obtenues pendant l'essai, en nous concentrant sur le comportement global du matériau. La comparaison avec les essais précédents nous a d'abord aidés à souligner les caractéristiques de la machine utilisée. Nous avons ensuit pu comparer les résultats expérimentaux avec les estimations théoriques obtenues dans le premier chapitre, et faire des considérations sur la structure microscopique de l'échantillon pendant l'essai. Enfin, après une description qualitative de la transformation et de ses phases différentes, nous avons commencé à déduire des quantités caractéristiques comme le pourcentage de la phase martensitique ou la déformation verticale. Ces quantités sont le premier example de signal qui semble être continus à une échelle macroscopique, mais avec une variation qui montre des va-

riations brusques.
Ce comportement nous a amenés vers le sujet principal de cette thèse, à savoir la présence d'une intermittence dans la transformation martensitique.

Que voulons nous dire avec le terme ´´intermittence" ? Nous disons qu'un phénomène est intermittent s'il se produit d'une façon non-périodique et non-prévisible. En particulier, le type d'intermittence qui nous intéresse est une intermittence qui est présente à plusieurs échelles pour le même phénomène. Cette caractéristique s'appelle l'*auto-similarité* (self-similarity en anglais). Comme on peut l'imaginer, un phénomène auto-similaire est similaire à lui-même, mais sur des échelles différentes. Par exemple, c'est le cas des tremblements de terre, des plus grands au plus petits mouvements de la croûte terrestre, de fractals, de réseaux neuronaux, du remplissage des poumons. Une liste très longue de phénomènes peut être établie dans des domaines différents et avec des échelles différentes.
L'auto-similarité peut être très utile. D'un côté, à l'intérieur du même phénomène cette propriété nous permet de nous concentrer sur le comportement global plutôt que de considérer des détails précis qui deviennent négligeables pour les échelles plus grandes. Cela permet également la comparaison entre phénomènes qui sont apparemment différents mais qui présentent le même comportement statistique. Il devient ainsi possible de comprendre des phénomènes compliqués, par exemple les tremblements de terre qui ont des échelles spatiales et temporelles très grandes, ceci en étudiant un phénomène plus simple mais qui est auto-similaire.
Parmi les phénomènes qui montrent une intermittence et une auto-similarité, il y a aussi les transformations martensitiques et on note aussi beaucoup de matériaux différents comme les super-conducteurs, les métaux ferromagnetiques et les matériaux poreux. Cette caractéristique est particulièrement intéressante parce que les transformations martensitiques sont généralement décrites comme des phénomènes continus même si, en regardant les détails, il y a des études qui montrent une séquence d'événements différents caractérisés par plusieurs dimensions.
La question est si dans notre cas et avec nos données, il y a ce comportement intermittent ou pas et, dans le cas d'une réponse positive, si nous sommes capable de le quantifier ou pas.

Dans le Chapitre 4 nous regardons la transformation martensitique d'un point de vue statistique. Nous commençons en analysant les quantités qui nous avions présentées dans le chapitre précédent, à savoir la fraction de phase martensitique et la défor-

mation verticale. Ensuite, nous continuons en définissant la nition d'avalanche dans les cartes bidimensionnelles des déformations, puis nous étudions leurs propriétés come l'amplitude ou la dimension. Ainsi, nous démontrons que la transformation a lieu à travers des événements intermittents qui couvrent plusieurs échelles. Nous avons conduit une comparaison entre magnitude et dimension des avalanches, ainsi qu'une une caractérisation de leur comportement statistique. Celle-ci a été réaliséeen utilisant aussi la méthode du maximum de vraisemblance. Les deux quantités montrent clairement des distributions en ligne avec l'hypothèse d'intermittence et d'auto-similarité. En outre, nous avons analysé la non-stationnarité de la transformation en montrant des comportements statistiques différents pour plusieurs parties de la transformation.

Nous concluons la thèse en traitant un autre type d'analyse des transformations martensitiques dans les AMF. Au lieu de nous concentrer sur le comportement intermittent, nous avons regardé l'effetde fatigue ou d'effets plastiques dans la transformation martensitique. En fait, plusieurs applications des AMFs, comme les actuateurs ou les stents coronaires, exigent un comportement cyclique qui doit rester stable pendant une longue période. Pas conséquent, nous avons abandonné l'échelle microscopique et nous avons regardé le matériau comme un continuum macroscopique, en utilisant la base théorique donnée dans le premier chapitre avec la théorie de Rajagopal.
Nous avons développé un modèle qui considère la production d'effets permanents pendant la transformation, ceci sans regarder la microstructure. Nous avons testé nos résultats numériques obtenus en résolvant les équations du modèle dans une approximation unidimensionnelle, ceci à travers une comparaison avec des résultats expérimentaux pour des transformations contrôlées par la température ou par la contrainte. En outre, nous avons montré la possibilité de calibrer les paramètres du modèle pour des cas différents. De cette manière, nous avons fourni une analyse de la transformation martensitique avec une stratégie de l'approche microscopique différente de celle que nous avions utilisée pour l'intermittence.

Tous ces points de vue différents peuvent être utilisés pour traiter les transformations martensitiques, dans le but d'améliorer notre connaissance dans ce domaine, ce qui était exactement notre objectif dans cette thèse.

Contents

CHAPTER 1

Theoretical Background on Shape Memory Alloys

In this chapter we provide the theoretical background that is necessary to understand the rest of the thesis. We start by introducing Shape Memory Alloys (SMAs) and their martensitic transformation. We then continue by focusing on crystallography in martensitic materials, that is used in the analysis of data performed in Chapter 3. Finally, we move towards the macroscopic scale and arrive to Rajagopal's theory of dissipative processes, that is the basis of the model of Chapter 5.

1.1 Shape Memory Alloys and Martensitic Transformations

Shape Memory Alloys (SMAs) are very interesting materials that are mainly characterized by two properties: the Shape Memory Effect (SME) and the Pseudo-Elasticity (PE). Their applications range from tools in Aeronautics and Aerospace to biomedical devises and everyday objects (arms for glasses or smoke detectors). In this section we explain the basic behavior of shape memory alloys and we introduce the main ingredients that are necessary to deal with them.

1.1.1 Austenite and martensite

Shape Memory Alloys are crystalline solids whose interesting properties derive by their undergoing a so-called *Martensitic Transformation* (MT). This transformation is a solid-to-solid first order phase transition between two different microstructures: *austenite* and *martensite*.

Let us distinguish between these two phases. *Austenite* is characterized by a highly symmetric lattice and is stable for high temperatures. On the other hand, *Martensite* is stable for lower temperatures and is less symmetric than austenite. This lack of symmetry with respect to austenite provides the existence of different variants of martensite, as will be better detailed in Section 1.2.2. Figure 1.1 shows a scheme of the kind of relation existing between the two phases in a simple case.

During the martensitic transformation austenite and the various variants of martensite can co-exist in different combinations.

There are basically two ways to obtain a martensitic transformation in SMAs: by

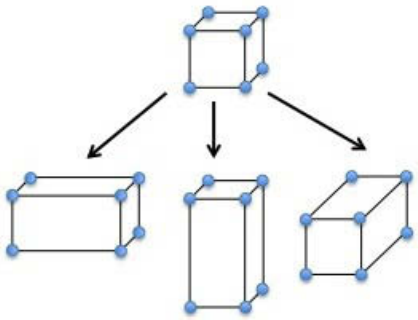

Figure 1.1: Simple example of different symmetry between austenite and martensite

applying a load or by varying the temperature. The variation of temperature simply makes one phase favorite with respect to the other one while the application of stress on an austenitic phase develops the so-called *stress-induced* martensite. This martensitic transformation is the basis of the two particular functional properties of SMAs.

1.1.2 Shape Memory Effect and Pseudo-Elasticity

Let us briefly describe the different steps undergone by SMAs in the Shape Memory Effect (SME) and in Pseudo-Elasticity (PE).

Figure 1.2 shows a schematic view of SME.

- Let us start with our specimen in a stress-free state at a high temperature, so that it is completely austenitic (lower left part of the scheme);

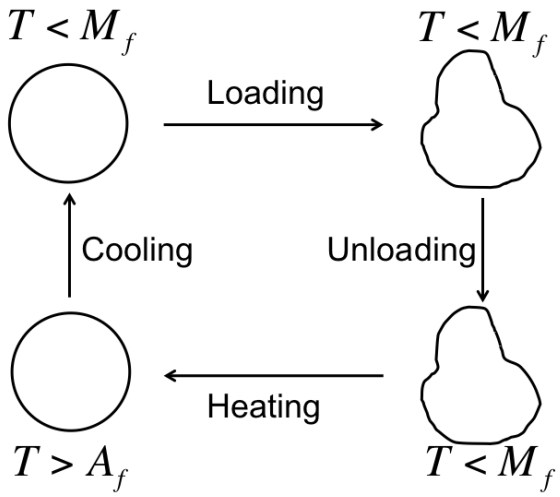

Figure 1.2: Scheme of the Shape Memory Effect.

- We cool the specimen until we reach a temperature that is low enough to guarantee stability for martensite. Since there is no external load, the specimen does not deform on a macroscopic scale. From the microscopic point of view we are moving from austenite to martensite (upper left part of the scheme);
- We keep a constant low temperature and we load the specimen, thus inducing a macroscopic deformation. At a microscopic level, different variants of martensite are differently re-orientered in order to satisfy the external conditions (lower right part of the scheme);
- We remove the load without varying the temperature. Since martensite is stable at the temperature, the specimen just stays in the current configuration, without recovering the external deformation (lower right part of the scheme);
- We heat the specimen until an austenitic temperature: the specimen returns back to its original shape (lower left part of the scheme, again).

The main cause of this behavior lies in the existence of many different variants of martensite corresponding to a single kind of austenite. In this way, though the crystallographic structure moves among different variants of martensite at low temperature, it has one possible choice for the austenitic configuration, that corresponds to the shape that is always remembered by the material.
As regards the PE, it is the phenomenon that we are going to investigate with our experimental test in Section 2.1.2 and can be described in the following way:

- Let us start with a stress-free specimen in the austenitic phase, that is at high temperature;

- We start loading the specimen thus inducing an initial elastic deformation;
- By keeping on loading we obtain the appearance of stress-induced martensite variants that re-arrange to cope with the external load;
- Eventually, if we keep on loading we obtain a completely martensitic phase and just some further elastic deformation.
- By unloading, we reverse the transformation so that we can go back to the initial austenitic phase.

The consequence of this behavior is that SMAs are able to undergo deformations up to $8\%-10\%$ of strain, just like rubbers, while metals usually reach strains around $1\%-2\%$.

1.1.3 Mathematical models for Shape Memory Alloys

From the mathematical point of view, the study of Shape Memory Alloys developed mainly around 1980s, together with a bigger interest from the experimental point of view, though the discovery of the first alloys dated back to 1930s. Basically, Shape Memory Alloys show some interesting macroscopic features directly due to a microscopic phase change at the crystal scale. For this reason, mathematical models aiming at reproducing their behavior can focus on different scales. Moreover, among martensitic materials it is possible to distinguish between monocrystalline solids (or single-crystal materials) and polycrystalline ones. In a monocrystalline solid the austenitic lattice is uniform in all the specimen. Conversely, polycrystalline materials are composed by agglomerates of crystals (or *grains*) whose austenite is the same from the lattice point of view but differs in the orientation. Actually, single crystals are easier from the theoretical point of view but rarer to be found both in nature and in industry than polycrystals. Thus, to distinguish among the different mathematical models, we can also consider their adaptability to the monocrystal or polycrystal case.

A branch of mathematical models which can be easily used both for monocrystals and polycrystals is the one of the microscopic models for martensitic transformations. By starting from Ericksen's ideas [36–38], it was possible to combine nonlinear continuum mechanics with the crystallographic theory for martensitic materials [19, 53, 54, 70, 75] (whose introduction is provided in the next section) and with non-convex variational calculus [14, 18]. The basic idea is that each grain in the material is in a particular phase, which is determined by combining minimization of energy and interaction with neighboring grains. The application to the polycrystalline case is

straightforward since the model already considers the crystalline scale. The deduced information is very detailed. For this reason, this class of models, like phase-fields models [103] or automaton models [72, 82], seems to be convenient for the reproduction of intermittency in the transformation.
Though we are not going to use this kind of model in this thesis, in the following section we shall provide the instruments to understand the martensitic phase transition from a crystallographic point of view and we shall give some theoretical results, successively used for the data analysis.

Together with microscopic models for SMAs there also exist mathematical models that consider SMAs as macroscopic continua, according to continuum thermodynamics theory [44]. Thus, their behavior can be modeled with the methods of nonlinear elasticity theory by providing an expression for the free energy density. This group of models includes works with different loading variables, like temperature [42] or stress [90], together with works on the hysteretic behavior of SMAs [63, 64] and on theoretical analysis applied to elasto-plastic systems [61]. All these studies pay attention to the macroscopic behavior of the material without going into detail on the crystalline structure. By consequence, the deduced information is less detailed than for models that take into account also for the microstructure. These models are particularly easy to be used in the monocrystalline case while the case of polycrystalline materials could become more complicated: the model should be solved for each grain of the material and it would lack of the information on the relative rotations between neighboring grains. On the other hand, since they catch some more general properties, these models are particularly suitable for different cases, like stress-induced or temperature-induced transformations, and when the interest is only on the macroscopic results.
This kind of model will be used in Chapter 5 to reproduce permanent effects during the transformation. A macroscopic model seems to be particularly useful in this sense since the final goal is to quantify the plastic deformation and compare it with some experimental test, in which microscopical quantities are not measured. Moreover, since the model is quite easy to be solved in different cases, it can be tested with experimental data from different kinds of experiments.

1.2 Crystallographic Theory of Martensitic Materials

Crystallographic theory provides several relations between the austenitic phase and the martensitic one at the crystal level. In particular, it relates compatibility between

different micrustructures to the crystal properties of the material. Moreover, it provides the theoretical formulas for the computation of the features of some microstructural combinations, for example the austenite-martensite transformation interfaces.

1.2.1 Cristalline solids and Cauchy-Born hypothesis

Let us start by considering our solid from the crystallographic point of view.
In crystallography, one of the fundamental notions is the definition of *Bravais lattice*. It is usually denoted by $\mathcal{L}(\boldsymbol{e}_i, \boldsymbol{o})$ and defined as follows

$$\mathcal{L}(\boldsymbol{e}_i, \boldsymbol{o}) = \{\boldsymbol{x} : \boldsymbol{x} = \nu^i \boldsymbol{e}_i + \boldsymbol{o},\ \nu^i \in \mathbb{Z}, i = 1, 2, 3\}, \tag{1.1}$$

where $\boldsymbol{o}$ is considered the origin of the lattice while $\{\boldsymbol{e}_1, \boldsymbol{e}_2, \boldsymbol{e}_3\}$ are called *lattice vectors* .
A lattice $\mathcal{L}(\boldsymbol{e}_i, \boldsymbol{o})$ can be deformed into another lattice $\mathcal{L}(\boldsymbol{f}_i, \boldsymbol{o})$ by applying a deformation to the lattice vectors, that is by introducing a matrix $\boldsymbol{F}$ such that det$\boldsymbol{F} \neq 0$ and

$$\boldsymbol{f}_i = \boldsymbol{F}\boldsymbol{e}_i,\ i = 1, 2, 3.$$

As a consequence of the symmetry of the lattice, it is possible to find deformations that map the lattice back into itself. It has been proved that these deformations can be simply characterized by using the following result [19].

Result 1.2.1. *Two sets of lattice parameters $\{\boldsymbol{e}_1, \boldsymbol{e}_2, \boldsymbol{e}_3\}$ and $\{\boldsymbol{f}_1, \boldsymbol{f}_2, \boldsymbol{f}_3\}$ generate the same lattice $\mathcal{L}(\boldsymbol{e}_i, \boldsymbol{o}) = \mathcal{L}(\boldsymbol{f}_i, \boldsymbol{o})$ if and only if*

$$\boldsymbol{f}_i = \sum_{j=1}^{3} \mu_i^j \boldsymbol{e}_j$$

for some matrix $[\mu_i^j] \in GL(3, \mathbb{Z})$, where $GL(3, \mathbb{Z})$ is the group of all matrices with integral elements ($\mu_i^j \in \mathbb{Z}$) and unitary determinant (det$[\mu_i^j] = \pm 1$).

According to this result, a matrix $\boldsymbol{H}$ maps a lattice back to itself if and only if

$$\boldsymbol{H}\boldsymbol{e}_i = \sum_{j=1}^{3} \mu_i^j \boldsymbol{e}_j = \mu_i^j \boldsymbol{e}_j, \quad i = 1, 2, 3, \text{ and } [\mu_i^j] \in GL(3, \mathbb{Z}),$$

where the sum over the repeated index is introduced. This characterization allows us to define the so-called *symmetry group of the lattice*

$$\mathcal{G}(\boldsymbol{e}_i) = \left\{\boldsymbol{H} :\ \boldsymbol{H}\boldsymbol{e}_i = \mu_i^j \boldsymbol{e}_j \text{ for some } [\mu_i^j] \in GL(3, \mathbb{Z})\right\}.$$

This set includes all the rotations and the shears that map the lattice into itself. Though, there is a fundamental distinction between the shears and the rotations of the group.

While the rotations do not basically change the crystal, the shears are related to plasticity. Actually, they map the lattice into itself when dealing with infinite lattices but induce dislocations or border effects when involving real finite lattices, as can be understood by looking at Figure 1.3 for a two-dimensional lattice. In order to focus on the

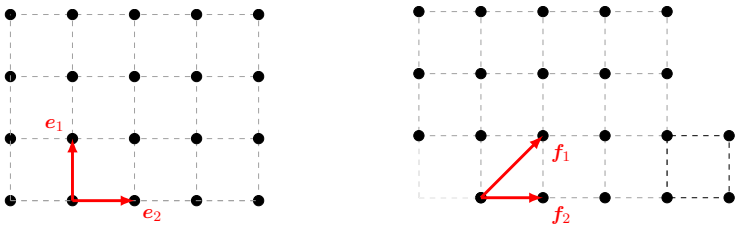

Figure 1.3: The infinite two-dimensional lattices generated by the lattice parameters $\{\boldsymbol{e}_1, \boldsymbol{e}_2\}$ and $\{\boldsymbol{f}_1, \boldsymbol{f}_2\} = \{\boldsymbol{H}\,\boldsymbol{e}_1, \boldsymbol{H}\,\boldsymbol{e}_2\}$ where $\boldsymbol{H}$ is a shear in $\mathcal{G}(\boldsymbol{e}_i)$ are equivalent. This equivalence is lost in the case of the finite lattices shown above, since border effects arise.

mechanism of the martensitic transformation, let us assume to neglect plasticity at this level of the theory thus considering only the rotations in $\mathcal{G}(\boldsymbol{e}_i)$. We thus define the *point group of the lattice*

$$\mathcal{P}(\boldsymbol{e}_i) = \{\boldsymbol{R} : \ \boldsymbol{R} \text{ rotation in } \mathcal{G}(\boldsymbol{e}_i)\}, \tag{1.2}$$

that is the set of all the rotations that map the lattice into itself.

We now take a further step in order to link this crystallographic description of the lattice with a continuum view of the solid. Let us assume to have a crystalline solid in a region $\Omega \in \mathbb{R}^3$ such that at each point $\boldsymbol{x} \in \Omega$ its structure can be described through a Bravais lattice with vectors $\{\boldsymbol{e}_i^0(\boldsymbol{x})\}$. We then deform the solid according to a deformation gradient $\boldsymbol{F}(\boldsymbol{x}) = \nabla \boldsymbol{y}$ and we indicate the lattice vectors in the material point $\boldsymbol{x}$ after the deformation with $\{\boldsymbol{e}_i(\boldsymbol{x})\}$.
The result that links the crystallographic level with the continuum one, which is known as *Cauchy-Born hypothesis*, relates the two sets of lattice vectors as follows

$$\boldsymbol{e}_i(\boldsymbol{x}) = \boldsymbol{F}(\boldsymbol{x})\boldsymbol{e}_i^0(\boldsymbol{x}).$$

It means that the deformation we consider for the continuum is actually the same deformation that is undergone at the lattice level.
For simplicity, let us assume that the reference configuration is homogeneous, so that there is no dependence on $\boldsymbol{x}$ in the lattice vectors $\{\boldsymbol{e}_i^0\}$.

We now assume to describe the behaviour of the material through the introduction of a certain *energy density function*. We start by characterizing this function on the Bravais lattice and we pass to an energy density on the continuum through the use of

the Cauchy-Born hypothesis.
Let us suppose that the energy density function on the Bravais lattice depends on the lattice vectors and on temperature θ so that

$$\hat{\varphi}(\boldsymbol{e}_i, \theta).$$

We require the satisfaction of the following properties:

- *Frame-indifference*

$$\hat{\varphi}(\boldsymbol{Q}\boldsymbol{e}_i, \theta) = \hat{\varphi}(\boldsymbol{e}_i, \theta) \quad \forall \boldsymbol{Q} \in \mathcal{Q},$$

  where $\mathcal{Q}$ is the set of all three-dimensional rotations. It implies that if we rigidly rotate the lattice vectors we do not affect the energy;

- *Material symmetry*

$$\hat{\varphi}(\mu_i^j \boldsymbol{e}_j, \theta) = \hat{\varphi}(\boldsymbol{e}_i, \theta) \quad \forall [\mu_i^j] \in GL(3, \mathbb{Z}),$$

  that means that two sets of lattice vectors generating the same lattice (according to the Result 1.2.1) also have to correspond to the same energy.

As already said, the Cauchy-Born hypothesis allows us to define the continuum free energy density

$$\varphi(\boldsymbol{F}, \theta) = \hat{\varphi}(\boldsymbol{F}\boldsymbol{e}_i^0, \theta),$$

where $\{\boldsymbol{e}_i^0\}$ are the lattice vectors in the chosen reference configuration that is deformed with a deformation gradient equal to $\boldsymbol{F}$, as above.
The frame-indifference requirement is now translated in claiming

$$\varphi(\boldsymbol{Q}\boldsymbol{F}, \theta) = \varphi(\boldsymbol{F}, \theta) \quad \forall \boldsymbol{Q} \in \mathcal{Q}.$$

Analogously, the material symmetry condition, after some calculation, provides

$$\varphi(\boldsymbol{F}\boldsymbol{H}, \theta) = \varphi(\boldsymbol{F}, \theta) \quad \forall \boldsymbol{H} \in \mathcal{P}(\boldsymbol{e}_i^0),$$

where we assume to neglect shears of the lattice vectors and thus use $\mathcal{P}(\boldsymbol{e}_i^0)$ instead of $\mathcal{G}(\boldsymbol{e}_i^0)$.

Now, let us decompose the deformation gradient by using the polar decomposition theorem and thus obtaining $\boldsymbol{F} = \boldsymbol{R}\boldsymbol{U}$, where $\boldsymbol{R} \in \mathcal{Q}$ and $\boldsymbol{U}$ is a positive-definite symmetric tensor. This last matrix is called *Bain strain matrix* or transformation strain matrix and, as a consequence of the frame-indifferece, we obtain that the energy density depends only on this part of the deformation gradient.

Finally, we define the total energy for our continuum related to a deformation with a gradient $\boldsymbol{F}$ as

$$\mathcal{F} = \int_{\Omega} \varphi(\boldsymbol{F}, \theta)\, d\boldsymbol{x}.$$

We define an equilibrium as *stable* when it is an absolute minimizer and *metastable* when it is a relative minimizer, at a given temperature θ. In the case of SMAs we will deal with metastable equilibria since there will be many minima that are energetically equivalent. The presence of metastable equilibria will also imply the hysteretic behavior that characterizes SMAs. Actually, hysteresis is due to dissipation or production of entropy, thus it is related to thermodynamical irreversible processes. This irreversibility is the signal that the system is not in a stable equilibrium during the process, since it is actually moving among different metastable minima [52].

1.2.2 The Austenite-Martensite transformation

In order to deal with the Austenite-Martensite transformation, let us indicate the austenite lattice vectors with $\{\boldsymbol{e}_1^a, \boldsymbol{e}_2^a, \boldsymbol{e}_3^a\}$. Analogously, let us suppose to have only one variant of martensite and to use $\{\boldsymbol{e}_1^m, \boldsymbol{e}_2^m, \boldsymbol{e}_3^m\}$ to indicate its lattice vectors. We also introduce the martensite Bain matrix $\boldsymbol{U}_1$ such that

$$\boldsymbol{e}_i^m = \boldsymbol{U}_1 \boldsymbol{e}_i^a.$$

As a consequence of the Cauchy-Born hypothesis, from the continuum point of view the austenitic phase is represented by the identity matrix $\boldsymbol{I}$ while the martensite is related to a deformation equal to $\boldsymbol{U}_1$.

We now focus for a moment on how the energy depends on the temperature θ. We know that austenite is stable for high temperatures while martensite is preferred for low temperatures. Thus, the energy has the behaviour shown in Figure 1.4. There is a particular temperature, θ_0, called *transformation temperature*, for which both phases are equivalent. Above this temperature the energy has a minimum coinciding with austenite while under θ_0 the minimum is given by the martensite, that is

$$\begin{aligned}
&\varphi(\boldsymbol{I}, \theta) \leq \varphi(\boldsymbol{F}, \theta) && \theta > \theta_0, \\
&\varphi(\boldsymbol{I}, \theta) = \varphi(\boldsymbol{U_1}, \theta) \leq \varphi(\boldsymbol{F}, \theta_0) && \theta = \theta_0, \\
&\varphi(\boldsymbol{U_1}, \theta) \leq \varphi(\boldsymbol{F}, \theta) && \theta < \theta_0.
\end{aligned}$$

Finally, we have to take into account the existence of many variants of martensite, that

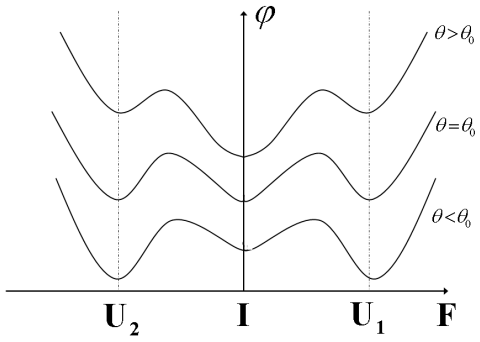

Figure 1.4: Scheme of the dependence of the energy density function on the temperature.

is a consequence of the higher symmetry of the austenitic lattice with respect to the martensitic one.

Let us denote the symmetry group of the austenitic lattice with $\mathcal{P}^a$, according to the definition (1.2). Let us apply a rotation $\boldsymbol{R} \in \mathcal{P}^a$ to the austenitic lattice and then trasform it into martensite. The corresponding transformation matrix is $\boldsymbol{R}^T\boldsymbol{U}_1\boldsymbol{R}$. As a consequence of the assumption on the austenite being more symmetric than the martensite, for certain rotations we shall have $\boldsymbol{R}^T\boldsymbol{U}_1\boldsymbol{R} = \boldsymbol{U}_k \neq \boldsymbol{U}_1$ for some $k \in 1, \ldots, N$ where N is the number of variants, detailed below. Thus, the set of the variants of martensite is given by all the different matrices resulting in $\{\boldsymbol{Q} \in \mathcal{P}^a : \boldsymbol{Q}\boldsymbol{U}_1\boldsymbol{Q}^T\}$. For some other rotations the transfomation matrix will be $\boldsymbol{R}^T\boldsymbol{U}_1\boldsymbol{R} = \boldsymbol{U}_1$, that is for the rotations that belong to the point group of the martensite. We thus define the point group of martensite

$$\mathcal{P}^m = \{\boldsymbol{Q} \in \mathcal{P}^a : \boldsymbol{Q}\boldsymbol{U}_1 Q^T = \boldsymbol{U}_1\}$$

as a subset of the point group of austenite. We remark that the point group of the different variants is always the same since alla the variants show the same symmetry. The number of the variants of martensite can thus be computed as

$$N = \frac{\text{number of elements in } \mathcal{P}^a}{\text{number of elements in } \mathcal{P}^m}.$$

The different symmetries in the austenitic phase and in the martensitic one provides different kinds of transformations, like *cubic to tetragonal, cubic to orthorombic* or *cubic to monoclinic* transformations, which will be thus associated to a precise number of possible variants of martensite.

The possibility of having more variants of martensite that are energetically equivalent is taken into account through the material symmetry requirement on the energy density, since it implies

$$\varphi(\boldsymbol{U}_1, \theta) = \varphi(\boldsymbol{U}_2, \theta) = \ldots = \varphi(\boldsymbol{U}_N, \theta).$$

On the other hand, frame-indifference states the equivalence within lattices that are obtained through rigid rotations. The consequence of this requirement is that energy is minimized not only by $\boldsymbol{I}$ for austenite or by $\boldsymbol{U}_i$ for martensite but by an entire orbit of matrices, called *energy well*. In particular, let us define

$$\mathcal{A} = \{\boldsymbol{F} : \boldsymbol{F} = \boldsymbol{Q} \text{ for some rotation } \boldsymbol{Q}\},$$

$$\mathcal{M}_1 = \{\boldsymbol{F} : \boldsymbol{F} = \boldsymbol{Q}\boldsymbol{U_1} \text{ for some rotation } \boldsymbol{Q}\},$$

$$\vdots$$

$$\mathcal{M}_n = \{\boldsymbol{F} : \boldsymbol{F} = \boldsymbol{Q}\boldsymbol{U_n} \text{ for some rotation } \boldsymbol{Q}\}.$$

The set $\mathcal{A}$ is called austenite well and frame-indifference implies $\varphi(\boldsymbol{F}, \theta) = \varphi(\boldsymbol{I}, \theta), \forall \boldsymbol{F} \in \mathcal{A}$. Analogously, $\mathcal{M}_i$ is the energy well for the $i-$th variant of martensite and it is also possible to introduce a further set $\mathcal{M} = \cup \mathcal{M}_i$ so that the energy has the same value for all the matrices in $\mathcal{M}$ (by combining frame-indifference and material symmetry).
Thus, the energy density ends up having an infinite number of minima depending on the temperature as follows:

$$\varphi(\boldsymbol{G}, \theta) \leq \varphi(\boldsymbol{F}, \theta) \quad \forall \boldsymbol{G} \in \mathcal{A},\ \forall \boldsymbol{F},\ \theta > \theta_0,$$

$$\varphi(\boldsymbol{G}, \theta) \leq \varphi(\boldsymbol{F}, \theta_0) \quad \forall \boldsymbol{G} \in \mathcal{A} \cup \mathcal{M},\ \forall \boldsymbol{F},\ \theta = \theta_0,$$

$$\varphi(\boldsymbol{G}, \theta) \leq \varphi(\boldsymbol{F}, \theta) \quad \forall \boldsymbol{G} \in \mathcal{M},\ \forall \boldsymbol{F},\ \theta < \theta_0.$$

According to this description, the study of the microstructure can be done by focusing only on the austenite and martensite wells, or simply by considering a representative deformation for each well up to suitable rotations.

1.2.3 Kinematic Compatibility conditions

In martensitic materials it often happens to see various combinations of different crystallographic microstructures, like austenite together with martensite (one or more variants). In particular, we can likely obtain deformations that are continuous but with a discontinuous gradient, with coherent interfaces along the gradient jumps. A scheme of this kind of deformation is shown in Figure 1.5.
Let us suppose that our continuum occupies a domain $\Omega \in \mathbb{R}^3$ that is partitioned in two zones, Ω_1 and Ω_2, in which the deformation gradients are different between each other

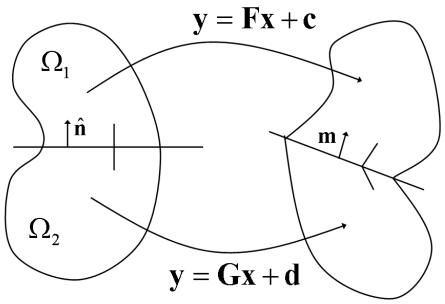

Figure 1.5: Scheme of a continuous deformation with a gradient jumps along the interface.

(but constant within the Ω_i), that is

$$\boldsymbol{y} = \begin{cases} \boldsymbol{F}\boldsymbol{x} + \boldsymbol{c} & \boldsymbol{x} \in \Omega_1, \\ \boldsymbol{G}\boldsymbol{x} + \boldsymbol{d} & \boldsymbol{x} \in \Omega_2. \end{cases}$$

Now, the values of $\boldsymbol{F}$ and $\boldsymbol{G}$ are not arbitrary if we want to assure continuity of the deformation $\boldsymbol{y}$, but they have to satisfy the so-called *Hadamard compatibility condition* or *kinematic compatibility equation* [19]:

$$\boldsymbol{F} - \boldsymbol{G} = \boldsymbol{b} \otimes \boldsymbol{m}, \tag{1.3}$$

for some vectors $\boldsymbol{b}$ and $\boldsymbol{m}$. Actually, $\boldsymbol{m}$ has also a physical meaning since it is going to be the normal to the interface between Ω_1 and Ω_2 in the deformed configuration.
It can be shown that this condition is equivalent to claiming that the plane separating Ω_1 and Ω_2 has to deform in the same way both when viewed from Ω_1 and from Ω_2. This situation is called *invariant plane condition*. In order to show this equivalence, let us consider a vector $\boldsymbol{v}$ along the interface between Ω_1 and Ω_2. When the Hadamard condition (1.3) holds, we have

$$\boldsymbol{F}\boldsymbol{v} - \boldsymbol{G}\boldsymbol{v} = (\boldsymbol{b} \otimes \boldsymbol{m})\boldsymbol{v} = \boldsymbol{b}(\boldsymbol{v} \cdot \boldsymbol{m}).$$

But $\boldsymbol{v} \cdot \boldsymbol{m} = 0$ since $\boldsymbol{v}$ lies on the interface (see Figure 1.5), thus we obtain $\boldsymbol{F}\boldsymbol{v} = \boldsymbol{G}\boldsymbol{v}$, *i.e.* the effect of $\boldsymbol{F}$ and $\boldsymbol{G}$ is the same for each vector on the interface, as required by the invariant plane condition.
The compatibility equation (1.3) plays a very important role in the crystallographic theory of martensitic materials since it allows us to determine which combinations of austenite and variants of martensite are compatible in different kinds of specimens.
In particular, we are going to analyze compatibility between austenite and a simple variant of martensite.

1.2.4 Austenite-Martensite interface

In order to study the features of the combination between austenite and a single variant of martensite, let us start with a more general result, known as *twinning equation*:

$$\boldsymbol{Q}\boldsymbol{U}_I - \boldsymbol{U}_J = \boldsymbol{a} \otimes \hat{\boldsymbol{n}}. \tag{1.4}$$

This equation is simply the Hadamard compatibility condition applied to the following situation

$$\nabla \boldsymbol{y} = \begin{cases} \boldsymbol{Q_1 U_I} & \text{in } \Omega_1 \\ \\ \boldsymbol{Q_2 U_J} & \text{in } \Omega_2, \end{cases}$$

that is the deformation belongs to the $I-$th well in Ω_1 and to the $J-$th well in Ω_2. By writing equation (1.3) for this piecewise homogeneous deformation and by setting $\boldsymbol{Q} = \boldsymbol{Q}_2^T \boldsymbol{Q}_1$ and $\boldsymbol{a} = \boldsymbol{Q}_2^T \boldsymbol{b}$, we thus obtain equation (1.4). The name of the equation as twinning equation is due to the fact that it actually describes a martensite twin.

We now report an important result by Ball and James [14] which provides a procedure for the solution of the twin equation.

Result 1.2.2. *Given $\boldsymbol{F}$ and $\boldsymbol{G}$ matrices with positive determinant, the following method provides a rotation $\boldsymbol{Q}$ and two vectors $\boldsymbol{a} \neq \boldsymbol{0}$ and $\hat{\boldsymbol{n}}$ such that*

$$\boldsymbol{Q}\boldsymbol{F} - \boldsymbol{G} = \boldsymbol{a} \otimes \hat{\boldsymbol{n}}.$$

- *Calculate the matrix $\boldsymbol{C} = \boldsymbol{G}^{-T}\boldsymbol{F}^T\boldsymbol{F}\boldsymbol{G}^{-1}$;*
- *If $\boldsymbol{C} = \boldsymbol{I}$, there is no solution;*
- *If $\boldsymbol{C} \neq \boldsymbol{I}$, calculate and order the eigenvalues of the matrix $\boldsymbol{C}$: $\lambda_1 \leq \lambda_2 \leq \lambda_3$;*
- *The equation has a solution if and only if it holds*

$$\lambda_1 \leq 1, \quad \lambda_2 = 1, \quad \lambda_3 \geq 1.$$

- *If all these conditions are satisfied, there are exactly two solutions*

$$\boldsymbol{a} = \rho \left(\sqrt{\frac{\lambda_3(1-\lambda_1)}{\lambda_3 - \lambda_1}} \hat{\boldsymbol{e}}_{\boldsymbol{1}} + \kappa \sqrt{\frac{\lambda_1(\lambda_3 - 1)}{\lambda_3 - \lambda_1}} \hat{\boldsymbol{e}}_{\boldsymbol{3}} \right), \tag{1.5}$$

$$\hat{\boldsymbol{n}} = \frac{1}{\rho} \frac{\sqrt{\lambda_3} - \sqrt{\lambda_1}}{\sqrt{\lambda_3 - \lambda_1}} \left(-\sqrt{1-\lambda_1} \boldsymbol{G^T} \hat{\boldsymbol{e}}_1 + \kappa \sqrt{\lambda_3 - 1} \boldsymbol{G^T} \hat{\boldsymbol{e}}_3 \right), \tag{1.6}$$

where $\kappa = \pm 1$ distinguishes between the two solutions and ρ normalizes $\hat{\boldsymbol{n}}$.
Rotation $\boldsymbol{Q}$ is eventually determined after substituting $\boldsymbol{a}$ and $\hat{\boldsymbol{n}}$ in the initial equation.

Since we are interested in the compatibility between austenite and a single variant of martensite (let us suppose to take the $I-$th variant), we can use this result by considering $\boldsymbol{F} = \boldsymbol{U}_I$ and $\boldsymbol{G} = \boldsymbol{I}$.
The first requirement to be satisfied in order to have a solution is $\boldsymbol{C} = \boldsymbol{G}^{-T}\boldsymbol{F}^T\boldsymbol{F}\boldsymbol{G}^{-1} = \boldsymbol{I}\boldsymbol{U}_I^T\boldsymbol{U}_I\boldsymbol{I} = \boldsymbol{U}_I^2 \neq \boldsymbol{I}$. This request is obviously satisfied since $\boldsymbol{U}_I^2 = \boldsymbol{I}$ would correspond to a constant deformation gradient equal to the identity in all the domain.
The second condition is on the eigenvalues of $\boldsymbol{C} = \boldsymbol{U}_I^2$. Indeed, the condition can be directly translated into the same requirement for the eigenvalues of $\boldsymbol{U}_I$:

$$\lambda_1(\boldsymbol{U}_I) \leq 1, \quad \lambda_2(\boldsymbol{U}_I) = 1, \quad \lambda_3(\boldsymbol{U}_I) \geq 1. \tag{1.7}$$

The condition on having an eigenvalue equal to one is particularly difficult to satisfy, so that the combination of austenite and a single variant of martensite is not possible in many martensitic materials. One of the solutions to this incompatibly is the creation of a twinning of two variants of martensite. This is not the case for the material we used in our work and that is described in Section 2.1.1, where austenite and single variants of martensite are compatible. Moreover, we also used an experimental setting which allowed for the appearance of a single variant of martensite against austenite, as explained in Section 3.1.2. Thus, after making some consideration on the probability of having a single variant of martensite, we shall use the expressions (1.5) and (1.6) for the computation of the crystallographic structure in the case of our specimen and compare these theoretical results with the experimental ones in Section 3.2.2.

1.3 Macroscopic Modeling of SMAs

We now take a further step in modeling SMAs by introducing the theory of irreversible processes by Rajagopal [79, 80]. We shall use it in Chapter 5 in order to build a macroscopic model taking into account functional fatigue in martensitic transitions.

1.3.1 Elastic domain and natural configurations

Let us initially recall the link between initial configuration, deformation and stress for elastic materials, in order to further move towards elasto-plasticity.
We denote the reference configuration with κ_r and the position of a particle in this configuration with $\boldsymbol{X}$. We further introduce the deformation χ_{κ_r} between the reference configuration and the current one, so that the position $\boldsymbol{x}$ of the particle that was initially in $\boldsymbol{X}$ can be expressed by

$$\boldsymbol{x} = \chi_{\kappa_r}(\boldsymbol{X}, t).$$

The constitutive requirement for elastic materials is that the Cauchy stress tensor is a function only of the gradient of the deformation, that is

$$\boldsymbol{T} = \hat{\boldsymbol{T}}_{\boldsymbol{\kappa_r}}(\boldsymbol{F}_{\boldsymbol{\kappa_r}}),$$

with $\boldsymbol{F} = \nabla \chi_{\kappa_r}$.
This first step can be used to build up a theory for more general elasto-plastic systems. The idea is to decompose the response of these systems in two parts: an elastic part and a change in the reference configuration. In order to do so, we need the concept of *elastic domain*, that is a set of configurations in which the material can be considered elastic with respect to the reference configuration. Thus, we consider an initial configuration κ_0 and an elastic domain related to this configuration. Once the material is deformed so that its configuration is outside the elastic domain, anelastic effects appear, for example microstructural changes, and they are translated in a new reference configuration κ_1 and a new elastic domain referred to κ_1.
All the configurations that may be used as reference configurations for the elastic domains are called *natural configurations*. Thus, we denote the reference configuration with κ_r and we introduce a natural configuration κ_p and the deformation gradient $\boldsymbol{e}_{\text{tr}}$ between κ_r and κ_p. It means that the natural configuration can be determined by knowing the starting point κ_r and the deformation gradient $\boldsymbol{e}_{\text{tr}}$. By introducing $\boldsymbol{F}_{\kappa_p}$ as the deformation gradient between the natural configuration κ_p and the current configuration, we thus obtain that the total deformation from the initial reference configuration κ_r to the current one is actually decomposed into $\boldsymbol{F}_{\kappa_p}$ and $\boldsymbol{e}_{\text{tr}}$. The first one is an elastic deformation while the second one, e_{tr}, takes into account the anelastic effects like microscopic transformations. The link between the different components of the deformation and the configurations involved is shown in Figure 1.6.

We now assume that the Cauchy stress keeps on depending only on the total deformation gradient, so that in this case it holds

$$\boldsymbol{T} = \hat{\boldsymbol{T}}(\boldsymbol{F}_{\kappa_p}, \boldsymbol{e}_{\text{tr}}).$$

Furthermore, we can rewrite this relation by introducing the Cauchy-Green deformation tensor $\boldsymbol{E}_{\kappa_r} = \boldsymbol{F}_{\kappa_r}^T \boldsymbol{F}_{\kappa_r}$ and using the Piola-Kirchhoff tensor instead of the Cauchy tensor. First of all, we have to notice that $\boldsymbol{F}_{\kappa_p} = \boldsymbol{F}_{\kappa_r}\, \boldsymbol{e}_{\text{tr}}^{-1}$. Moreover, objectivity claims that a function of $\boldsymbol{F}_{\kappa_r}$ actually depends on $\boldsymbol{E}_{\kappa_r}$. These facts imply that every function of $\boldsymbol{e}_{\text{tr}}$ an $\boldsymbol{F}_{\kappa_p}$ is in fact a function of $\boldsymbol{e}_{\text{tr}}$ and $\boldsymbol{E}_{\kappa_r}$ so that we can write

$$\boldsymbol{S} = \hat{\boldsymbol{S}}(\boldsymbol{E}_{\kappa_r}, \boldsymbol{e}_{\text{tr}}), \tag{1.8}$$

where $\boldsymbol{S} = \det(\boldsymbol{F}_{\kappa_r}) \boldsymbol{F}_{\kappa_r}^{-}1\, \boldsymbol{T}\, \boldsymbol{F}_{\kappa_r}^{-T}$.

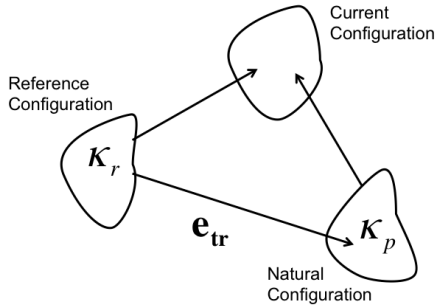

Figure 1.6: Scheme of the relation between the reference configuration κ_r, the natural one κ_p and the current one, together with the deformation gradients $\boldsymbol{e}_{\text{tr}}$, $\boldsymbol{F}_{\kappa_p}$ and $\boldsymbol{F}_{\kappa_r}$.

By consequence, we need a constitutive equation for the stress and another one for the behavior of $\boldsymbol{e}_{\text{tr}}$.
A first step in this direction consists in defining a quantity related to the rate of variation of $\boldsymbol{e}_{\text{tr}}$

$$\boldsymbol{L}_p := \dot{\boldsymbol{e}}_{\text{tr}}\, \boldsymbol{e}_{\text{tr}}^{-1},$$

which we assume to depend only on $\boldsymbol{e}_{\text{tr}}$ and $\boldsymbol{E}_{\kappa_r}$, that is $\boldsymbol{L}_p = \hat{\boldsymbol{L}}_p(\boldsymbol{E}_{\kappa_r}, \boldsymbol{e}_{\text{tr}})$. Moreover, we suppose $\boldsymbol{L}_p$ to be continuous is $\boldsymbol{E}_{\kappa_r}$. This quantity will be fundamental in all the rest of the theory and introduces here an implicit definition of the elastic domain.
Let us imagine to fix $\boldsymbol{e}_{\text{tr}}$, and to stay within the elastic domain: since the natural configuration does not change in this domain, $\dot{\boldsymbol{e}}_{\text{tr}} = \boldsymbol{0}$ and so $\boldsymbol{L_p}$ is null, too. By consequence, the elastic domain is determined by

$$\hat{\boldsymbol{L}}_p(\boldsymbol{E}_{\kappa_r}, \boldsymbol{e}_{\text{tr}}) = \boldsymbol{0}. \tag{1.9}$$

1.3.2 Dissipative evolution

In order to provide the constitutive equations necessary to complete the theory, Rajagopal introduces two scalar functionals: the *Helmholtz potential* ψ and the *rate of dissipation function* ξ. The energy ψ has to depend on the total deformation, so that we suppose

$$\psi = \hat{\psi}(\boldsymbol{E}_{\kappa_r}, \boldsymbol{e}_{\text{tr}}).$$

As explained in Section 1.2.4, there is an issue of compatibility between different phases that affects the material behavior. When there is no direct compatibility between two phases the solution consists in creating refined combinations of phases so that an average compatibility is obtained. Intuitively, finer combinations imply a better average

compatibility, so that the best choice seems to have an infinitely fine structure. On the other hand, an extremely fine structure is not energetically convenient. Thus, it becomes necessary to balance these two aspects. From the mathematical point of view it is possible to introduce a mixing entropy, that fosters the refinement of the microstructure and en interfacial energy that goes in the opposite direction, penalizing finer microstructures [32, 64]. In general, the energy for the continuum can take into account for the features of the microstructure and be ad hoc for the material [96].

In our case, we do not consider the microscopic structure and we just use a measure of the deformation that is a macroscopic mean of what happens at the micro structural level. We suppose that the microstructure can become infinitely fine and we do not introduce an interfacial energy term so that ψ does not depend on the spatial gradient of the deformation.

As regards dissipation, it is not allowed in elastic materials, whose behavior is completely reversible. This means that it is actually related only to the anelastic part of the deformation, so that we can suppose

$$\xi = \hat{\xi}(\boldsymbol{e}_{\text{tr}}, \boldsymbol{L}_p).$$

The dissipation ξ is supposed to be always nonnegative because of its physical meaning.

Tipically, we define the energy and the dissipation directly related through some dissipation inequality, for example the Clausius-Duhem inequality under isothermal hypothesis

$$\boldsymbol{S} \cdot \dot{\boldsymbol{E}}_{\kappa_r} - \varrho_0 \dot{\psi} = \hat{\xi} \geq 0.$$

In this theory, we are introducing the Helmholtz free energy and the dissipation as two indipendent functions. Thus, in order to be consistent with classical thermodinamycs, we assume

$$\boldsymbol{S} \cdot \dot{\boldsymbol{E}}_{\kappa_r} - \varrho_0 \dot{\psi} = \hat{\xi}(\boldsymbol{e}_{\text{tr}}, \hat{\boldsymbol{L}}_p(\boldsymbol{E}_{\kappa_r}, \boldsymbol{e}_{\text{tr}})), \tag{1.10}$$

for each fixed $\boldsymbol{E}_{\kappa_r}$ and $\boldsymbol{e}_{\text{tr}}$, and any $\dot{\boldsymbol{E}}_{\kappa_r}$. We already separately asked for ξ to be positive so that the Clausius-Duhem inequality is automatically satisfied.

Let us use the chain rule to write

$$\dot{\psi} = \frac{\partial \psi}{\partial \boldsymbol{E}_{\kappa_r}} \cdot \dot{\boldsymbol{E}}_{\kappa_r} + \frac{\partial \psi}{\partial \boldsymbol{e}_{\text{tr}}} \cdot \dot{\boldsymbol{e}}_{\text{tr}}$$

and combine this expansion with (1.10), thus obtaining

$$\boldsymbol{S} = \hat{\boldsymbol{S}}(\boldsymbol{E}_{\kappa_r}, \boldsymbol{e}_{\text{tr}}) = \varrho_0 \frac{\partial \hat{\psi}}{\partial \boldsymbol{E}_{\kappa_r}}. \tag{1.11}$$

In words, the stress can be determined by using the Helmholtz potential as for elastic materials, but in this case there is also a dependence on the changing reference configuration since ψ is a function also of $\boldsymbol{e}_{\text{tr}}$.
Let us further introduce the so-called *driving force function*

$$\boldsymbol{X} = \hat{\boldsymbol{X}}(\boldsymbol{E}_{\kappa_r}, \boldsymbol{e}_{\text{tr}}) := -\varrho_0 \frac{\partial \hat{\psi}}{\partial \boldsymbol{e}_{\text{tr}}} \boldsymbol{e}_{\text{tr}}^T. \tag{1.12}$$

The combination of this definition with (1.10) and (1.11) provides

$$\hat{\boldsymbol{X}}(\boldsymbol{E}_{\kappa_r}, \boldsymbol{e}_{\text{tr}}) \cdot \boldsymbol{L}_p = \hat{\xi}(\boldsymbol{e}_{\text{tr}}, \boldsymbol{L}_p). \tag{1.13}$$

The first consequence of this equation is that there is no dissipation in the elastic domain, since $\hat{\xi}(\boldsymbol{e}_{\text{tr}}, \boldsymbol{0}) = 0$. Moreover, let us look separately to the left hand size term and the right hand size one. On the left, we have the rate of energy release due to changes in the natural configuration. On the right, there is the dissipation during the total deformation. Equation (1.13) thus claims the balance between these two quantities for every admissible process undergone by the material.
This is the first restriction on the choice of $\boldsymbol{L}_p$. Let us now take a further step in determining it.

1.3.3 The Maximum Rate of Dissipation criterion

In [80], Rajagopal and Srinivasa provide a criterion for the characterization of the rate $\boldsymbol{L}_p$.

Proposition 1.3.1. ***The maximum rate of dissipation criterion***

Given the function $\hat{\boldsymbol{L}}_p$ and the values $\boldsymbol{E}_{\kappa_r}$ and $\boldsymbol{e}_{tr}$, let $\boldsymbol{L}_{p_0} := \hat{\boldsymbol{L}}_p(\boldsymbol{E}_{\kappa_r}, \boldsymbol{e}_{tr})$ and $\xi_0 = \hat{\xi}(\boldsymbol{e}_{tr}, \boldsymbol{L}_{p_0})$ be the actual values of $\boldsymbol{L}_p$ and of the rate of dissipation.
If $\boldsymbol{L}_p \neq \boldsymbol{L}_{p_0}$ is any other value of the rate of variation of the natural configuration such that

$$\hat{\xi}(\boldsymbol{e}_{tr}, \boldsymbol{L}_p) \geq \hat{\xi}(\boldsymbol{e}_{tr}, \boldsymbol{L}_{p_0})$$

then

$$\hat{\boldsymbol{X}}(\boldsymbol{E}_{\kappa_r}, \boldsymbol{e}_{tr}) \cdot \boldsymbol{L}_p < \hat{\xi}(\boldsymbol{e}_{tr}, \boldsymbol{L}_p).$$

Let us understand the main consequence of this proposition. Once the function $\hat{\boldsymbol{L}}_p$ is given and for each fixed $\boldsymbol{E}_{\kappa_r}$ and $\boldsymbol{e}_{\text{tr}}$, it is possible to choose an actual value for $\boldsymbol{L}_p$ among all the possible ones satisfying (1.10) and it corresponds to maximizing the rate of dissipation.
The maximum rate of dissipation criterion provides also a characterization of the elastic domain, through the two following results (we refer to [80] for their proofs).

Result 1.3.2.

$$\hat{\xi}(\boldsymbol{e}_{tr}, \boldsymbol{L}_p) > 0 \quad \textit{whenever} \quad \hat{\boldsymbol{L}}_p(\boldsymbol{E}_{\kappa_r}, \boldsymbol{e}_{tr}) \neq \boldsymbol{0}.$$

This means that whenever there is a change in the natural configuration there is dissipation, complementing the consequence of (1.13) according to which there is no dissipation within the elastic domain.
Moreover, the second result relates the elastic domain to the driving force $\boldsymbol{X}$ as follows

Result 1.3.3.

$$\textit{If } \boldsymbol{E}_{\kappa_r} \textit{ is such that } \hat{\boldsymbol{X}}(\boldsymbol{E}_{\kappa_r}, \boldsymbol{e}_{tr}) = \boldsymbol{0} \textit{ then } \hat{\boldsymbol{L}}_p(\boldsymbol{E}_{\kappa_r}, \boldsymbol{e}_{tr}) = \boldsymbol{0}.$$

The consequence of this result is that when the driving force is null there is no dissipation. In other words, the elastic domain includes all the configurations with driving force equal to zero.
We can further link the elastic domain to the driving force by defining two other quantities: the *driving force magnitude* and the *threshold function*. The driving force magnitude is defined as

$$d(\boldsymbol{E}_{\kappa_r}, \boldsymbol{e}_{\text{tr}}; \boldsymbol{\Pi}) := \hat{\boldsymbol{X}}(\boldsymbol{E}_{\kappa_r}, \boldsymbol{e}_{\text{tr}}) \cdot \boldsymbol{\Pi},$$

where $\boldsymbol{\Pi}$ is a given unit in the symmetric tensor linear space. It can be interpreted as the potential related to changes in the configurations in the direction $\boldsymbol{\Pi}$. It can be computed both when the natural configuration changes but also in the elastic domain.
Let us indicate with γ the norm of the strain rate $\boldsymbol{L}_p$. Result 1.3.2 claims that for $\gamma > 0$ the dissipation is non null. We thus introduce another quantity, called *threshold function*, as follows

$$\mathcal{T}(\boldsymbol{e}_{\text{tr}}, \boldsymbol{\Pi}) := \inf_{\gamma > 0} \frac{\hat{\xi}(\boldsymbol{e}_{\text{tr}}, \gamma \boldsymbol{\Pi})}{\gamma} \geq 0,$$

for each $\boldsymbol{e}_{\text{tr}}$ and $\boldsymbol{\Pi}$ fixed. The name of the quantity is due to its meaning, since it represents the threshold that the driving force has to cross in order to obtain dissipation, as stated by the following result.

Result 1.3.4. *For each fixed $\boldsymbol{e}_{tr}$, necessary and sufficient condition for $\boldsymbol{E}_{\kappa_r}$ to be in the elastic domain is*

$$d(\boldsymbol{E}_{\kappa_r}, \boldsymbol{e}_{tr}; \boldsymbol{\Pi}) < \mathcal{T}(\boldsymbol{e}_{tr}, \boldsymbol{\Pi}),$$

for all admissible values of $\boldsymbol{\Pi}$.

In this manner we have a description of the elastic domain; however, we do not have a practical characterization of the rate $\boldsymbol{L}_p$ yet. Actually, we still need two other theorems to obtain a more efficient picture (as above, we refer to [80] for the proofs).

Let us indicate with $\mathcal{X}$ the range of the function $\hat{\boldsymbol{X}}$ for $\boldsymbol{e}_{\text{tr}}$ fixed. This is a subset of a nine-dimensional Euclidean space, called X-space. The following theorem provides an equivalent formulation of the maximum rate of dissipation criterion by working in the range $\mathcal{X}$.

Theorem 1.3.5. *Let us give the Helmholtz potential $\hat{\psi}(\boldsymbol{E}_{\kappa_r}, \boldsymbol{e}_{tr})$ such that the driving force $\hat{\boldsymbol{X}}$ related to it is an open map. Then there exist functions $\hat{\boldsymbol{L}}_p(\boldsymbol{E}_{\kappa_r}, \boldsymbol{e}_{tr}) = \boldsymbol{L}_p$ and $\hat{\xi}(\boldsymbol{e}_{tr}, \boldsymbol{L}_p) \geq 0$ satisfying* (1.13) *if and only if it is possible to construct functions $\tilde{\boldsymbol{L}}_p(\boldsymbol{X}, \boldsymbol{e}_{tr})$ and $f(\boldsymbol{X}, \boldsymbol{e}_{tr}) \geq 0$ defined on $\mathcal{X}$ such that, for fixed $\boldsymbol{e}_{tr}$:*

1. $\boldsymbol{L}_p = \tilde{\boldsymbol{L}}_p(\hat{\boldsymbol{X}}(\boldsymbol{E}_{\kappa_r}, \boldsymbol{e}_{tr}), \boldsymbol{e}_{tr}) = \hat{\boldsymbol{L}}_p(\boldsymbol{E}_{\kappa_r}, \boldsymbol{e}_{tr})$,

   $\xi = f(\boldsymbol{X}(\boldsymbol{E}_{\kappa_r}, \boldsymbol{e}_{tr}), \boldsymbol{e}_{tr}) = \hat{\xi}(\boldsymbol{e}_{tr}, \hat{\boldsymbol{L}}_p(\boldsymbol{E}_{\kappa_r}, \boldsymbol{e}_{tr}))$,
2. $\boldsymbol{X} \cdot \tilde{\boldsymbol{L}}_p(\boldsymbol{X}, \boldsymbol{e}_{tr}) = f(\boldsymbol{X}, \boldsymbol{e}_{tr}) \quad \forall \boldsymbol{X} \in \mathcal{X}$,
3. *For fixed $\alpha > 0$, given two tensors $\boldsymbol{X} \neq \boldsymbol{X}_0 \in \mathcal{X}$ such that*

$$f(\boldsymbol{X}, \boldsymbol{e}_{tr}) = \alpha, \qquad f(\boldsymbol{X}_0, \boldsymbol{e}_{tr}) \leq \alpha,$$

   indicating $\boldsymbol{L}_p := \tilde{\boldsymbol{L}}_p(\boldsymbol{X}, \boldsymbol{e}_{tr})$ and $\boldsymbol{L}_{p_0} := \tilde{\boldsymbol{L}}_p(\boldsymbol{X}_0, \boldsymbol{e}_{tr})$, then

$$(\boldsymbol{X} - \boldsymbol{X}_0) \cdot \boldsymbol{L}_p \begin{cases} > 0 & \text{if } \boldsymbol{L}_p \neq \boldsymbol{L}_{p_0}, \\ = 0 & \text{if } \boldsymbol{L}_p = \boldsymbol{L}_{p_0}. \end{cases}$$

We thus obtain that the dependence of $\boldsymbol{L}_p$ and ξ on $\boldsymbol{E}_{\kappa_r}$ can be expressed simply be a dependence on $\boldsymbol{X}$, this result will be recalled in Section 5.1 for the description of our model. The second and the third points of the result correspond to (1.13) and to the maximum rate of dissipation criterion, respectively.

Finally, let us move to the last theorem for a full characterization of $\boldsymbol{L}_p$.

Theorem 1.3.6. *Consider a function $f(\boldsymbol{X}, \boldsymbol{e}_{tr})$ defined on all the X-space (that is the range of $\hat{\boldsymbol{X}}$, varying ψ) such that*

1. $f(\boldsymbol{X}, \boldsymbol{e}_{tr}) \geq 0, \qquad f(\boldsymbol{0}, \boldsymbol{e}_{tr}) = 0$,
2. *the sets $\mathcal{L}(\alpha, \boldsymbol{e}_{tr}) := \{\boldsymbol{X} \mid f(\boldsymbol{X}, \boldsymbol{e}_{tr}) \leq \alpha\}$, that is the level sets of $f(\boldsymbol{X}, \boldsymbol{e}_{tr})$, are convex for each $\alpha > 0$,*
3. *at every point where $f(\boldsymbol{X}, \boldsymbol{e}_{tr})$ is strictly positive, it is differentiable with respect to $\boldsymbol{X}$ and to $\boldsymbol{e}_{tr}$, and $\partial f / \partial \boldsymbol{X}$ is non-zero,*
4. $\lambda f(\boldsymbol{X}, \boldsymbol{e}_{tr}) > f(\lambda \boldsymbol{X}, \boldsymbol{e}_{tr})$ *for* $0 < \lambda < 1$, *if* $f(\boldsymbol{X}, \boldsymbol{e}_{tr}) > 0$.

If, for any choice of $\hat{\psi}$ twice differentiable with respect to $\boldsymbol{E}_{\kappa_r}$ and $\boldsymbol{e}_{tr}$, f is restricted to $\mathcal{X}$ (the range of $\boldsymbol{X}$ related to the choice of ψ through the definition of the driving force) and, for each $\boldsymbol{X} \in \mathcal{X}$, we define

$$\tilde{\boldsymbol{L}}_p(\boldsymbol{X}, \boldsymbol{e}_{tr}) := \begin{cases} \boldsymbol{0} & \text{if } f(\boldsymbol{X}, \boldsymbol{e}_{tr}) = 0 \\ \frac{f(\boldsymbol{X}, \boldsymbol{e}_{tr})}{\boldsymbol{X} \cdot \partial f / \partial \boldsymbol{X}} \frac{\partial f}{\partial \boldsymbol{X}} & \text{if } f(\boldsymbol{X}, \boldsymbol{e}_{tr}) > 0 \end{cases}$$

then $\boldsymbol{L}_p = \tilde{\boldsymbol{L}}_p(\boldsymbol{E}_{\kappa_r}, \boldsymbol{e}_{tr})$ and $\xi = \hat{\xi}(\boldsymbol{e}_{tr}, \boldsymbol{L}_p)$ satisfy equation (1.13).

This last results complete Rajagopal's theory providing the ingredients to model the material behavior by the use of the Helmholtz potential ψ and of the rate of dissipation f. While the first one is related to the stress by (1.11), the second one easily gives us the flow rule for the natural configuration. It is important to underline that these two functions are linked through the maximum rate of dissipation criterion but can be chosen separately.
All this theory will be used in building up the model of Chapter 5, by introducing two main assumptions: *quasi-staticity* of the process and small strain regime. These hypothesis lead to easier expressions for the driving force $\boldsymbol{X}$ and the strain rate $\boldsymbol{L}_p$ as explained below.

1.3.4 Quasi-static processes

In order to understand the kind of hypothesis that we want to do and its consequences, let us try to understand what happens to the system described by Rajagopal's theory from the dynamical point of view. Let us suppose to deform our material in a configuration that is outside the current elastic domain. This deformation causes a change in the natural configuration: intuitively, this change is going to be fast at the beginning and slower when the new elastic domain approaches the current configuration until including it. In particular, let us consider a constant $\boldsymbol{E}_{\kappa_r}$ outside the initial elastic domain. The rate $\boldsymbol{L}_p$ should have a non-zero value and approach $\boldsymbol{0}$ as the natural configuration $\boldsymbol{e}_{\text{tr}}$ induces an elastic domain that is closer to include $\boldsymbol{E}_{\kappa_r}$. In this way, $\boldsymbol{L}_p$ creates a trajectory in the X-space that goes towards the border of the elastic domain from outside. We call *relaxation time* the characteristic time of this process, determined by the time constants associated to the constitutive equations.
In this sense, the process is considered *quasi-static* when this relaxation time is much smaller than the characteristic time of the macroscopical evolution.
The consequence of this assumption is that the trajectory created by $\boldsymbol{L}_p$ approaching $\boldsymbol{0}$ in the X-space actually lies on the boundary of the elastic domain. It becomes quite

interesting to notice that we obtain kind of a contradiction. On one hand, since $\boldsymbol{L}_p$ is continuous in $\boldsymbol{E}_{\kappa_r}$ it should be null along all the boundary of the elastic domain, thus implying that on this same boundary there is a constant $\boldsymbol{e}_{\text{tr}}$. On the other hand, the trajectory that rapidly approaches the boundary allows us to find different values of $\boldsymbol{e}_{\text{tr}}$ along all the boundary, as sketched in Figure 1.7. Thus, all the evolution can be supposed to happen along the boundary of the elastic domain.

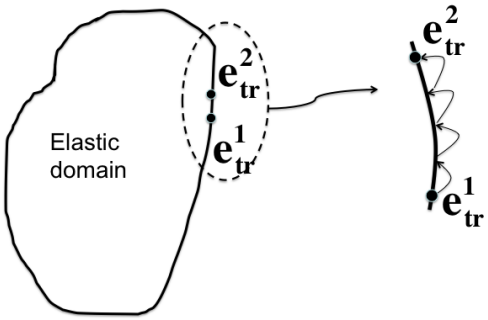

Figure 1.7: Scheme of the trajectory in the X-space in the case of quasi-static evolution, leading to different values of $\boldsymbol{e}_{\text{tr}}$ along the boundary of the elastic domain.

1.3.5 Linearization

In this section we introduce an assumption that will be used both in the model of Chapter 5 and in the treatment of the experimental data in Chapter 2. We suppose that the natural configuration is very close to the original reference configuration, that is

$$\boldsymbol{e}_{\text{tr}} = \boldsymbol{I} + \boldsymbol{e}_1, \tag{1.14}$$

where $||\boldsymbol{e}_1|| = \varepsilon \ll 1$. We can now rewrite some of the equations in Section 1.3.2 by neglecting the terms that are $o(\varepsilon)$.
As for starters, the driving force $\boldsymbol{X}$ defined by (1.12) can be re-written as follows

$$\boldsymbol{X} = -\varrho \frac{\partial \hat{\psi}}{\partial \boldsymbol{e}_{\text{tr}}},$$

where we neglected the term $-\varrho \frac{\partial \hat{\psi}}{\partial \boldsymbol{e}_{\text{tr}}} \boldsymbol{e}_1^T = o(\varepsilon)$.
Anagously, we can simplify the expression of $\boldsymbol{L}_p$ as

$$\boldsymbol{L}_p = \dot{\boldsymbol{e}}_{\text{tr}} \boldsymbol{e}_{\text{tr}}^{-1} = \dot{\boldsymbol{e}}_{\text{tr}}.$$

We can also expand the dissipation function as

$$f(\boldsymbol{X}, \boldsymbol{e}_{\text{tr}}) = f(\boldsymbol{0}, \boldsymbol{e}_{\text{tr}}) + \frac{\partial f}{\partial \boldsymbol{X}} \cdot \boldsymbol{X} = \frac{\partial f}{\partial \boldsymbol{X}} \cdot \boldsymbol{X},$$

where we used $f(\boldsymbol{0}, \boldsymbol{e}_{\text{tr}}) = 0$. Eventually, this leads to an expression of the natural configuration variation, that is

$$\dot{\boldsymbol{e}}_{\text{tr}} = \begin{cases} \boldsymbol{0} & \text{in the elastic domain,} \\ \alpha \frac{\partial f(\boldsymbol{X}, \boldsymbol{e}_{\text{tr}})}{\partial \boldsymbol{X}} & \text{outside the elastic domain.} \end{cases} \tag{1.15}$$

In closing, we can also simplify the total strain $\boldsymbol{E}_{\kappa_r}$ by using the linear version $\boldsymbol{\varepsilon} = \text{sym}(\boldsymbol{F}_{\kappa_r} - \boldsymbol{I})$.
All these relations are recalled in Chapter 5 when detailing our model.

CHAPTER 2

Experimental Setting and Grid Method

In this chapter we detail the test we performed ad IFMA (Institut Français de Mécanique Avancée) laboratories in Clermont-Ferrand. We combined a device that guarantees uniaxiality of a slow-rate load and a full-field measurement technique for the data treatment, as described in the following sections.

2.1 Materials and methods

In this section we describe the characteristics of our main experiment. We start by introducing the super-elastic SMA specimen that we used and we continue by detailing the experimental setting for our mechanical traction test and the novelties that characterize it.

2.1.1 Specimen composition and crystallographic properties

Our experiment was performed on a $\mathrm{Cu\,Al_{11.4}\,Be_{0.5}}$ (wt.%) single crystal with a martensite-start temperature equal to $-2\,^{\circ}\mathrm{C}$, whose geometry is shown in Figure 2.1. In order to avoid damage or sliding of the specimen during the uniaxial tensile test, aluminum tabs were bonded at its ends. The external conditions, first of all the gripping device can strongly affect the transformation in several ways. From the mathematical

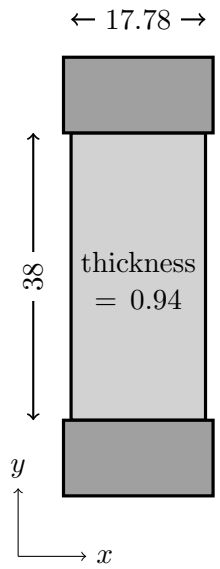

Figure 2.1: Geometry and dimensions of the Cu Al Be specimen.

point of view it is possible to show the influence of the grips on the specimen by taking into account long-range interactions [78]. In parallel, it is possible to experimentally show that the transformation can change from one region to the other one of the specimen because of the different external conditions, like presence of grips or external means that could affect thermal diffusion [86]. In our case, the tabs have been precedently glued on the specimen with a special stiff glue that avoids slides. Their influence has not been treated in this thesis but some analysis can be found in [31] for the same specimen. Without considering the aluminum tabs, our specimen has dimensions equal to $17.78 \times 38 \times 0.94$ mm^3 along x- y- and z-directions, respectively.

The test was performed at a room temperature equal to $T_{\text{amb}} = 26.8°\text{C}$. As T_{amb} is higher than the martensite-start temperature, the specimen is in the austenitic state as zero stress. The austenitic phase is cubic, with axes $([1,0,0],[0,1,0],[0,0,1])$. The rotation matrix from the austenitic axes to the specimen axes (x, y, z) indicated in Figure 2.1 was determined by X-ray diffraction in a previous work in which the same specimen was employed [31]:

$$R = \begin{bmatrix} -0.6612 & 0.0721 & 0.7467 \\ -0.0049 & -0.9958 & 0.0918 \\ 0.7502 & 0.0570 & 0.6588 \end{bmatrix}.$$

The alloy undergoes a cubic to M18R-monoclinic transformation, thus involving twelve variants of martensite [19]. The number of variants involved in the transformation derives from the relation between the crystal symmetry in austenite and the one in the martensitic phase, as already explained in Section 1.2.2. The indication M18R refers to the kind of monoclinic crystal structure, that comes from a suitable combination of 18 atomic planes, as detailed in [12]. In our case, the Bain matrices of the martensite variants, as defined in section 1.2.2, are the following ones

$$\mathbf{U_1} = \begin{pmatrix} \beta & 0 & 0 \\ 0 & \rho & \sigma \\ 0 & \sigma & \tau \end{pmatrix} \qquad \mathbf{U_2} = \begin{pmatrix} \beta & 0 & 0 \\ 0 & \rho & -\sigma \\ 0 & -\sigma & \tau \end{pmatrix} \qquad \mathbf{U_3} = \begin{pmatrix} \beta & 0 & 0 \\ 0 & \tau & \sigma \\ 0 & \sigma & \rho \end{pmatrix}$$

$$\mathbf{U_4} = \begin{pmatrix} \beta & 0 & 0 \\ 0 & \tau & -\sigma \\ 0 & -\sigma & \rho \end{pmatrix} \qquad \mathbf{U_5} = \begin{pmatrix} \tau & 0 & \sigma \\ 0 & \beta & 0 \\ \sigma & 0 & \rho \end{pmatrix} \qquad \mathbf{U_6} = \begin{pmatrix} \tau & 0 & -\sigma \\ 0 & \beta & 0 \\ -\sigma & 0 & \rho \end{pmatrix}$$

$$\mathbf{U_7} = \begin{pmatrix} \rho & 0 & \sigma \\ 0 & \beta & 0 \\ \sigma & 0 & \tau \end{pmatrix} \qquad \mathbf{U_8} = \begin{pmatrix} \rho & 0 & -\sigma \\ 0 & \beta & 0 \\ -\sigma & 0 & \tau \end{pmatrix} \qquad \mathbf{U_9} = \begin{pmatrix} \rho & \sigma & 0 \\ \sigma & \tau & 0 \\ 0 & 0 & \beta \end{pmatrix}$$

$$\mathbf{U_{10}} = \begin{pmatrix} \rho & -\sigma & 0 \\ -\sigma & \tau & 0 \\ 0 & 0 & \beta \end{pmatrix} \qquad \mathbf{U_{11}} = \begin{pmatrix} \tau & \sigma & 0 \\ \sigma & \rho & 0 \\ 0 & 0 & \beta \end{pmatrix} \qquad \mathbf{U_{12}} = \begin{pmatrix} \tau & -\sigma & 0 \\ -\sigma & \rho & 0 \\ 0 & 0 & \beta \end{pmatrix}$$

where $\beta = 0.9044,\ \rho = 1.0062,\ \tau = 1.0832$ and $\sigma = 0.0227$ are the so-called stretch parameters [31]. The structure of the Bain matrices is derived in [53, 75] while the values of the stretch parameteres have been deduced in [31] exactly for this specimen. Moreover, the single variants of martensite are individually compatible with austenite, according to the definitions given in 1.2.3, and it is possible to compute the *habit planes* corresponding to each austenite-martensite variant combination.

2.1.2 Experimental setup and loading conditions

Both strain- and stress-controlled tests on SMAs are usually performed by using retro-active controlled devices. These devices allow a good degree of automatism in the experiment and permit to focus on the data acquisition. On the other hand, this kind

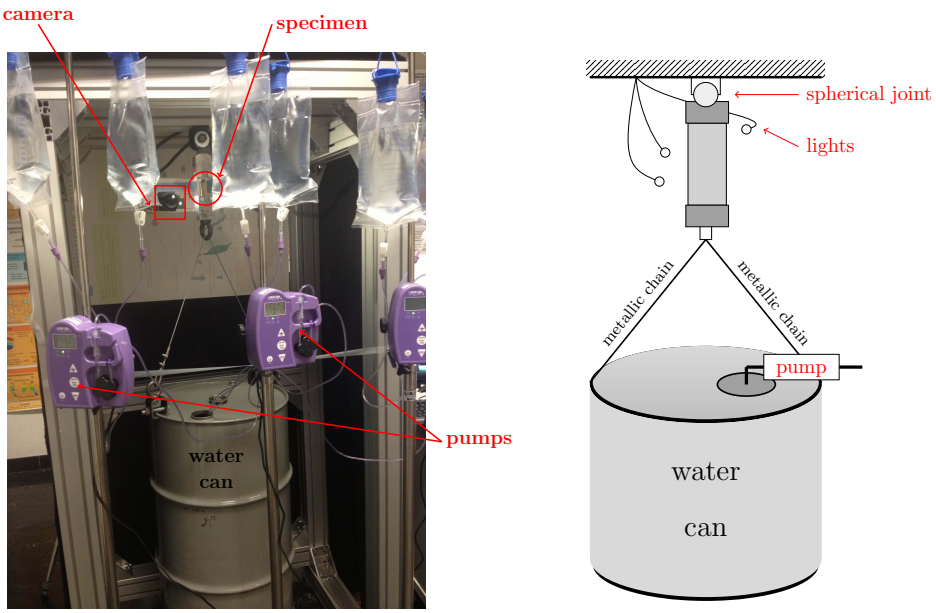

Figure 2.2: Picture and scheme of the experimental setting described in Section 2.1.2

of devices becomes useless when the focus of the test is to find out the presence of intermittency in the transformation. The usual testing machines are based on sensors and actuators, both with their own properties, in terms of resolution and response, integrated in a PID (Proportional-Integral-Derivative) controller. This kind of control makes the loading variable fluctuate around the required values for each step of the test. The problem is that these oscillations are not predictable so that it is impossible to distinguish this experimental bias from the microscopical transformation intermittency.

In order to avoid this drawback, a non-classical experimental setup has been designed. A schematic view of this setting is shown in Figure 2.2.

The top of the specimen was connected to the top of the structure through a spherical joint, so that rotation around the vertical axis was allowed. At the other end of the specimen there was a suspended can, which was slowly filled by water during all the experiment. We thus obtain a stress-controlled test with two very important features:

- both the spherical joint on the top of the specimen and the joint to the can at the bottom allow rotations. This enables us to apply a perfect uni-axial tensile loading, that is not possible in classical tensile machines;

- the use of gravity guarantees monotonicity and uni-axiality of the loading but above all it allows for uni-directionality. In this way, we avoid the fluctuations in the results that could be due to variations in the loading direction.

The flux of water was controlled and held constant by electronic pumps and it was possible to reverse it, thus obtaining both loading and unloading of the specimen. Moreover, the velocity of the loading was easily verifiable. It was possible to choose a slow loading rate and assume a *quasi*-static transformation, according to the definition of *quasi*-staticity given in Section 1.3.4. Some further remark on the satisfaction of this hypothesis is detailed in Section 3.1.3.

As already said, the test was performed at a constant room temperature $T_{\text{amb}} = 26.8°\text{C}$. At this temperature the specimen was purely austenitic as we are far from the transition temperature (since $M_{\text{s}} = -2\,°\text{C}$ as in section 2.1.1). We induced the martensitic transformation by loading, and successively reversed it by unloading. It is important to underline that the transformation stress strongly depends on temperature. This dependence implies that the stability of temperature has to be insured during the whole test, since slight modifications of this external factor would definitely affect the results. Moreover, the very slow loading rate insures that local temperature changes due to phase transformation (this phenomenon is accompanied by latent heat [84]) remain negligible, and thus do not influence the observed phenomena, which is not the case with usual loading rates applied with tensile machines.

Super-elastic shape memory alloys usually show the following behavior when loaded: a first elastic part in the austenitic phase, followed by a *transformation plateau* when the martensitic transition starts. During this transformation plateau, small changes in the stress will induce strain jumps related to the appearance of martensite. By keeping in mind this behavior, the loading conditions we applied during the test are the following ones.

- Before the test, we applied a preliminary fast load-unload cycle to optimize the position of the camera that we used to record the data;
- We pre-loaded the specimen by filling the can with an initial quantity of water, in order to skip the first elastic deformation part and reduce the duration of the test. We performed some preliminary tests to estimate the starting point of the transformation and avoid to overload the specimen with this initial load. Actually, it is important to slowly reach the plateau in order not to lose any information about the phase transition. By taking into account these difficulties, we chose to apply a pre-load equal to $34.37\,\text{MPa}$;
- We loaded the specimen at a constant rate equal to $1.055\,\text{MPa/h}$ until we reached

a final load of 57.29 MPa, that enables a complete transformation to martensite. The duration of this loading phase was thus about 22 hours;

- The unloading was slightly slower, with a rate of -0.915 MPa/h down to 35.95 MPa. This value was reached after more or less 23 hours and 15 minutes.

During the test it was necessary to stop loading each 97 minutes in order to save the data recorded by the camera and clear its memory. During this phase we paid particular attention to not to touch or perturb the whole system, though some effects on the data seem to be unavoidable, as explained in Section 3.1.2.
It is worth noticing that usual testing machines are not intended to be used with such a low loading rate and they are not designed for that. In our case, much slower rates (say at least hundred times slower) could even be reached: we chose our rates in order to obtain a good compromise between the duration of the test and the need for *quasi*-static conditions.
The same kind of procedure has also been used in [23] but with a faster water flux compared to ours (around 37.55 MPa/h in the gauge zone of the specimen, which is about 35 times faster than in our study).

2.2 Grid method

Here we describe the features of the method we used for the determination of the strain maps, the *grid method*. We describe the ideas behind this method and we rapidly compare it to other similar techniques. Moreover, we provide an estimate for the strain resolution. Afterwards, we detail the phases of the preparation of the specimen and of the image acquisition and processing.

2.2.1 Theoretical basis of the method

The grid method is one of the full-field measurement techniques which are currently available. These techniques have recently spread within the Experimental Mechanics community. They are indeed very attractive since they provide *fields* of measurements, which clearly represent a breakthrough compared to more classic measurement means such as displacement sensors or strain gauges. The most used and known methods of this genre, in addition to the grid method, are digital image correlation (DIC), moiré interferometry and speckle interferometry. All these techniques have the possibility to provide displacement fields (and thus strain fields after derivation, within certain limits due to noise) on a spatial region of the specimen under test. The size of this region depends on various parameters, the main one being the number of pixels of the camera

sensors, but current cameras enable us to investigate specimen featuring dimensions of the order of some squared centimeters.
Interference methods, like interferometric moiré or speckle interferometry, rely on the interference produced by two coherent laser beams on the specimen. These interference methods are characterized by their high sensitivity. The consequence is that they are also very perceptive to parasite vibrations, so that their use in industry is limited in practice.
Conversely, the grid method and the DIC method belong to the class of *white light* measurement methods. All these methods relate the displacement to the spatial variation of the light intensity. The DIC technique is quite immediate to use since the preparation of the surface specimen is very simple. On the other hand, the displacement is the solution of an implicit equation which is solved iteratively.

Concerning the grid method, the drawback with respect to DIC is that the preparation of the specimen (detailed in Section 2.2.3) needs more effort since a regular marking has to be deposited or printed on the surface of the specimen. Even if recent attempts show that out-of-plane displacements can be measured by diffracting the observed grid [69], only 2D displacement and strain components can be easily measured. The positive aspect is that the determination of the displacement from the measurements is straightforward, so no iterative algorithm is necessary.
The post-processing of the images is consequently fast enough to calculate the displacement components with the same procedure at any pixel of the images, without any interpolation. This feature makes the method particularly suitable for our analysis since we are interested in measuring very local strain changes and we are going to work with a big amount of data, as later explained. Moreover, we are studying only one specimen so that the preparation of the surface has to be done only once. Note finally that we perform the same of calculation at any pixel, but the measurement provided at any pixel is not independent from the ones given at the surrounding pixels because of the data treatment described below. The so-called spatial resolution is therefore not equal to one pixel, but to a greater quantity (see below).

The idea at the basis of the grid method is simply geometrical: by analyzing the deformation of a grid suitably deposited on the specimen, we can deduce some information on the specimen itself. As will be explained in section 2.2.3, a grid is deposited on a surface of the specimen. Pictures of this surface are then taken during the whole test. The first fundamental assumption of the technique is that the grid deforms exactly

like the specimen on which it is transferred using a thin layer of glue. Moreover,it is plausible to suppose that the stiffness of the glue layer is negligible compared to the stiffness of the metallic specimen, in order to consider the method as non-intrusive.

Initially, the grid is a spatial carrier whose lines are periodically distributed with a given distance between each other. This distance is denoted by p and called the *grid pitch*. We can thus characterize each grid by introducing a frequency vector $\boldsymbol{f} = f\,\boldsymbol{n} = \boldsymbol{n}/p$, where $\boldsymbol{n}$ is the unity vector perpendicular to the grid lines. In the undeformed configuration, we can express the light intensity as

$$S(\boldsymbol{R}) = A[1 + \gamma \mathrm{frgn}(2\pi \boldsymbol{f} \cdot \boldsymbol{R})], \tag{2.1}$$

where $\boldsymbol{R} = (X, Y)$ is a point in the reference configuration, A is the amplitude, γ the contrast, and frgn a 2π-periodic function [11]. Let us indicate by $\boldsymbol{U}(\boldsymbol{R})$ the displacement field, so that the material point $\boldsymbol{R}$ occupies the position $\boldsymbol{r} = \boldsymbol{R} + \boldsymbol{U}(\boldsymbol{R})$ after deformation. We can also reverse this relation by introducing the displacement field on the deformed configuration $\boldsymbol{u}(\boldsymbol{r})$ such that $\boldsymbol{R} = \boldsymbol{r} + \boldsymbol{u}(\boldsymbol{r})$.
Since we are focusing on a material point, the light intensity in $\boldsymbol{r} = (x, y)$ and $\boldsymbol{R}$ has to be the same, that is

$$s(\boldsymbol{r}) = S(\boldsymbol{R}) = S(\boldsymbol{r} + \boldsymbol{u}(\boldsymbol{r})).$$

By consequence, we can write

$$s(\boldsymbol{r}) = A[1 + \gamma \mathrm{frgn}(2\pi \boldsymbol{f} \cdot \boldsymbol{r} + \phi(\boldsymbol{u}))],$$

where $\phi(\boldsymbol{u})$ is the total phase modulation of the grid. There are actually two phases: one along each direction. They are denoted by ϕ_x and ϕ_y for the x- and y-axis, respectively. Thus, by using the Cartesian coordinates, we can express the x- and y-components of the displacement with respect to the reference configuration as

$$\begin{cases} u_x = -\dfrac{p}{2\pi}\,\Delta\phi_x, \\ \\ u_y = -\dfrac{p}{2\pi}\,\Delta\phi_y, \end{cases} \tag{2.2}$$

where $\Delta\phi_i, i = x, y$ represent the phase changes between current and reference grid images. Therefore, the unknown that has to be provided by the algorithm is the phase distribution for each grid image, while it is not necessary to measure the mean intensity A and the contrast γ for the problem at hand. Also the frgn function is not really known but it is periodic and Fourier analysis can therefore be employed to study it, in

particular to extract its phase, as discussed below.

There are different methods for the calculation of the phase. On one hand, it is possible to use a global Fourier transform and isolate it in a suitable neighborhood of the frequency of the reference configuration $\boldsymbol{f}$, thus obtaining an estimate of the quantity $2\pi \boldsymbol{f} \cdot \boldsymbol{r} + \phi(\boldsymbol{u})$. This method does not require the knowledge of the other quantities (A and γ) and it is quite fast, but provides results with a certain amount of uncertainty that can be reduced by using a local method. The method we used is the *Windowed-Fourier Transform* (WFT) algorithm which enables us to retrieve a localized information. The WFT is written as follows :

$$\phi(x,y,\theta) = \int_{-\infty}^{+\infty} \int_{-\infty}^{+\infty} s(\xi,\eta) g(\xi - x, \eta - y) \exp\{-i2\pi f(\xi\cos(\theta) + \eta\sin(\theta))\} d\xi d\eta, \tag{2.3}$$

where $g(x,y)$ is a suitable window discussed briefly below and θ an angle which is equal to 0 (resp. $\pi/2$) when investigating the $x-$ (resp. $y-$) direction. Since only the phase of each of the two superimposed line patterns has to be found (it is not necessary to determine A and γ in the problem at hand), this quantity is directly given by the phase of the WFT calculated at any pixel. Indeed, the phase of the WFT and the sought phase are generally considered as being equal within a constant angle which disappears when calculating the difference in phase between current and reference images ([91]). However, it has been shown recently that the phase of the WFT is equal, as a first approximation, to the sought phase *convolved* by the window of the WFT, plus the same preceding constant angle [93]. This means that the phase maps, and thus the phase derivative, displacement and strain maps, are blurred, the blurring intensity being merely driven by the width of the window. It also means that the actual values for these quantities can theoretically be retrieved by deconvolution [45] but this question is a problem as such which has not been addressed during this thesis.

The nature of the window $g(x,y)$ influences the quality of the results. It is proposed in [91] to employ a triangular function for $g(x,y)$. The advantage is to have a width which can be very small (twice the pitch value as a minimum), thus assuring a very good spatial resolution (defined here as the minimum distance between two localized measurements). The drawback is that the measurement resolution (defined as the smallest measurement that emerges from the noise floor) is impaired in proportion. In addition, it can be shown that, since the frng function is generally not a pure sine function in practice, harmonics may potentially affect the strain field if the width of the triangle is not an integer value multiple of the grid pitch. A Gaussian function has been

proposed and employed in [10, 11]. It is defined by

$$g(x,y) = \frac{1}{2\pi\sigma^2} exp\left(-\frac{x^2+y^2}{2\sigma^2}\right),$$

where σ is the standard deviation of the distribution characterized by this envelop. The drawback of this choice is that the minimum value for σ is the pitch p of the grid [93]. This affects the minimum width of the envelope which, according to the three-sigma rule, is equal to six times the pitch (three times the minimum value obtained with the triangular window). However, the main advantages are of two kinds. First of all, the problem mentioned above concerning the harmonics is theoretically avoided. Second, it can be shown that we obtain an excellent compromise between resolution and spatial resolution for the order of magnitude of the strain we have in our problem.
We decided to use this type of window in this study. Since in our case the grid pitch employed is equal to 0.2 mm, this gives a spatial resolution equal to 1.2 mm. The strain resolution is discussed below in Section 2.2.2.

Once the displacement is known by using Equation 2.2, the strain can be merely obtained by differentiation if noise is sufficiently filtered by a relevant choice of the kernel width, like in our case. However, the problem is that slight grid defects, such as pitch fluctuations, affect the phase, and by consequence displacement and above all strain distributions. These fluctuations are due to the grid printing. The consequence of these fluctuations is generally not visible to the naked eye when looking at the displacement maps, but it is severely amplified by differentiation when calculating the strain components. A compensation technique has been proposed in [10, 11] to significantly limit this effect. It consists in mapping the phase derivative maps in the reference coordinate system prior to subtracting current and reference phase derivative maps. This technique has been employed in the current work, since significant parasitic fringes due to grid defects have been detected in the phase derivative maps.

Another point is the fact that phase maps (and thus potentially displacement maps) are affected by phase (or displacement) jumps in some cases. This phenomenon occurs when the displacement over a given image is greater than the grid pitch and it is due to the discontinuity in the $\arctan$ function. As we said, we work under a small strain assumption that does not imply also small displacements, so that we actually obtain phase jumps in our case. The problem was solved by using a so-called *unwrapping* algorithm which re-establishes the continuity of the phase distributions when necessary. On the other hand, the small strain assumption allows us to calculate the linearized strain components. Actually, the grid method also provides the possibility to deal with

large strains and in that case the analysis would probably be more precise but would also require longer post-processing times.

2.2.2 Strain resolution

In this section we aim at assessing the strain resolution of our measurement technique. This point is crucial in order to determine a threshold value to distinguish actual events from noise in strain maps. Specific studies have been carried out in [46, 92, 93] in order to estimate the strain resolution of the method by taking into account the propagation of the noise due to the camera sensor. The estimation starts from the images taken by the camera, without any kind of treatment. If a Gaussian envelope is use in the WFT, the noise level in displacement and strain maps due to camera sensor noise propagation is given by the following expression [46, 93]:

$$\sigma_\varepsilon(x,y) = p\left(\frac{9\sqrt{2}}{2\pi^{3/2}}\right)\left(\frac{\sqrt{\Delta_x\,\Delta_y}}{K}\right)\frac{\sigma_{\text{image}}}{d_\varepsilon^2}, \tag{2.4}$$

where $p = 5$ pixels is the grid pitch, $\Delta_x \times \Delta_y$ represents the pixel size (and since we are measuring everything in pixels, $\Delta_x = \Delta_y = 1$), d_ε is the spatial resolution estimated at the end of section 2.2.1, so $d_\varepsilon = 6 \times \sigma$, σ_{image} is the standard deviation of the noise in the grid images and K the modulus of the WFT : $K(x,y) = |\phi(x,y)|$. To obtain this result, it is assumed in [94] that the noise is Gaussian and homoscedastic, that is σ_{image} is constant throughout each image. However, it has recently been shown in [46] that this assumption is too rough to precisely assess the noise level. Actual noise is Poisson-Gaussian and heteroscedastic in images, as classically observed and admitted in the image processing community [35].
The noise variance for each point of the picture is thus shown to be linearly related to the light intensity of the pixel under consideration [92]:

$$v(x,y) = \text{Var}\left(s(x,y)\right) = a\,s(x,y) + b, \tag{2.5}$$

where the parameters a and b depend on the camera. In our case, the two parameters have been estimated in [92]: $a = 8.4547$ and $b = -5378.1$. In [46], it is proposed to employ the so-called Generalized Anscombe Tranform to change the nature of the noise in grid images from a Poisson-Gaussian heteroscedastic noise to a Gaussian homoscedastic one [2, 65] and to employ a specific image processing to limit the effect of micro-movements which occur when taking the images. These procedures are necessary for a precise and pixelwise estimation of the noise level. In this thesis, since we are interested in a global value, we use a simplified approch which consists in the following steps:

- taking a grid image and estimate the variance distribution by using Equation 2.5;
- deducing a global equivalent value throughout each image which is defined as

$$\sigma = \sigma_{\text{im}}^{\text{eq}} = \sqrt{\frac{1}{N}\sum_{i=1}^{N}\sigma_{\varepsilon}^{2}(x_i, y_i)},$$

  where N is the number of pixels in the image;
- using Equation 2.4 in order to predict the global noise level in a strain map.

Finally, the grid images were averaged over $N = 128$ frames to reduce the noise level. This procedure takes quite a long time for each image (slightly more than one minute), which means that micro-movements between camera and specimen that are observed to occur during this type of experiment influence the grid image resulting from this averaging procedure. Indeed, it has been shown recently that the mean image is a biased estimator of the noise-free image because of these micro-movements, but that the resulting phases which are then extracted from this mean image (and thus the resulting displacement and strain maps) remain unaffected in practice for the amplitude of the micro-movements observed in the laboratory [94]. Consequently, the estimation in Equation 2.4 can be reasonably divided by $\sqrt{N}$ to account for this procedure on the final standard deviation. By applying this procedure, we eventually obtain an estimate for the strain resolution equal to $\sigma = 5.2 \cdot 10^{-5}$.

2.2.3 Preparation of the specimen

The preparation of the specimen takes some day and is a fundamental part of the method since slight imperfections in depositing the grid can strongly affect the results. In our case, the grid is printed on a polymeric substrate with a high definition printing machine (12000 dots per inch (dpi) resolution) by specialized laboratories. It is important to underline that the grid can deform without cracking or breaking until a strain about $18\,\%$. This property becomes particularly important when dealing with super-elastic materials like SMAs. In our case, the maximum strain that we reached was about $9\,\%$, thus assuring no breaking for the grid.

The surface of the specimen was initially degreased and cleaned. The grid was then glued on the clean surface by using a suitable white adhesive. In particular, we used an $\text{E}504$ glue provided by Epotechny, France. The choice of the white color for the glue is done in order to maximize the contrast between this substrate and the black lines of the grid since, as shown in Section 2.2.2, a higher contrast implies better results. During the gluing phase, it is particularly important to pay attention to the orientation of

the grid lines. The best result consists in having the grid lines parallel to the axes of the coordinate system in which we want to obtain the components of displacement and strain. In our case, we referred to the axes which are parallel to the borders of the gauge section of the specimen.

In general, the gluing phase is one of the most difficult parts of the preparation. First of all, the glue layer has to be very thin (generally some tenth of millimeters [74]) in order to satisfy the assumption of having the grid deformed in the same way as the specimen, as required in section 2.2.1. Moreover, it is necessary to avoid air bubbles in the glue while putting it on the specimen, since they would create defects in the visualization of the outcome.
This first part is followed by a curing phase, which lasts about 40 hours, at a temperature equal to $37\,°$C. At the end of this phase, it is possible to peel off the polymeric substrate on which the grid was printed, so that the grid lines remain glued on the specimen surface.

2.2.4 Image acquisition and processing

The data we recorded during the experiment are pictures of the surface of the specimen on which the grid is deposited. We used a Sensicam QE camera with a 12-bit/1040×1376 pixel sensor and a 105 mm Sigma lens. We chose this kind of camera because a suitable magnification of the lens was sufficient to distinguish the grid lines though the grid pitch was very small (5 pixels, that is more or less 0.2 mm). The camera was positioned on an adjusting stage. In this way, it was easy to set the camera in order to have the pixels of the sensor parallel to the grid lines.
It is important to have a certain uniformity in the lighting of the grid. In particular, the grid has to be uniformly enlightened on an area equal to the kernel of the WFT [93]. In order to satisfy this requirement, it is not necessary to keep brightness constant but it is sufficient to ensure smoothness in the brightness variations. We fulfill this condition by using three flexible and movable light guides fed by a KL 2500 LCD cold light source. Moreover, the cold light improves the contrast, thus allowing a better strain resolution, as explained in Section 2.2.2.

Eventually, we collected about 20.000 images during the whole test (one image every 8.6 seconds more or less). These data required a post-processing phase which took about one month. The treatment was done according to the method detailed in 2.2.1. In particular, we chose the first image (corresponding to the pre-loaded specimen) as the

reference configuration. By comparing each image to the reference one, it was possible to deduce the phase ϕ as described in section 2.2.1. The final output data were the in-plane linearized strain component fields ε_{xx}, ε_{yy} and ε_{xy} and the rotation angle field about the z-direction, ω.

2.3 Conclusions

In this chapter we described the test that we performed and the kind of data that we collected. There are many features that make this test interesting.

- The specimen dimensions are such that most of the transformation is likely going to take place on the surface, that is the part on which we are collecting our information. Actually, the scaling between the behaviour of the transformation within the specimen and on its surface is not known, but we can suppose to approximate our three-dimensional specimen with a two-dimensional plate without losing too much information. Moreover, we have a quite complete description of the specimen from the crystallographic point of view and we are going to use it in order to better understand our data;
- The device that we used does not apply strong boundary conditions on the specimen when compared to classical tensile test devices, so that we tried to minimize the influence of boundaries on the transformation outcome;
- The device guarantees a constant loading direction. Since we are going to analyze the presence of intermittency in the martensitic transition, variations in the direction of the load would affect the results;
- The grid method allowed us to treat a very big amount of images in a quite short period. Moreover, it provided strain maps with a resolution in the range $10^{-5} - 10^{-4}$. This implies that we have many high-resolution two-dimensional maps to be used for our analysis.

Eventually, the combination of our mechanical experimental device and of the image treatment method provided a collection of suitable data for a characterization of the martensitic transformation from several points of view, as we shall do in the following chapters.

CHAPTER 3

Description of the Martensitic Transformation

In this chapter we show some of the results that it is possible to obtain with our data. We start with a comparison with previous experiments on the same specimen in order to underline some features of our experimental device. Then, we describe the martensitic transformation and we deduce some quantities, like the percentage of martensite or the vertical strain. These quantities will show a continuos behavior from the macroscopic point of view but spikes and jumps will appear when looking at their variations.

3.1 Qualitative analysis of the transformation

In this section we provide an overall description of the martensitic transformation undergone by our specimen. First of all, we qualitatively analyze the different strain components and we describe their evolution during the phase transition.
Afterwards, we look at the stress *vs* strain curve and compare it with previous results on the same specimen, though under different testing conditions.
In conclusion, we compare loading phase and unloading one and we spend some words on the beginning of the transformation before the plateau.

3.1.1 Strain components

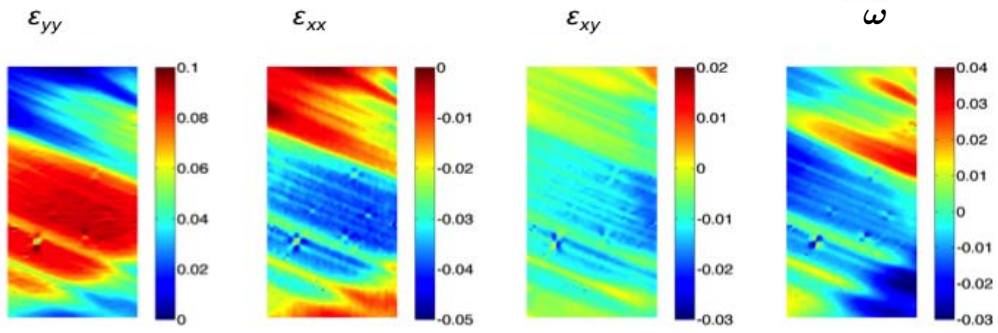

Figure 3.1: Linear strain components ε_{yy}, ε_{xx} and ε_{xy} and in-plane rotation angle ω for $\overline{\varepsilon}_{yy} = 0.057$, that is around the middle of the transformation.

Figure 3.1 shows the maps of the linear strain components obtained with the grid method for a given instant during the transformation, corresponding to $\overline{\varepsilon}_{yy} = 0.057$. As expected, since we are pulling in the vertical direction, ε_{yy} is positive since the specimen is stretching in that direction while ε_{xx} is negative. Moreover, as it is easy to guess, it is exactly the longitudinal vertical component ε_{yy} that shows the biggest values among the strain components. As it is shown in the first map in Figure 3.1, the martensitic zone corresponds to a quite homogeneous zone with strain equal to 0.0914 (by averaging over the red zone) while the austenite is represented by the zero strain level, that is the blue zone.

As regards ε_{xy}, it shows small values and seems to keep a constant sign everywhere except for a small zone in the upper right part of the specimen.

The rotation angle represented in the fourth panel of Figure 3.1 is computed as the skew part of the strain, that is as $1/2(u_{x,y} - u_{y,x})$. It confirms the existence of relative rotations between different zones of the specimen. In particular, we can distinguish abrupt jumps between $+0.03$ radians and -0.03 radiants corresponding with the interfaces between austenite and martensite. These values are in agreement with the values that can be theoretically predicted (see Section 1.2.4 and 3.2.2 for these estimates).

As the vertical component ε_{yy} shows larger variations during the transformation, in the rest of the thesis we focus only on this map when dealing with the macroscopic description of the transformation (for intermittency, we shall use the information of all the components).

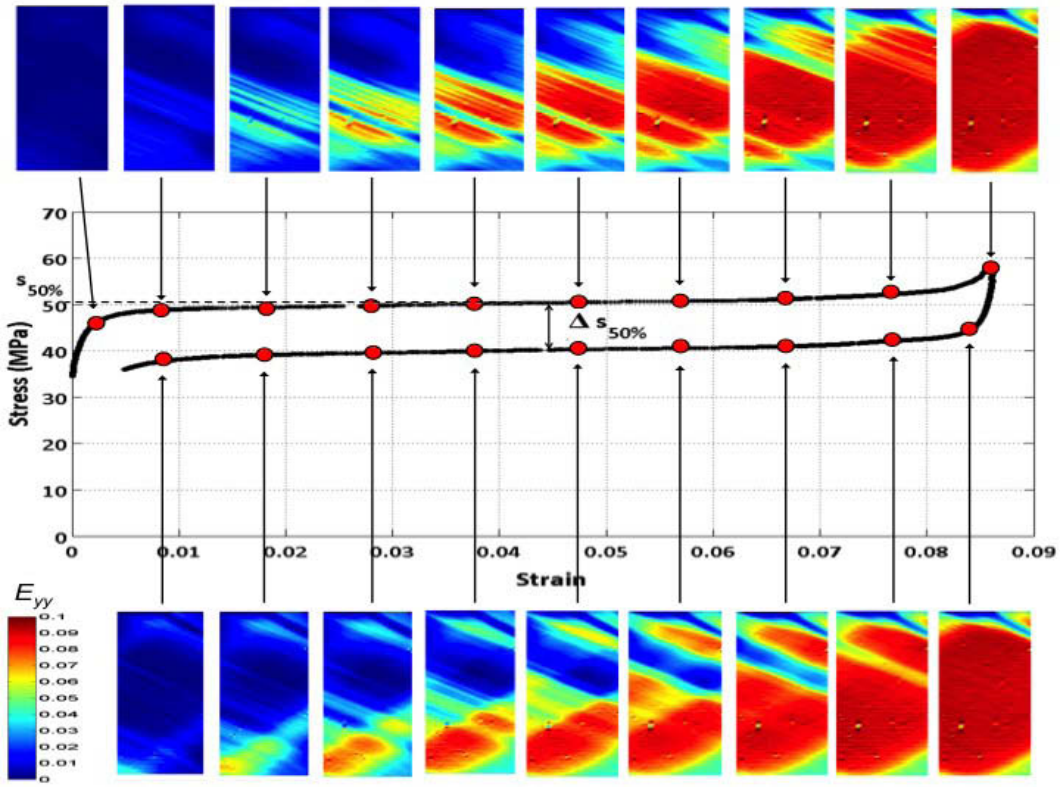

Figure 3.2: Plot of the stress versus strain curve together with the maps of the vertical strain ε_{yy} along the hysteresis loop.

3.1.2 Macroscopic stress versus strain plot

Let us continue our analysis by focusing on the stress *vs* strain curve corresponding to the experiment. This kind of result is usually provided for the experiments on shape memory alloys, so it enables us to start comparing our test with the rest of the experimental literature.

Figure 3.2 shows the stress-strain curve obtained for our experiment. The plotted stress is computed by considering a constant section (equal to the initial one) since we know the weight carried by the specimen. In this computation we obviously use the perfect uni-axiality of our load due to the rotations allowed at the two ends of the specimen (that is a main difference with tests presented in the literature). The strain is the mean of the vertical strain component ε_{yy} over the gauge surface, that is the part of the specimen not covered by the grips at the extremities.

As expected, the specimen exhibits a hysteresis loop in the stress-strain plane. The hysteretic behavior is a consequence of the metastability of the minima for the material, as described in [52], where a link between metastability and the pseudo-elastic hysteresis is provided, and as explained at the end of Section 1.2.1. The maps of the vertical strain that surround the loop can help us understand what is happening in the different parts of the hysteresis.

- At the beginning, there is only elastic deformation, so that the curve shows linearity between stress and strain and no martensite appears in the specimen;
- As the plateau begins, the maps start showing traces of martensite (in red against the blue of austenite) and small increments in stress provide big jumps in the average strain. Actually, during the transition, parts of the specimen switch from austenite (zero strain) to martensite (more or less 9% of strain) so that the average strain is strongly affected by the transition of even small parts of the specimen;
- At the end of the plateau, the most of the specimen is in the martensitic phase except for small zones close to the grips. These zones seem to hardly transform into martensite. The possible reasons for the presence of residual austenite are better detailed in Section 3.2.4.

  Since previous tests assured the resistance of the material only until a load around 58 MPa, we decided not to insist on pulling and we started the unloading.

A more detailed comparison between loading and unloading is done in Secton 3.1.5, but for the moment it is worth to notice that martensite disappears along the plateau of the reverse transformation until a quite complete return to the zero strain state.

Figure 3.2 also shows some missing data during the plateau, for example around a strain equal to 0.026 during loading. It is important to underline that these jumps are not related to the effective transformation events. They are actually due to the pauses we had to take every 97 minutes in order to clear the camera memory, as described in Section 2.1.2. We do not have any information about what happens to the specimen during those breaks but we can assume a combination of noise and small perturbations of the device so that the martensitic transition can likely take place in some small regions. Moreover, the slow loading rate should make the process satisfy the hypothesis of quasi-staticity but it is also possible to have some events still going on when we stop loading for the pause. A wider analysis of the satisfaction of the quasi-staticity assumption can be found in Section 3.1.3. In general, for the rest of the analysis we are going to neglect these strain jumps (they are more or less 4 during the loading plateau and as many for the unloading one) since they cannot be clearly analyzed.

The stress-strain curve in Figure 3.2 is also shown in Figure 5.10 in Section 5.4.2, where it is fitted with the numerical results of the Souza-Auricchio modified model. In addition to the features we shall use for the parameter calibration in section 5.4.2, let us consider some characteristic quantities that can be used to compare our curve with other tests:

- $S_{50\%}$, the stress corresponding to the middle of the plateau during the loading phase;
- m_{load} and m_{unload}, slopes of the plateau during loading and unloading respectively;
- $\Delta\, S_{50\%}$, hysteresis width, *i.e.* the difference between loading and unloading stresses corresponding to the middle of the plateau.

The most effective comparison can probably be done with the results shown in [30, 31] where exactly the same specimen had been tested, though under different test conditions. For simplicity, let us indicate the test in [30] as Test 1 and the test in [31] as Test 2. While our test is detailed in section 2.1.2, let us recall for a moment the features of Test 1 and Test 2.

- A hydraulic testing MTS machine was used in both Test 1 and Test 2, instead of our device.
- The ambient temperature was held constant but around a value equal to $22\,^{\circ}$C, against $26.8\,^{\circ}$C for our test.
- Rotation was not allowed in those tests, since the specimen was strongly constrained by a tensile machine (in our case, a spherical joint permitted rotation). A

scheme of the differences in the boundary conditions is shown in Figure 3.3.

- The test was completely strain-controlled in Test 1 while it was strain-controlled for the loading and stress-controlled for the unloading in Test 2.
- The loading and unloading rates were different from the ones in our test, as shown in table 3.1 through the information on the duration of the plateaus.

Note that the strain obtained in Test 1 and Test 2 is the Hencky strain instead of the linearized strain of our test, but this difference should not affect the main features of the stress versus strain curve.

Table 3.1: Results on the same specimen for the macroscopic stress-strain curve in three different tests: our test and the ones described in [30, 31] and indicated by Test 1 and Test 2, respectively.

Test	T_{amb}	$S_{50\%}$ (in MPa)	m_{load} (in MPa/%)	m_{unload} (in MPa/%)	$\Delta S_{50\%}$ (in MPa)	Duration of the plateau
Present test	26.8 °C	50.34	0.338	-0.353	10.15	load: 5 h unload: 6h
Test 1	22 °C	≈ 34	≈ 0	non linear	≈ 10	load: 50 min unload: 50 min
Test 2	22 °C	≈ 50	≈ 0.5	≈ 3	≈ 22	load: 1.5 min unload: 0.5 min

By keeping in mind these differences, let us compare the features of the loops.

- *Height of the plateau* $S_{50\%}$ — It has already been proven that this feature depends on two factors: the room temperature [70] and the loading rate [73]. In particular, when the room temperature increases it implies a higher value of $S_{50\%}$. Analogously, the higher the loading rate, the higher the plateau. This second relation actually depends on the first one since, by increasing the loading rate, the temperature changes and affects the value of $S_{50\%}$.

  From the comparison between the two slowest tests (present test and Test 1), it can be noticed that the first dependence is verified, since higher temperature corresponds to higher plateau. By comparing our test with Test 2, we can observe that the combination of a higher room temperature and a smaller loading rate leads to a nearly similar value of $S_{50\%}$. Moreover, we do not have any information on how the boundary conditions influence the height of the plateau, but they likely play an important role in determining the value of $S_{50\%}$.

- *Slope of the plateau* m_{load} and m_{unload} — Usually, stress-strain curves obtained for strain-controlled transformations show very flat plateaus. This feature can be explained in two ways. First of all, a strain-controlled test allows a non-monotonicity in the stress, that can increase or decrease, so that it is possible to obtain very small average stress variations. Second, strain-controlled tests are often slower than stress-controlled ones. This implies also less temperature changes that would affect the transformation stress.

  For stress-controlled transformations it is obviously more difficult to provide a flat plateau, since the stress is monotonically increasing and the increasing rate will affect the slope of the plateau. This difference can be observed by comparing m_{load} and m_{unload} for Test 2 in Table 3.1: the first one is obtained from a strain-controlled test and it is clearly smaller than the second one, due to the stress-controlled unload. In this context, it is interesting to observe that the plateau we have obtained by using our stress-controlled device is as flat as the ones obtained for strain-controlled transformations on the same material. This is due to the *quasi*-static conditions we tried to guarantee during the test (whose effect can be also noticed in the smoothness of the experimental curve) and in general to the slow loading rate.
- *Hysteresis width* $\Delta S_{50\%}$ — The width of the hysteresis loop has been related to many features of the transformation and of the material. In general, we can say that the width of the loop is an indication of the dissipated energy [63] (both in the temperature-controlled case described in section 5.3 and in the stress- or strain-controlled transformation).

  This gives a hint on the relation between the loading rate and the hysteresis width: when the loading rate is small there is less dissipation so that the hysteresis loop is smaller and viceversa in the case of fast loading. This is confirmed by our results: the present test and Test 1 maintain a small hysteresis; on the contrary, Test 2, which is faster, provides a bigger hysteresis. Moreover, the change in the kind of loading for Test 2 implies also a non-constant hysteresis width.

Test 2 can be used for a further comparison. Figure 3.3 shows the maps of the vertical strain ε_{yy} almost at the end of the transformation for both the present test and Test 2. Before starting the comparison it is important to specify that the slightly horizontal lines that are present in the map for Test 2 are not physical but are due to the data treatment. In particular, the problem derives from slightly pitch variations that were not erased by the motion compensation technique we used in the present test (as said at the

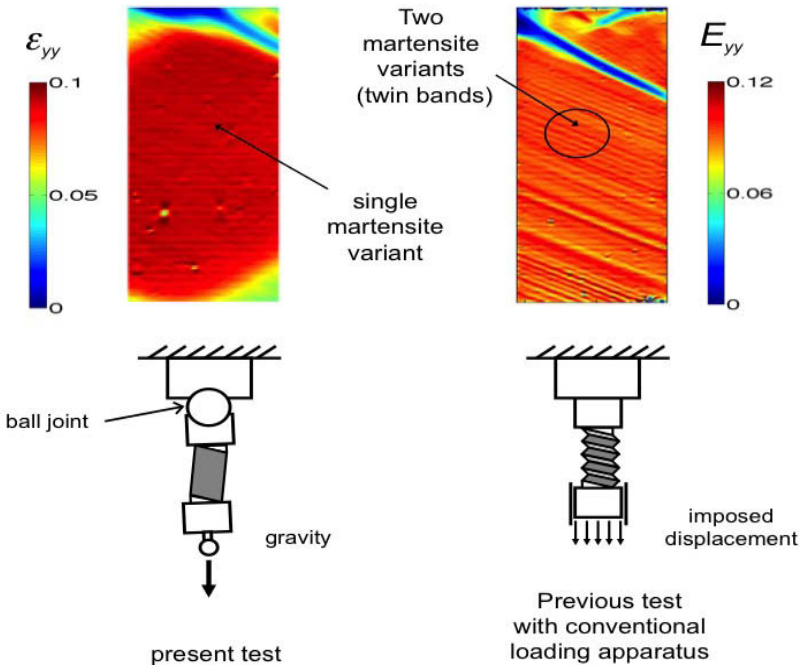

Figure 3.3: Comparison between the present test and Test 2 in terms of longitudinal strain field ε_{yy} when the phase transformation has nearly finished (top). Scheme of the boundary conditions in the two cases (bottom).

end of section 2.2.1). On the other hand, the small dots that can be seen in both images are due to local grid defects. In this case, the compensation technique helps in limiting the effect of their presence on the results but cannot erase them.

In both cases, we can notice the presence of residual austenite (blue region in the maps of Figure 3.3). The main difference between the two experiments can be noted in the martensitic region. As we already stated in Section 3.1.1, in our case we have a basically homogeneous vertical strain. This homogeneity cannot be found in the map corresponding to Test 2, where two different levels of strain are present. On a crystallographic level, this difference is due to two different martensitic rearrangements. In our test it is reasonable to suppose the appearance of a single variant of martensite while in Test 2 we are obtaining a martensite twinning.

The main difference in the two tests that is responsible for this diversity in the results is in the external constraints. As explained at the beginning of this section, no rotation was allowed for the specimen in Test 2. On the contrary, the ball joint used in our experiment permits rotations of the specimen. In particular, in the current test it is possible to obtain a displacement along the horizontal axis at the extremities of the specimen.

To understand how this constrain is related to the appearance of twins or of single vari-

ables, it is necessary to recall Section 1.2. The phase transition from austenite to any variant of martensite corresponds to a large shear strain, whose angle is analytically deducible through the lattice parameters ((1.6)). This implies that having only a variant of martensite is necessarily related to a rotation of the specimen. In cases for which this rotation is not possible, as in Test 2, the appearance of another variant of martensite (for example forming twins) can help restoring uniaxiality.

3.1.3 Time scales and *quasi*-staticity

After the results shown in the previous section it is possible to make some observation on the satisfaction of the quasi-staticity assumption.
First of all, there are many time scales that have to be considered when analyzing the test results:

- time scale of the microscopic events, for which there are some experimental estimates between 10 and 100 μs [71];
- relaxation time, that is the time that the system needs to reach the (metastable) equilibrium, as introduced in Section 1.3.4. This is the time scale on which we do not have any information;
- image acquisition time, in our case equal to 8.6 seconds;
- time scale of the loading, as determined by the loading rate detailed in Section 2.1.2.

The image acquisition time and the loading rate have been empirically chosen in order to balance the duration of the experiment and the number of images recorded for the treatment. The real unknown is the relaxation time: we can only imagine it to be longer that the time scale of the microscopic events. The quantity that matters for the quasi-static assumption is the ratio between this microscopic time scale and the loading time scale, thus unknown.
We can consider several clues both pro and con the satisfaction of the quasi-staticity assumption.
First of all, we have to consider the big strain jumps that are recorded after the breaks we needed to save the data, as explained at the beginning of Section 3.1.2. In practice, we stop the loading for some minute and we record some data before and after this break: we notice strain jumps with bigger orders of magnitude than for the rest of the test at the constant loading rate. This jumps can be caused by the combination of several effects:

- significant external perturbations could affect the whole experimental device, like accidentally touching the hanging can or the water pipes and so on;
- creeping of the material [58];
- the loading rate is not slow enough to make the material reach its (metastable) equilibrium, so that the transformation keeps on progressing with further loading.

The last point would be a clear hint of lack of quasi-staticity, but we obviously do not have any clear information on what really happens.
On the other hand, the comparison between our test and Test 1 and Test 2 as described in Section 3.1.2 provides hints in favour of the quasi-staticity of the process. Actually, the width of the hysteresis seems to be the same as for a faster test, Test 1, though we should consider further differences in the testing conditions (boundary conditions and room temperature). Furthermore, the plateau is shown to be very flat when compared even to strain-controlled tests.
At this level, we do not have enough information to prove that the process is quasi-static and further experimental tests should be performed. As an example, it would be interesting to test the specimen in the same conditions and varying only the loading rates until convergence of the hysteresis loop.
It is interesting to underline that an intermittent behavior on the microscopic scale can be easily related to a quasi-static and rate-indipendent behavior on the macroscopic scale, as explained in [77]. Basically, in an intermittent process the overall dissipation of the system is due to the microscopic bursts that characterize the advancement of the process. A suitable scaling of the number of these events allows the rate-indipendency and the quasi-staticity of the whole final process.

3.1.4 Temporal analysis along longitudinal profiles

In order to start analyzing the big amount of data we have, let us start decomposing the spatial information and focusing on the evolution of three profiles. In particular, let us indicate by $P1, P2$ and $P3$ the vertical sections shown in Figure 3.4 on the vertical strain component map. For each profile, it is possible to show the evolution in time of the strain.
In Figure 3.5 there is the three-dimensional plot of this evolution during only the loading phase for section $P2$ (on one axis there is time, on the other one the vertical component and the height of the plot indicates the strain). By looking at this plot, it is immediately clear that the transformation occurs on a time lapse which is quite small when compared to the whole duration of the loading phase. In particular, the plateau

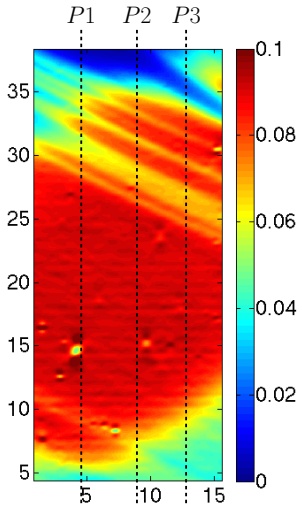

Figure 3.4: Position of the profiles $P1$, $P2$ and $P3$ used for Figures 3.5 and 3.6.

starts at about 14 hours from the beginning of the experiment and ends more or less 5 hours later (less than the 24% of the overall 21-hour load). Moreover, the transformation does not take place homogeneously, neither in space or in time, as it is made clear by figures 3.6 and in agreement with other experimental results [87]. As will be explained in Section 5.4.2, this is one of the reasons why the numerical curve in Figure 5.10 will not exactly fit the experimental stress-strain curve, since the homogeneity condition of the model is clearly unsatisfied by the transformation.

Figure 3.6 shows the two-dimensional view of the strain profile in Figure 3.5 together with the plot for the sections $P1$ and $P3$ and strain profiles corresponding to some fixed times. These plots provide a qualitative idea of how the transformation happens. Firstly, martensite appears along inclined lines (visible in the maps of Figure 3.2), whose trace in the profiles is a localized appearance of strain and that we call *needles* of martensite. They can both appear on one side of the specimen or abruptly cross the whole width (see profiles for $t = 15h$). These needles enlarge and merge, creating larger bands of martensite, while other small needles keep on appearing in other zones of the specimen ($t = 16.5h$). At the end of the loading phase the martensite has quite completely filled the whole specimen ($t = 18.5h$).

As for the spatial information, the transformation seems to start at the middle of the specimen, then moving towards the bottom and from left to right (from $P1$ to $P3$). Afterwards, it starts proceeding towards the top and from right to left. The part of material close to the fixed grip is the last one to transform. Moreover, there is an entire zone, just under the constrained end of the specimen, that remains austenitic, as already said

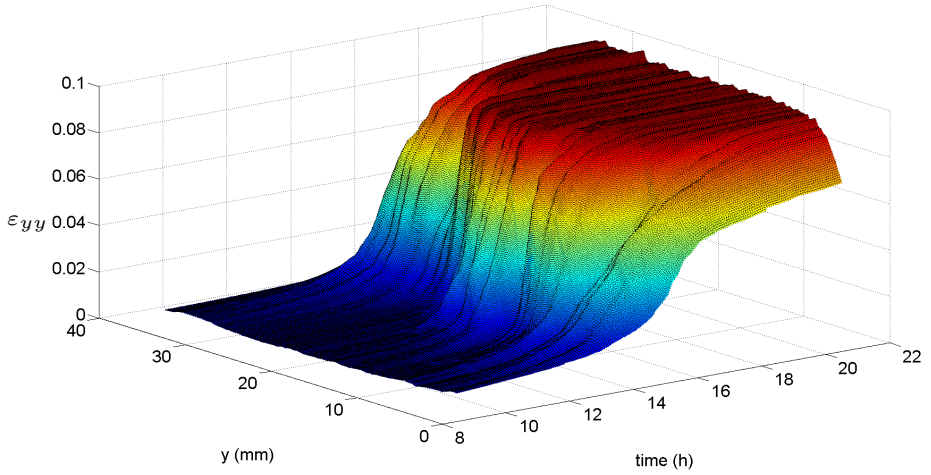

Figure 3.5: Three-dimensional plot of the vertical profiles corresponding to section $P2$ in figure 3.4 versus time.

in Section 3.1.2.

3.1.5 Loading versus unloading and beginning of the transformation

Let us focus now on the differences and analogies between the loading phase and the unloading one.
We already detailed the stress rates for loading and unloading, the durations of these two phases and of the corresponding plateaus in table 3.1 of Section 3.1.2. It is clear that from the experimental point of view the two parts of the experiment are actually akin. On the other hand, figure 3.7 shows the evolution of the strain profiles for section $P2$ (see Figure 3.4). The results are evidently asymmetric, though it is interesting to notice that the first part of the specimen that goes back to austenite is actually the last part that transformed into martensite (and viceversa).

In the same figure there is a focus on the first part of the evolution of ε_{yy}. Though the actual transformation is really fast with respect to the whole experiment, as pointed out by figure 3.5, it is interesting to notice that very small events occur already at the beginning of the experiment. The observation of the scales at which these events arise ($[0, 10^{-2}]$ versus $[0, 10^{-1}]$ for the plateau), justifies the decision to focus only on the plateau for the rest of the analysis. At the same time, it is a good evidence of the resolution that the grid method can provide.

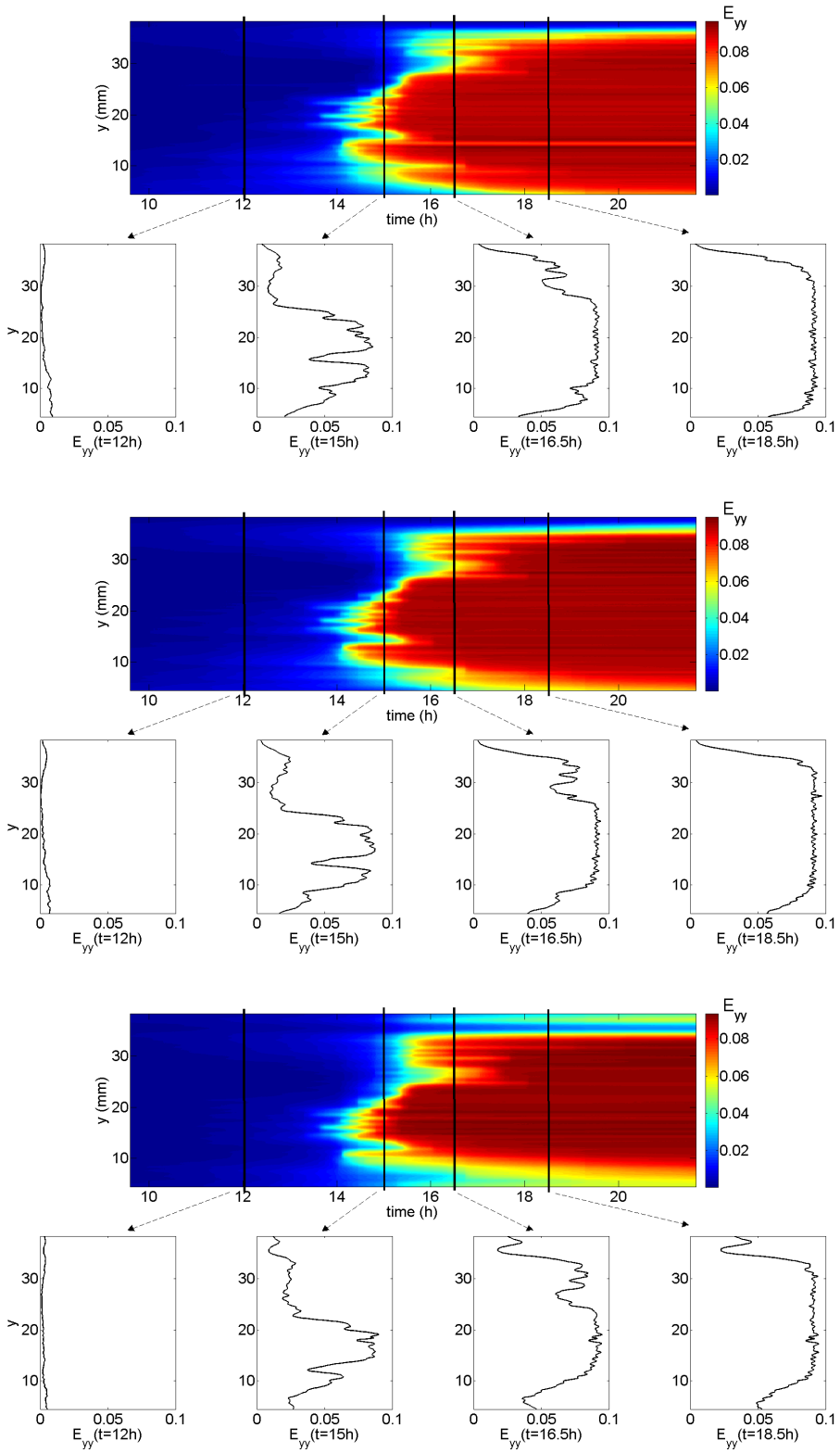

Figure 3.6: Two-dimensional view of figure 3.5 and sample strain profiles at fixed times.

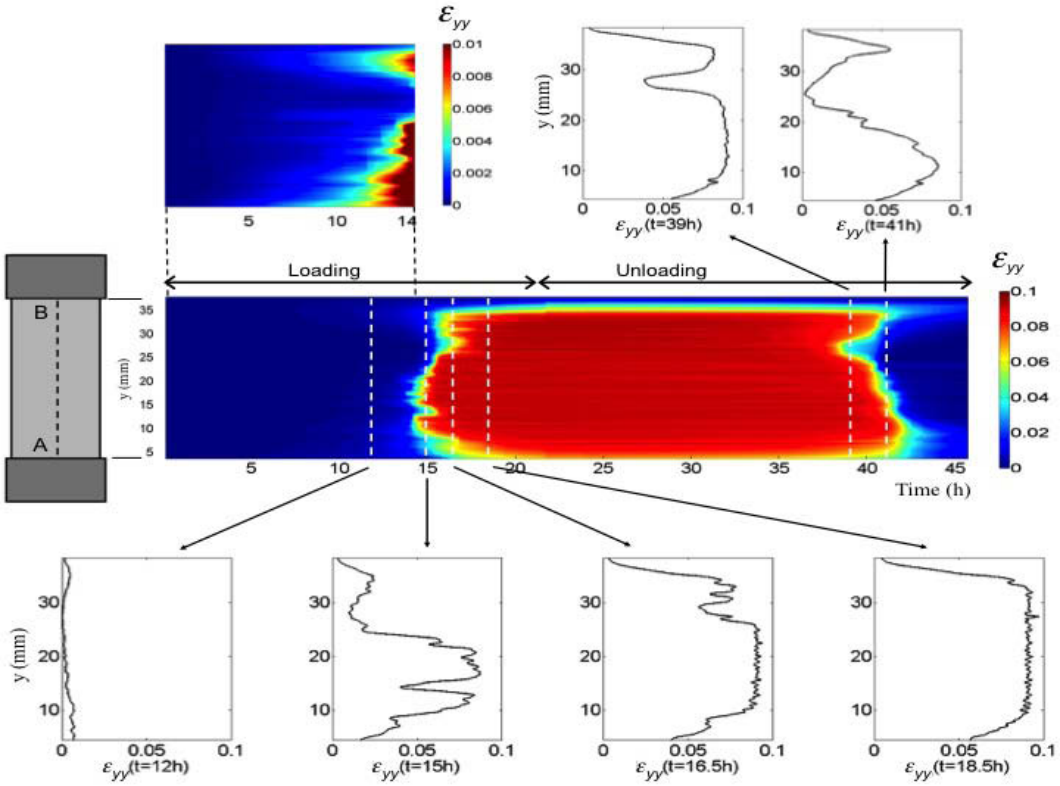

Figure 3.7: Longitudinal strain profile versus time for the total transformation, both loading and unloading phase, corresponding to section $P2$ in Figure 3.4, together with profile samples for unloading and loading. At the upper left corner there is same evolution in the time interval between the beginning and the 14th hour of experiment with a different strain scale, in order to show the first transformation events.

3.2 Characterization of the Transformation

In this section we try to deduce the kind of microstructure appearing during the transformation through the macroscopic information that are provided by our data. We start by checking whether one or more variants of martensite appear and we continue by isolating some favorite variants among the possible twelve choices for the monoclinic transformation.
Afterwards, we analyze some quantities that can be computed from our data: the number of martensite stripes and their average width, the percentage of martensite and its variation, and the variation of longitudinal vertical strain for a pixel.

3.2.1 Number of martensite variants

The first thing that we can try to determine is whether there are different variants of martensite or not. A simple way to answer this question consists in looking at the different values of strain that appear during the transformation.
Figure 3.8 shows the distribution in time of the number of pixels in ε_{xx} and ε_{yy}. At the very beginning of the plateau (map 1) all the pixels have $(\varepsilon_{xx}, \varepsilon_{yy}) = (0, 0)$ since the specimen is in the austenitic phase. The initial elastic deformation undergone by the specimen is such that the pixels are distributed in a left neighborhood of $(0, 0)$ (map 2). By proceeding with the transformation, some of the pixels start showing non-zero strains. At the end, all the pixels end around a unique non-zero value of the couple $(\varepsilon_{xx}, \varepsilon_{yy})$ (maps 7, 8 and 9). The eventual concentration of all the pixels in a point of the map indicates the presence of a single variant of martensite, since it means that all the transformed pixels have the same strain. Conversely, in case of more than one variant we would see more different attractors for the pixels in the $(\varepsilon_{xx}, \varepsilon_{yy})$ maps.

3.2.2 Selection of the martensite variant

In Section 3.2.1 we stated that in our test it is reasonable to suppose the appearance of a single variant of martensite. We thus try to identify this variant, or at least to reduce the choice among the twelve possibilities of the cubic to monoclinic transformation.
The different Bain matrices for the twelve variants of martensite are listed at the beginning of Section 2.1.1. It is straightforward to check that the compatibility condition (1.7) in Section 1.2.4 is satisfied by each variant, since it is $\lambda_1(\boldsymbol{U}_i) \leq \lambda_2(\boldsymbol{U}_i) = 1 \leq \lambda_3(\boldsymbol{U}_i)$ for $i = 1, \ldots, 12$ (we recall that $\lambda_j(\boldsymbol{U}_i)$ is the j-th ordered eigenvalue of the i-th variant of martensite). Thus, it is possible to use the result 1.2.2 to compute $\boldsymbol{a}_i^\kappa$, $\hat{\boldsymbol{n}}_i^\kappa$ and $\boldsymbol{Q}_i^\kappa$ with $\kappa = \pm 1$ characterizing the combination of austenite with each martensitic

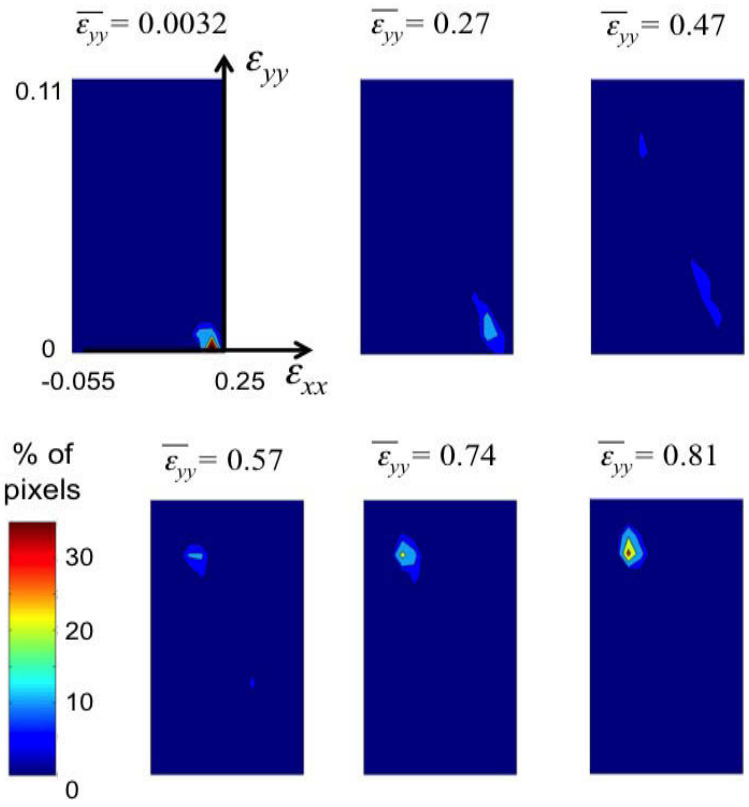

Figure 3.8: Strain clustering in the sample during the forward transformation from austenite to martensite. Snapshots for selected growing values of the average strain $\overline{\varepsilon}_{yy}$ are shown. The color bar indicates the percentage of pixels with the given strain values, with a grid pitch on the (ε_{xx}, ε_{yy}) strain plane equal to (0.005, 0.0073).

variant (we recall that there are two possible solutions for each variant). In particular, the main information is in the vector $\hat{\boldsymbol{n}}_i^\kappa$ that is related to the interface between austenite and martensite.

We can also compute a theoretical estimate of the strain components. Let us notice that, though we have two different deformation gradients $\boldsymbol{F}_i^\kappa = \boldsymbol{Q}_i^\kappa \boldsymbol{U}_i$ for each variant, there is no dependence on the rotation $\boldsymbol{Q}_i^\kappa$ when computing the strain, because of the product $\boldsymbol{F}^{\kappa T}\boldsymbol{F}^\kappa$. Actually, during our test we are dealing with linearized strains that a-priori depend on $\boldsymbol{Q}_i^\kappa$ but it can be shown that this dependence is negligible on a first order approximation. For simplicity, we thus consider a unique solution for the strain, for example by using $\boldsymbol{Q}_i = \boldsymbol{Q}_i^{+1}$ and by computing $\boldsymbol{F}_i = \boldsymbol{Q}_i \boldsymbol{U}_i$ and its linear strain $\boldsymbol{\varepsilon}_i = 1/2(\boldsymbol{F}^T + \boldsymbol{F}) - \boldsymbol{I}$.

Moreover, we can also provide some information about the interface between the austenitic zone and the martensitic one. Actually, as explained in Section 1.2.3, vector $\hat{\boldsymbol{n}}_i^\kappa$ corresponds to the normal direction to the *habit plane*, that is the undeformed plane that divides austenite and martensite.

It is important to underline that all the theoretical results we have obtained from the resolution of the twinning equation are referred to the cubic austenitic lattice vectors. In order to compare our results with the experimental ones we have to refer everything to the specimen axes. We gave in Section 2.1.1 the rotation matrix $\boldsymbol{R}$ that relates the crystal axes with the specimen ones, as

$$\boldsymbol{x}_i = \sum_j R_{ij}\boldsymbol{e}_j,$$

where $\{\boldsymbol{x}_1, \boldsymbol{x}_2, \boldsymbol{x}_3\}$ indicate the directions of the cartesian axes (x, y, z) and $\{\boldsymbol{e}_1, \boldsymbol{e}_2, \boldsymbol{e}_3\}$ are the austenite lattice vectors. Thus we can write

$$\hat{\boldsymbol{n}}^\kappa = \sum_i \hat{n}_i \boldsymbol{e}_i = \sum_{i,j} \hat{n}_i^\kappa R_{ij}^T \boldsymbol{x}_j = \sum_j \tilde{n}_j^\kappa \boldsymbol{x}_j,$$

where $\tilde{n}_j^\kappa = \sum_i R_{ji}\hat{n}_i^\kappa$, so that $\tilde{\boldsymbol{n}}^\kappa = \boldsymbol{R}\hat{\boldsymbol{n}}^\kappa$ is the normal to the habit plane referred to the specimen axes.

Analogously, we can transform the strain matrix and obtain

$$\tilde{\boldsymbol{\varepsilon}}_i = \boldsymbol{R}\boldsymbol{\varepsilon}_i\boldsymbol{R}^T.$$

Eventually, since the interface we can experimentally see is a line in the $(x.y)$ plane because we have two-dimensional maps, we have to project the habit plane. Its equation becomes

$$\tilde{n}_2^\kappa x + \tilde{n}_3^\kappa y = C.$$

This means that the angles between the horizontal axis x and the interface can be computed as

$$\theta^{\kappa} = -\arctan\left(\frac{\tilde{n}_2^{\kappa}}{\tilde{n}_3^{\kappa}}\right) + n\pi, \quad n \in \mathbb{Z}.$$

All of these theoretical information can be compared with the same experimental quantities. In Figure 3.9 we show two vertical strain maps showing the two angles formed by the interfaces between austenite and martensite. The map on the left corresponds to the loading phase while the map on the right corresponds to the unloading phase. During the loading phase we can detect only one angle since all the interfaces have the same slope, while during the unloading a second angle appears. By linearly fitting the interfaces in Figure 3.9, we obtain the experimental estimates for the two angles $\theta_{\text{exp}}^{+1} = -25$ degrees and $\theta_{\text{exp}}^{-1} = 30$ degrees more or less. Moreover, we can estimate a value for the linear strain components in the martensitic regions by averaging over a zone that is already transformed.

Table 3.2 shows the estimates for the strain components and the angle θ^{κ} for each choice of the variant, together with the experimental estimates of the same quantities. By comparing the different quantities we are able to select at least four variants that seem to be likely to appear but it is seems not possible to guess which variant is favorite among these four.

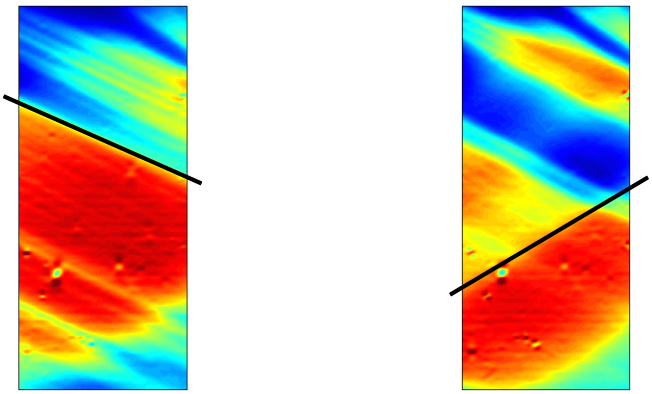

Figure 3.9: Interfaces between martensite and austenite for two fixed times, $t = 15.6$ h (left) and $t = 40.6$ h (right).

3.2.3 Number of martensite stripes

After the crystallographic guess of the previous section, it is possible to proceed with a deeper analysis of the appearance and development of martensite.

Let us focus on the central vertical section $P2$ in Figure 3.4. Figure 3.10 shows the

Table 3.2: Strain component and interface slope estimates for the twelve variants of the cubic-to-monoclinic transformation. On top, the experimental estimates for the same quantities. In bold, the four variants of martensite that appear to be closer to the experimental values.

	ε_{yy}	ε_{xx}	ε_{xy}	θ^{+1}	θ^{-1}
Experimental	0.0913	-0.0387	-0.0126	$-25°$	$30°$
Var. 1	0,003	-0,006	-0,010	$83°$	$25°$
Var. 2	0,010	-0,010	0,019	$-75°$	$-7°$
Var. 3	**0,074**	**-0,034**	**-0,027**	$\mathbf{-22°}$	$\mathbf{44°}$
Var.4	**0,082**	**-0,044**	**0,005**	$\mathbf{-38°}$	$\mathbf{28°}$
Var. 5	-0,098	0,017	0,003	$-21°$	$27°$
Var. 6	-0,099	0,060	0,002	$-37°$	$43°$
Var. 7	-0,097	0,024	0,016	$34°$	$-23°$
Var. 8	-0,099	0,068	0,006	$-37°$	$47°$
Var. 9	**0,076**	**-0,056**	**-0,005**	$\mathbf{-38°}$	$\mathbf{35°}$
Var. 10	**0,076**	**-0,047**	**-0,033**	$\mathbf{-25°}$	$\mathbf{48°}$
Var. 11	0,006	-0,015	0,009	$33°$	$-75°$
Var. 12	0,004	-0,011	-0,022	$-13°$	$83°$

evolution of the number of stripes of martensite and their average width in correspondence to this section. In order to compute this number, we firstly put a threshold on the strain value and consider as martensitic all the pixels that are above the threshold and as austenitic the under threshold ones. We chose a threshold $\tau = 0.05$, i.e. the middle value between austenite and martensite. This is the same kind of procedure that we used for the computation of the percentage of martensite in the next section, where we also detail the influence of the choice of the threshold on the results.

Once we distinguish between austenitic zones and martensitic ones, we just count how many martensite bands we find along the vertical section $P2$. We focus on the plateau, so on the time interval between the thirteenth and the eighteenth hour of experiment. At the beginning of the plateau, no stripe is counted. There is actually some microscopical phase change but it cannot be detected as an actual stripe of martensite (see section 3.1.5 referring to the beginning of the transformation).

Afterwards, the transformation proceeds through both the creation of new needles and the enlargement of previously existing martensitic stripes. From the snapshot corresponding to $t = 14.60$ h on top of Figure 3.10 we observe the presence of many small needles. The evolution of these needles proceeds by enlarging and merging while other

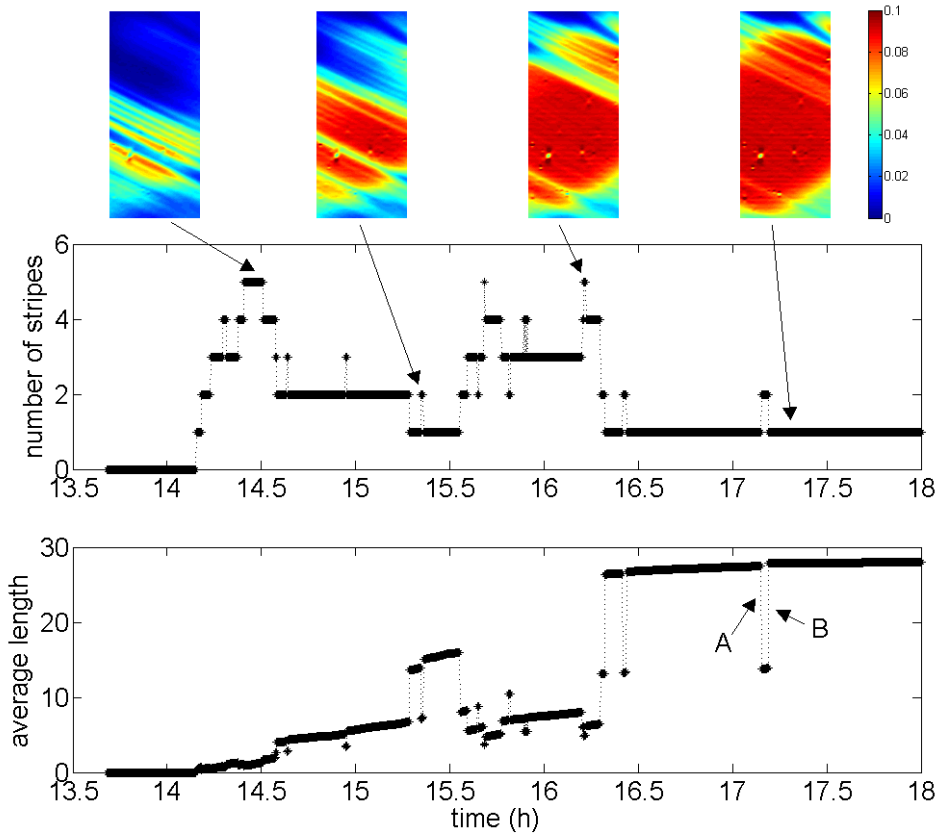

Figure 3.10: Number of stripes (top) and average width of the stripes (bottom, in pixels) versus time.

needles appear on the sides of the specimen. For $t = 15.35$ h just two big stripes are counted. Similarly, further merging and needle appearances lead to the map for $t = 16.25$ h: many stripes are counted, some of them are small needles just appeared next to a big one that keeps on enlarging. At the end of the transformation, just a unique big zone of martensite is present.

At the bottom of Figure 3.10 we show the average width of the martensitic stripes. The width of each martensite stripe is computed by using the information about the direction of the interfaces between austenite and martensite during loading (when it is practically constant and characterized by θ^{+1}). We easily compute the width of the stripe along the vertical direction, thus it is necessary to multiply by $\cos(\theta^{+1})$ to find the actual width of the stripe.

Just like the subplot that shows the number of stripes, the plot of the average width shows vertical jumps in both directions, upwards and downwards. The sudden rises correspond to the merging of two or more stripes in bigger ones, so they are related to downward jumps in the number of stripes. On the other hand, a drop in the average width can be explained by the appearance of new small needles of martensite, whose small dimension lowers the mean value. It is the case of point A and B. Immediately before point A, there is only a big stripe of martensite. Point A corresponds to the appearance of a small needle of martensite, so that the number of stripes increases while the average width decreases. The two zones merge in correspondance to point B, so that we obtain the unique big final stripe.

3.2.4 Percentage of martensite

An interesting quantity that can be easily computed is the volume fraction of martensite, denoted by ν. Like in the previous section, we fix a threshold τ and for each image we detect the number of pixels that are above this threshold. The ratio between this number and the total number of pixels provides the martensitic volume fraction for that image.

Figure 3.11 shows the behavior of the percentage of martensite during the loading phase for different choices of the threshold, from $\tau = 0.01$ to $\tau = 0.9$ (we recall the mean value in the martensitic zone is 0.0914). As expected, we have slightly different behaviors when the threshold is particularly high or low, since we are considering not enough or too much martensite, but we have a qualitatively equal behavior for thresholds $\tau \in [0.3, 0.7]$. Thus, we chose $\tau = 0.05$, which is about half of the maximum

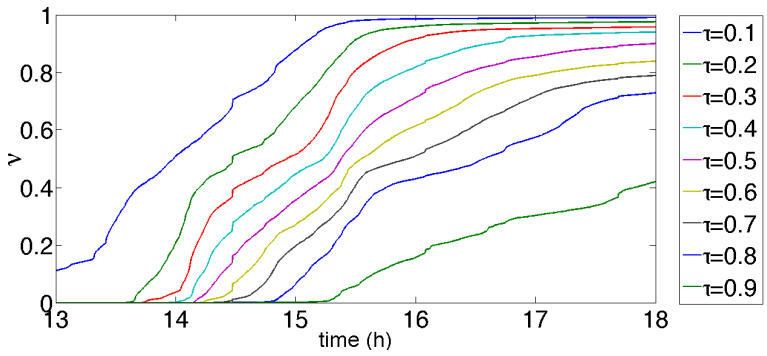

Figure 3.11: Martensite volume fraction ν versus time during loading for different values of the threshold τ.

local strain, assuming that it allows us to cut out the elastic deformations both in the austenitic phase and in martensitic one.

A further check on the choice of τ can be done by considering an estimate the error made during the computation of ν. As explained in Section 2.2.2, the grid method has a certain resolution that we have to take into account. Since the resolution for each strain map is computed to be 5.2×10^{-5} and by using the usual three-σ rule, we compute the percentage of pixels in the range $[\tau - 1.6 \times 10^{-4}, \tau + 1.6 \times 10^{-4}]$ for each image. The mean of this percentage provides a (pessimistic) estimate of the error on ν due to the strain resolution. Figure 3.12 shows the behavior of this estimate during the loading phase for different choices of τ. It is straightforward to notice that the absolute error can be consider constant for $\tau \in [0.03, 0.07]$. This plot actually proves that the percentage of points around the threshold is determined only by the strain resolution and not by elastic movements around the austenitic well or the martensitic one.
Figure 3.13 shows the behavior of ν during the plateaus of the loading and unloading phases for $\tau = 0.05$. It is particularly interesting to notice that the maximum value of ν is around 0.9 (and does not reach 1 for all the thresholds under 0.8). The fact that the martensite does not cover the total volume, as we clearly see also in Figure 3.2 and 3.3, has different causes.
On one hand, there are the reasons that are related to the features of the test. First, the presence of the grips constrains the material in such a way that it is likely inconvenient to transform all the volume. Second, the specimen has already been used for other tests. This implies that there can be defects or freezed austenite nuclei that foster the residual austenite instead of the appearance of martensite. The effect of pre-existing nuclei on

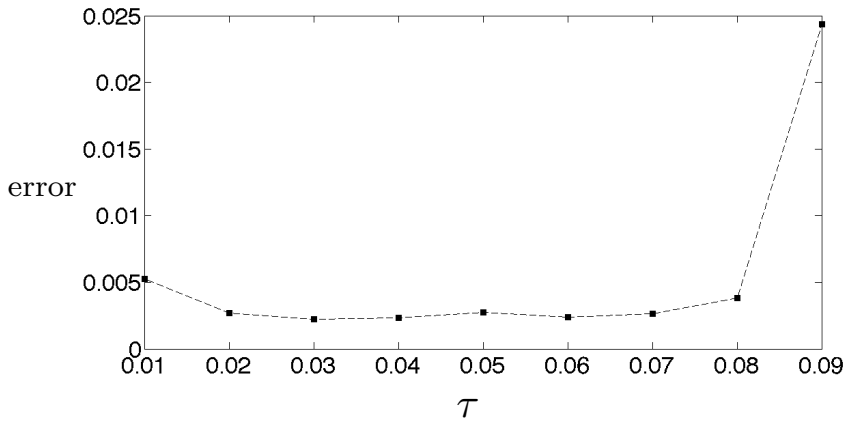

Figure 3.12: Error on the estimate of ν during loading for different values of τ.

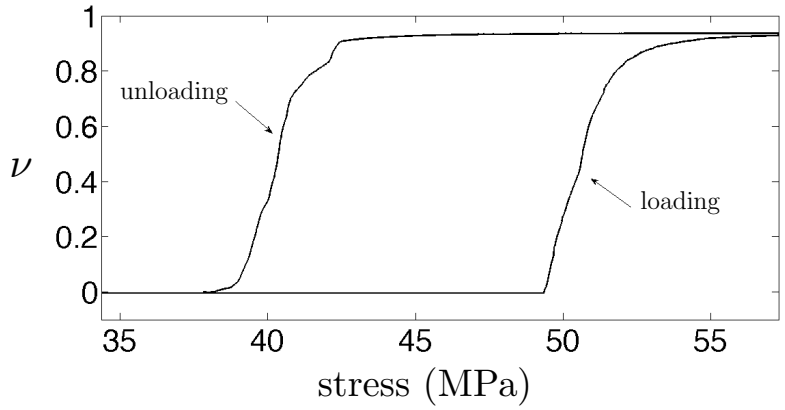

Figure 3.13: Hysteresis in the martensite volume fraction ν versus stress during loading and unloading for $\tau = 0.05$.

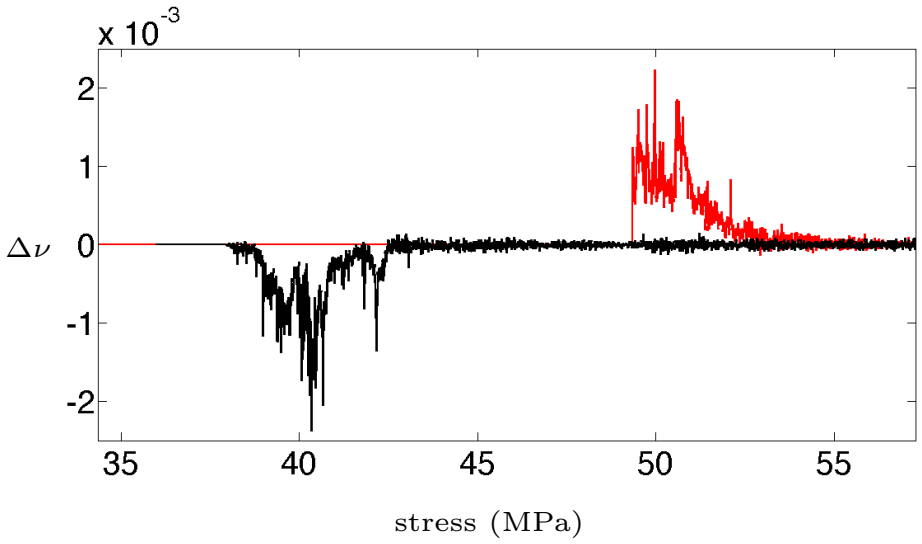

Figure 3.14: Variation of the martensitic volume fraction between consecutive images $\Delta\nu$ versus stress during loading (red), and unloading (black).

the transformation is already been studied [39] and has to be taken into account above all when dealing with cyclical transformations [95].

On the other hand, there are causes that are associated to the treatment of our data. Actually, all the strain maps are built by difference with a reference configuration and it is possible to have some zones in this reference configuration that are not completely austenitic. The presence of martensite can be due both to the residual defects or nuclei in the specimen due to previous tests and to the pre-load of 34.37 MPa applied to skip part of the elastic initial deformation, as explained in Section 2.1.2. Obviously, we selected a suitable pre-load in order to avoid this problem, but we cannot completely exclude it. The consequence of all this reasoning is that there exist zones where the strain is equal to zero but in which the specimen is in the martensitic phase. This is due to a subtraction with something that was already martensitic in the reference configuration.

The other feature that is interesting to underline in Figure 3.13 is that the overall behavior of the volume fraction seems to be continuous at the time-scale of the test. Actually, we can find a first indication of intermittent behavior in the transformation by looking at the variation $\Delta\nu$ of the martensite percentage, shown in Figure 3.14. It is important to underline that $\Delta\nu$ is not the derivative of the percentage ν but its variation between consecutive images. We immediately notice that it shows a spiky behavior despite the monotonicity of the loading and of ν. A statistical analysis of this signal is discussed in

Section 4.1.1.
Moreover, $\Delta\nu$ shows again the asymmetry between the loading phase and the unloading one as introduced in Section 3.1.5. It is possible to observe that the appearance of martensite is concentrated above all in the first part of the plateau during the loading while its nucleation rate is slower when proceeding along the plateau. Conversely, the unloading phase shows lower transformation rates at the beginning and at the end of the plateau while the main part of the martensite disappearance corresponds to the center of the plateau.

3.2.5 Longitudinal strain variation

The martensitic volume fraction ν and its variation are a global kind of information. Actually, we have further and more detailed data on the transformation since we have two-dimensional data for each instant, not only a global value for each map.
In Figure 3.15 we show the variation of the vertical longitudinal strain increment $\Delta\varepsilon_{yy}$ (computed between consecutive images) corresponding to the central section of the specimen indicated by $P2$ in Figure 3.4. In the central panel there is the overall strain variation while under it there are two panels showing the profiles of $\Delta\varepsilon_{yy}$ for two pixels $p1$ and $p2$, always corresponding to the mid-section $P2$. The biggest events in the main panel have an order of magnitude equal to 2×10^{-3} but the scale in all panels is limited to 5×10^{-4} in order to provide a better idea of the bursty evolution.
It is interesting to notice that the span of the vertical strain variation is more of less of one order of magnitude but above all the maximum variation is smaller than the value of the strain in the martensite with respect to the austenite. In theory, the crystal should transform locally from austenite to martensite so the allowed values should be just zero or the one corresponding to the martensite variant. In practice, we have to deal with the spatial resolution of the method so that the strain value for each pixel is an average of the strain of the microstructure underneath. The consequence is that we do not see abrupt jumps from zero to more or less 0.9 but a wide range of small variations.

This figure gives us an idea of the possible presence of intermittency in the transformation and of the kind of data that we have to analyze it. Indeed, the evolution shown in Figure 3.15 examines a single vertical section of the specimen while we actually have to take into account for the whole width, as we shall do in the following chapter when dealing with the statistical analysis.

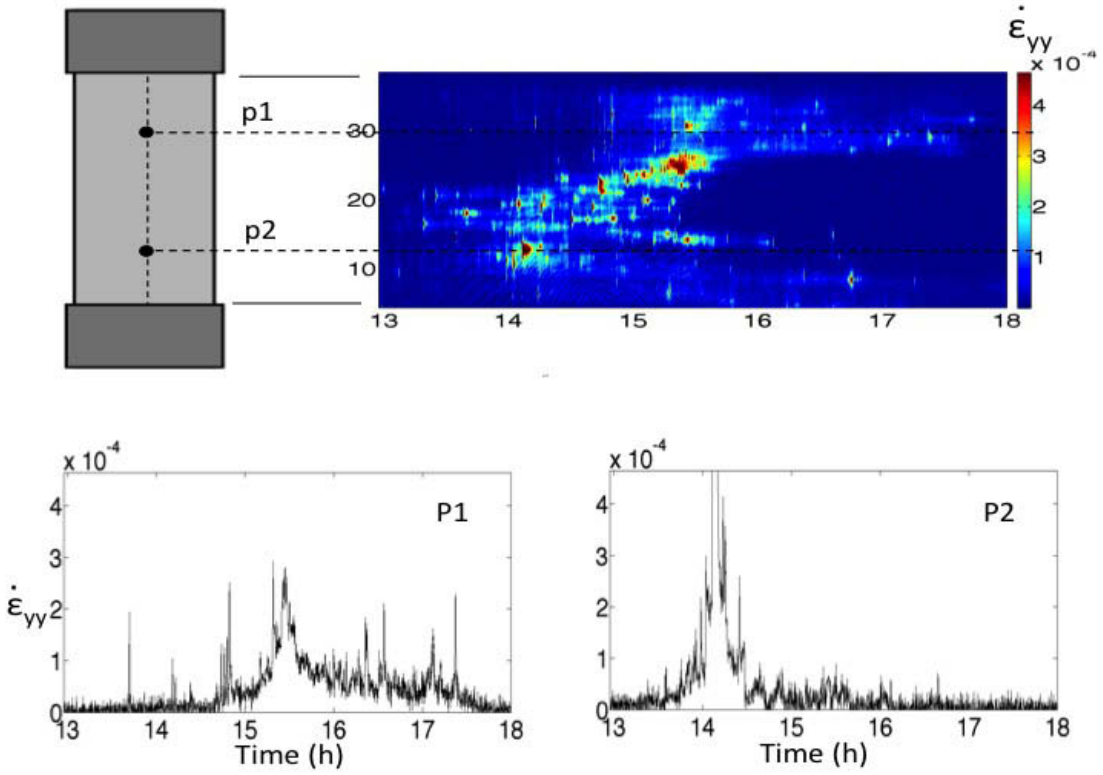

Figure 3.15: (Color online) Variation in time of the increments $\Delta\varepsilon_{yy}$ evaluated at each subsequent image at two pixels $p1$ and $p2$ in the mid-section of the sample. The time interval is [13 h; 18 h], where most of the phase transformation occurred during loading.

3.3 Conclusions

In this chapter we show some of the analysis that it is possible to perform on our strain maps. We are able to obtain some classical results for SMAs, like the stress *vs* strain curve, that allow us to compare our device with classical testing machines.
Moreover, we can deduce some information on the quantity of martensite variants appearing during our transformation and compare the experimental data with some theoretical estimates in order to select some favorite variants. In this context, it would be useful to have a microscopical mathematical model that would provide further information on the preferred variant.
The richness of our data also allows us to analyze different aspects of the martensitic transformation. We can compare the loading phase and the unloading one, we can estimate the number of martensite stripes appearing during the transformation but above all we can deduce some signals like the variation of the martensite percentage or of the vertical strain. These signals provide the first hints of the presence of intermittency in our transformation and are the starting point for the analysis in the following chapter.

CHAPTER 4

Intermittency

In this chapter we characterize the martensitic transformation in our sample from a statistical viewpoint. We first analyze some aspects of intermittency in the collected data, as in the evolution of the martensite phase fraction and of the vertical strain. We then determine the strain avalanches in our two-dimensional strain maps and analyze some of their statistical properties.

We will see that the progress of the phase change is characterized by heavy-tailed probability distributions for a number of relevant quantities, i.e. distributions whose decay is not exponentially bounded. An important example of the latter is the power-law distribution,

$$P(X) = X^{-\alpha}. \tag{4.1}$$

As such a law cannot hold for all X, a typical power-law behavior in the data is characterized by the exponent α but also by the logarithmic width of the interval in which it describes the phenomenon of interest (that is the number of orders of magnitude for which equation (4.1) describes reasonably well the data collected for the variable X). Among the heavy tailed distributions, power laws are especially remarkable because a change of scale in X just implies a multiplication by a factor while the exponent re-

mains the same. Furthermore, power law behavior is thus often associated to the proximity of the given system to a critical point.
We follow the usual practice and plot heavy-tailed distributions in a logarithmic scale on both axes, so that power laws are described by straight log-log plots whose slope corresponds to the exponent α.
Martensitic transformations exhibit a classical hysteresis loop such as the one in Figure 3.2. However, they have also been found to display intermittency and self-similarity in their acoustic emission [16, 24, 43, 66–68, 100–102]. Previous attempts to deduce some spatial information on the progress of the martensitic transformation has also been based on acoustic emission techniques, for example by coupling more than one sensor [102]. Other techniques, such as optical observations [49,68] or calorimetry [16], have also given partial information on the spatial distribution of the intermittency. The present experiment not only confirms the macroscopic results for the hysteretic stress-strain relation in SMAs, but also highlights how the transition progresses through intermittent strain events under the monotonic stress-driven loading, which we analyze quantitatively here for the first time.

4.0.1 Intermittency and the energy landscape

The presence of intermittency is strictly linked to the shape of the energy landscape. Shape Memory Alloys are characterized by a non-convex energy, so that the free energy density functions built in the mathematical models are non-convex in the strain variables and the analytical tools usually used derive from non-convex analysis ([14, 61, 62]). Models that take into account the interesting energetic landscape for shape-memory alloys have already been built, like phase-field models [25, 34, 103, 105] or automaton models [40, 76, 78]. As suggested in the conclusions, this is the kind of model that could reproduce intermittency in the process, exactly because it recreates the complex energy landscape.
For simplicity, let us suppose to be at the transition temperature for which austenite and martensite are energetically equivalent. Locally, the energy is as sketched in the middle of Figure 1.4 in Section 1.2.2: it is a non-convex energy with a number of minima equal to $N + 1$, where N is the number of martensite variants. On the global level, it is necessary to introduce the idea of *Ericksen-Pitteri neighbors* [29, 75]. Shortly, an Ericksen-Pitteri neighbor includes lattices that are identical to the original lattice but that have been obtained through a certain number of slips. As explained in Section 1.2 with Figure 1.3, a slip in the lattice, and thus the jump to an Ericksen-Pitteri neighbor,

implies the appearance of dislocations in the finite crystal. The final result is that the energy landscape is composed by an infinite number of wells, obtained by periodically repeating the local structure with $N + 1$ minima. This kind of description keeps on holding when the temperature is higher or lower than the transition temperature, since it is only the number of minima in the local structure that changes.
Thus, the main features for the SMA energy are non-convexity and the presence of many metastable minima (see Section 1.2.1 for the definition of metastability), that are separated by different energy barriers. Moreover, the whole energetic landscape can be easily modified by varying the external load or the temperature: this kind of changes can affect the number of minima, the stability of the configurations and the height of the barriers between the minima. The consequence of this kind of structure is that the evolution of the system can be non-continuous: the system remains pinned in a minimum until there is enough energy to jump to another energy well (from austenite to martensite or viceversa or among different Ericksen-Pitteri neighbors). By consequence, an intermittent behavior can arise since a single point of the system stays still in a well, while it stores the energy to overcome the barriers between the minima or until the energy landscape is modified by a change in load or temperature, and then suddenly jumps. The jump of one point can cause the jumps of other points of the system towards other minima, thus producing a so-called avalanche.

4.1 Some Intermittent Behaviors in the Experimental Results

In this section we analyze the probability distribution function of the martensite variation and of the vertical strain variation that we introduced in Sections 3.2.4 and 3.2.5.

4.1.1 Variation of the percentage of martensite

We have already seen in Section 3.2.4 that the percentage of martensite is a good example of quantity that seems to be quite smooth and continuous when macroscopically observed but shows a spiky behavior in its variation. Thus, it can be interesting to study the variation $\Delta\nu$ from a statistical point of view.
Figure 4.1 shows the empirical probability distribution function of the absolute value of the martensite variation, $|\Delta\nu|$, in a logarithmic scale: on the horizontal axis there is a logarithmic binning of the martensite variation values while on the vertical axis there is the frequency of each of these bins.

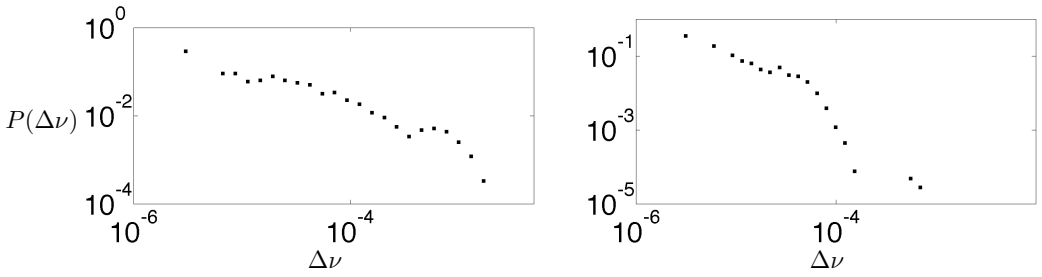

Figure 4.1: Log-log plots of the pdf of the absolute value of the martensite variation during loading (left) and unloading (right).

Both plots show how the martensite variation $|\Delta\nu|$ spans over a range of about two decades, giving heavy-tailed distributions which are not power laws.

The same kind of analysis can be done on a quantity that is basically the same as the martensite percentage, that is the average vertical strain $\overline{\varepsilon}_{yy}$. Its behavior in time is already shown in the stress-strain curve in Figure 3.2, since stress and time are proportional, while its variation is plotted in Figure 4.2. The spiky behavior suggests the presence of intermittency that is translated in a heavy-tailed distribution, shown in Figure 4.3, that is anyway far from being a power-law.
Moreover, both the variation of the martensite percentage $\Delta\nu$ and of the average vertical strain $\Delta\overline{\varepsilon}_{yy}$ are clearly different in different parts of the transformation. This behavior is a hint of the non-stationarity of the process, that we will analyze in Section 4.3.4.

4.1.2 Variation of the longitudinal strain

As for the martensite percentage, the average strain $\overline{\varepsilon}_{yy}$ merges many events into a global information, so that it is not suitable for a good statistical analysis.
On the other hand, another quantity that we showed in the previous chapter, in Section 3.2.4, is the variation of the vertical strain, $\Delta\varepsilon_{yy}$.
We previously showed the behavior in time of $\Delta\varepsilon_{yy}$ for only two pixels, but we obviously have this information for many more pixels (around 3×10^5 pixels for each image). By focusing only on the plateaus, that is more than 4000 images between loading and unloading, we thus have a good amount of points to consider for some statistics. Actually, of all these values of $\Delta\varepsilon_{yy}$ we select the ones above a threshold equal to 4×10^{-4} in order to cut out the experimental noise. The necessity of a threshold and the choice of its value is better detailed later in Section 4.2.2.

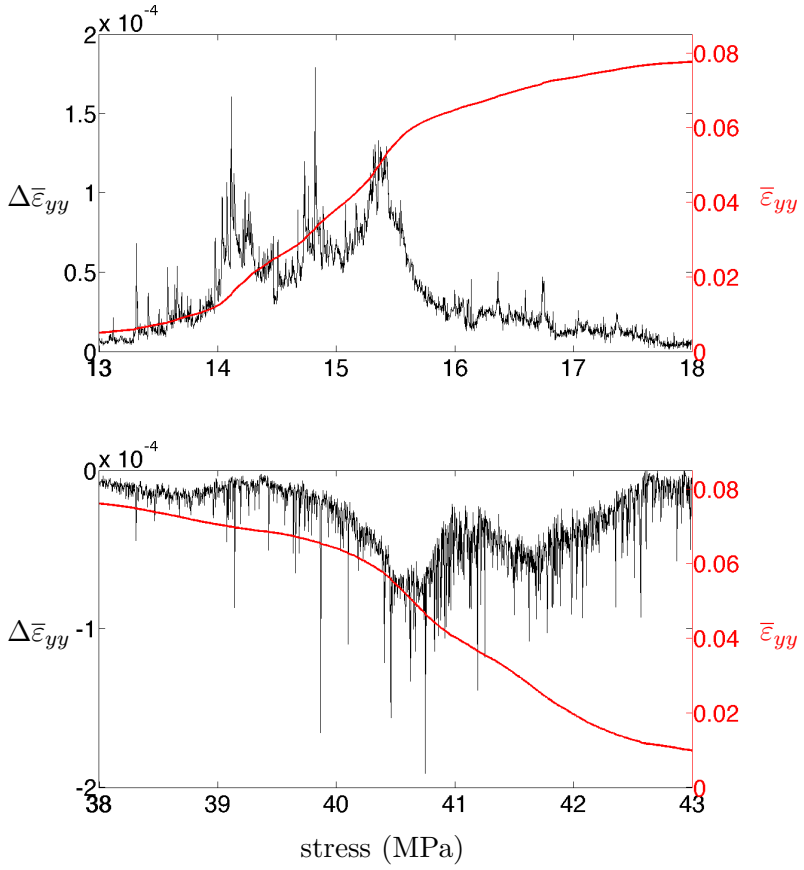

Figure 4.2: Evolution of the average vertical strain variation between consecutive images $\Delta\overline{\varepsilon}_{yy}$ during loading (left), and unloading (right).

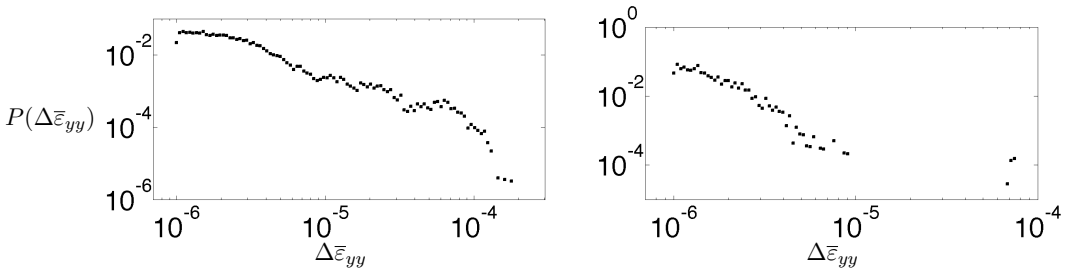

Figure 4.3: Log-log plots of the probability distribution function of the average vertical strain variation $\Delta\overline{\varepsilon}_{yy}$ during loading (left) and unloading (right).

Figure 4.4 shows the logarithmic plot of the probability distribution function of $\Delta\varepsilon_{yy}$ for all the pixels in which it is bigger than the threshold and along both the loading and unloading plateaus.

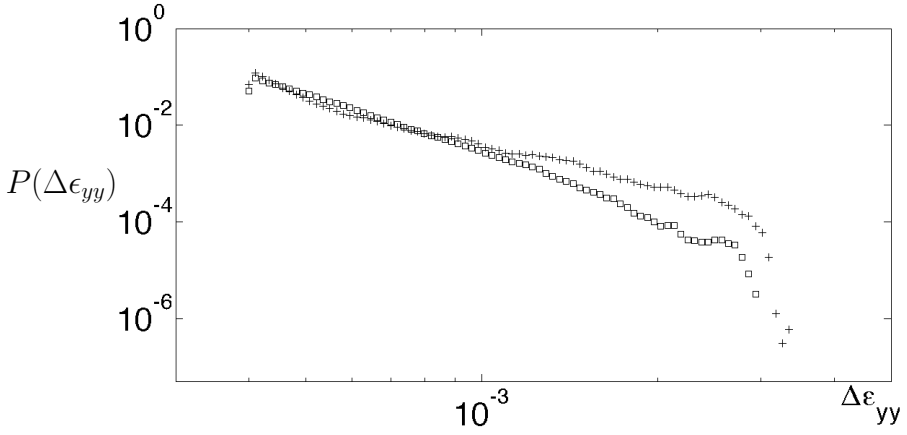

Figure 4.4: Log-log plot of the probability distribution function of the vertical strain variation $\Delta\varepsilon_{yy}$ during loading (squares) and the unloading (crosses).

We see that the values of the vertical strain variations $\Delta\varepsilon_{yy}$ span about an order of magnitude both on loading and unloading, with the biggest events below the usual deformation value of the martensite, as explained in Section 3.2.5. The corresponding probability distributions are heavy-tailed, but we are looking at a measure of the strain events that is in a sense too localized, as here we are considering the strain variation at the level of single pixels with no interaction among them. We conjecture this is the reason for the severe cutoff that we observe in these strain data. A better analysis of the strain events must properly take into account the full extent of such events, i.e. of the strain avalanches that mark the progress of the transformation. From the analyzed behavior of $\Delta\varepsilon_{yy}$ and $\Delta\overline{\varepsilon}_{yy}$ we expect such avalanches to span several orders of magnitude in size, with, possibly, a distribution which is rather close to a power law, as indicated by the acoustic emission data.

4.2 Avalanche Detection

In this section we define the *strain avalanches* and describe how we detect them in our data.

4.2.1 Detection algorithm

In order to take into account all the strain components, we consider the norm of the strain variation between consecutive images, that is

$$||\Delta\varepsilon|| = \sqrt{\Delta\varepsilon_{yy}^2 + \Delta\varepsilon_{xx}^2 + 2\,\Delta\varepsilon_{xy}^2}.$$

This gives a scalar value for each pixel and time, for which we consider a threshold η that cuts out the noise, whose choice is detailed below in Section 4.2.2. For each fixed time, we then define an *avalanche* as a connected set of pixels whose value $||\Delta\varepsilon||$ is above threshold.
The detection of each avalanche thus requires the following steps:

1. we select the point P in the map where $||\Delta\varepsilon||$ is maximum;
2. if $||\Delta\varepsilon(P)|| < \eta$, we stop. Otherwise
   - we create a list of the pixels that are involved in this avalanche and we put P in it, while setting $||\Delta\varepsilon(P)|| = 0$ to avoid multiple counting of the same pixel;
   - we check each neighbor of each point on the list and if its $||\Delta\varepsilon||$ is bigger than η we put it in the list and we nullify its $||\Delta\varepsilon||$;
   - we continue this check until there are no points in the list (all the points involved in the avalanche have been recorded, without double counting);
3. we return to number 1.

As the time scale of our image collection (8.6 seconds) is much larger than the known time of avalanche evolution in SMAs, we do not consider the possible evolution in time of the strain avalanches detected as described above.

Figure 4.5 provides a visual evidence of the intermittent behavior of the transformation, with avalanches of different sizes. On the left there are two maps of $||\Delta\varepsilon||$ corresponding to two different times (quite close, 14 hours and 49 minutes on top and 14 hours and 51 minutes below): they are blurred because of the noise and it is not easy to distinguish the avalanches, though it is possible to notice that the events have different intensities. On the right we put the threshold η on the $||\Delta\varepsilon||$ maps: the blue pixels are the ones with $||\Delta\varepsilon|| < \eta$ while for the red ones we have $||\Delta\varepsilon|| > \eta$. Such noise thresholding highlights the strain events in a much clearer and sharper way.

4.2.2 Choice of the threshold

In Section 2.2.2 we provided an estimate for the experimental noise in our data, with a final value for the noise standard deviation $\sigma = 5.2 \cdot 10^{-5}$.

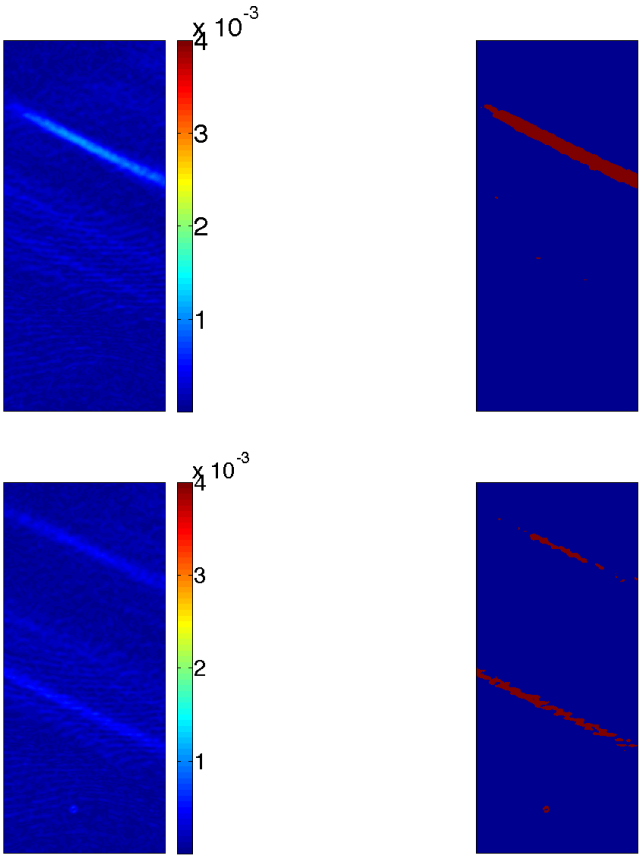

Figure 4.5: Examples of maps of the strain variation norm (left) and the same maps after putting a threshold $\eta = 4 \times 10^{-4}$ (right).

In order to correctly cut out the noise, we have to pay attention to the quantity that we are considering. First of all, σ is simply the standard deviation, so it has to be multiplied by three if we want to be quite confident in avoiding the noise (by using the usual three-σ rule). Thus, the value 3σ would be the minimum noise threshold to choose when dealing with only a component of the strain.
In our case, the use of $||\Delta\varepsilon||$ implies firstly a difference between two maps and then a function of three different components. Thus, it is necessary to make the following considerations for an estimate of the noise for the norm of the strain variation.

- *Noise in the strain variation maps*. Usually, when making the difference between quantities q_1 and q_2 with errors e_1 and e_2, the result is affected by a bigger error obtained as the sum $e_1 + e_2$. This relation holds when q_1 and q_2 are independent between each other, that is not true in our case. Indeed, each strain map is already obtained through a difference with respect to the same reference configuration, according to equation (2.2). The noise standard deviation σ that we compute for each map thus includes the noise of the reference configuration and the own error of the current strain. When we make the difference between the maps at two consecutive times, let us say t and $t + 1$, the part of the noise corresponding to the reference configuration is compensated. Thus, we can assume to estimate the noise for the strain variation simply with the noise of the strain map, without any amplification.

- *Noise of the different components*. We can assume ε_{xx} and ε_{yy} to have the same noise, since obtained in the same way, while there is some change when dealing with the shear component ε_{xy}. The reason of this difference comes from the definition of $\varepsilon_{xy} = 1/2(u_{x,y} + u_{y,x})$, where $u_{x,y}$ and $u_{y,x}$ are the mixed partial derivatives of the displacement.
  Actually, the computation of the camera sensor noise propagation through Equation (2.4) provides an estimate that is sensibly the same for the four derivatives $u_{x,x}, u_{y,y}, u_{x,y}$ and $u_{y,x}$. Since we are adding two of these derivatives, the variance of the sum is equal to the sum of the single variances. By consequence, the standard deviation of $(u_{x,y} + u_{y,x})$, that is the square root of the variance, is computed as $\sqrt{2}\sigma$. Finally, the definition of the shear strain component requires a division by 2, so that the standard deviation for ε_{xy} is equal to $\sigma_{xy} = 1/2\sqrt{2}\sigma = \sigma/\sqrt{2}$.

- *Noise of the square variation*. In order to estimate the standard deviation for the square variation of the strain, we use the following result, known as *delta method*. In general, given a quantity X with standard deviation σ_X and another quantity

$Z = f(X)$, it is possible to compute the standard deviation of Z as

$$\sigma_Z = f'(\overline{X})\sigma_X,$$

where $\overline{X}$ is the mean of X. In our case we would have for example $Z = (\Delta\varepsilon_{yy})^2$ and $X = \Delta\varepsilon_{yy}$, so that the standard deviation for the square variation is $\sigma_{yy^2} = 2\overline{\Delta\varepsilon_{yy}}\sigma$.

This estimate depends both on time, since we a-priori have a different $\overline{\Delta\varepsilon_{yy}}$ for each image, and on which component of the strain we are considering.

Since we are already working with approximations and estimates, we can solve the problem of the dependance on time by considering only the mean order of magnitude of $\overline{\Delta\varepsilon_{yy}}$, neglecting particular values that would not have a real importance in this context. In this way, we have $\sigma_{yy^2} = \sigma_{xx^2} = 2 \times 10^{-4}\sigma$ and $\sigma_{xy^2} = \sqrt{2} \times 10^{-5}\sigma$.

- *Noise of the norm*. Eventually, we sum the three square variations, so that we have to sum the single standard deviations that we have just computed. We thus obtain $\sigma_{\text{sum}} \simeq 4 \times 10^{-4}$.

  At this point, we should apply the just described delta method in order to consider the square root of the sum. This time it is $Z = f(X) = \sqrt{X}$, thus providing

  $$\sigma_f = \frac{1}{2\sqrt{\overline{X}}}\sigma_{\text{sum}}.$$

  Also in this case we have to compute the mean of $(\Delta\varepsilon_{yy})^2 + (\Delta\varepsilon_{xx})^2 + 2(\Delta\varepsilon_{xy}^2)$. Since it is going to be different for each image as well, we compute its order of magnitude, that is 10^{-8}. By doing so, we eventually obtain an estimate of the standard deviation of the noise on the norm as $\sigma_f = 2\sigma \simeq 10^{-4}$.

Finally, by applying the usual three-σ rule, we obtain a lower bound for our noise threshold $\eta_{\text{min}} = 3\sigma_f = 3 \times 10^{-4}$.

All the steps we described actually imply approximations, so that the value we obtained for σ_f has to be checked by looking at our experimental data. Figure 4.6 shows the map of the strain variation norm and the corresponding maps with two different values of the threshold η. It is straightforward to notice that for a η slightly lower than η_{min} we obtain more events but the image is blurred, so that we are not able to distinguish real events from experimental error. On the contrary, for a threshold just above η_{min} we lose part of the information on the event but the noise disappears.

After these considerations, we eventually chose a threshold $\eta = 4 \times 10^{-4}$, so that we are above η_{min} in order to cut out the noise but we are close enough to the limit in order to catch the most of the information we have on events.

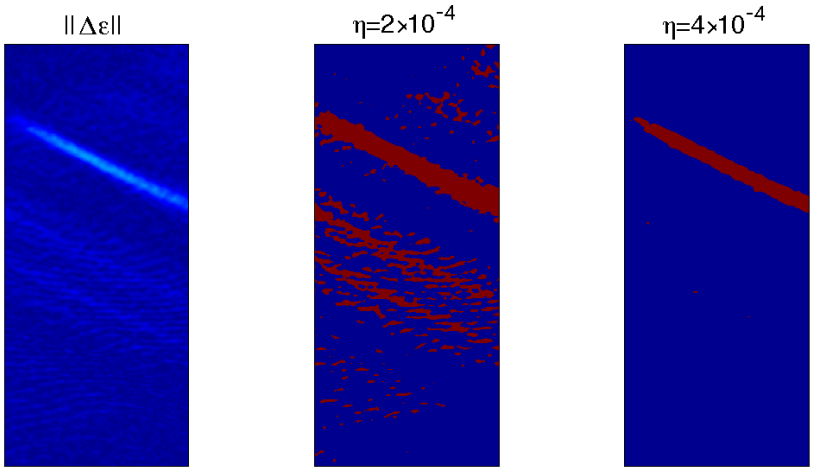

Figure 4.6: Comparison of the effect of different choices of the threshold η on the noise. The first image is the map of the strain variation norm $||\Delta\varepsilon||$ around $t = 14.8$ h. The second and third map correspond to $\eta = 2 \times 10^{-4}$ and $\eta = 4 \times 10^{-4}$, respectively.

4.2.3 Magnitude, size and epicenter

At this point we have recorded which point belongs to which avalanche so that we can deduce some information on the events. Thus, we define some characteristic quantities.

First of all, we can introduce the *size* $\mathcal{S}$, that is the number of pixels involved in each avalanche V, to be computed as

$$\mathcal{S} = \sum_{(i,j)\in V} 1.$$

Furthermore, we can define a *magnitude* $\mathcal{M}$ of V, by considering

$$\mathcal{M} = \sum_{(i,j)\in V} ||\Delta\varepsilon_{(i,j)}||.$$

Finally, we can try to keep some spatial information by detecting the *epicenter* of an avalanche V, defined as

$$(e_x, e_y) \quad s.t. \quad ||\Delta\varepsilon_{(e_x,e_y)}|| = \max_{(i,j)\in V} ||\Delta\varepsilon_{(i,j)}||,$$

that is the point of maximum for each event.

Before proceeding with a statical characterization of these avalanches, let us simply look at the patterns of the signals we obtained.

Figure 4.7 shows the number of avalanches for each image during the transformation

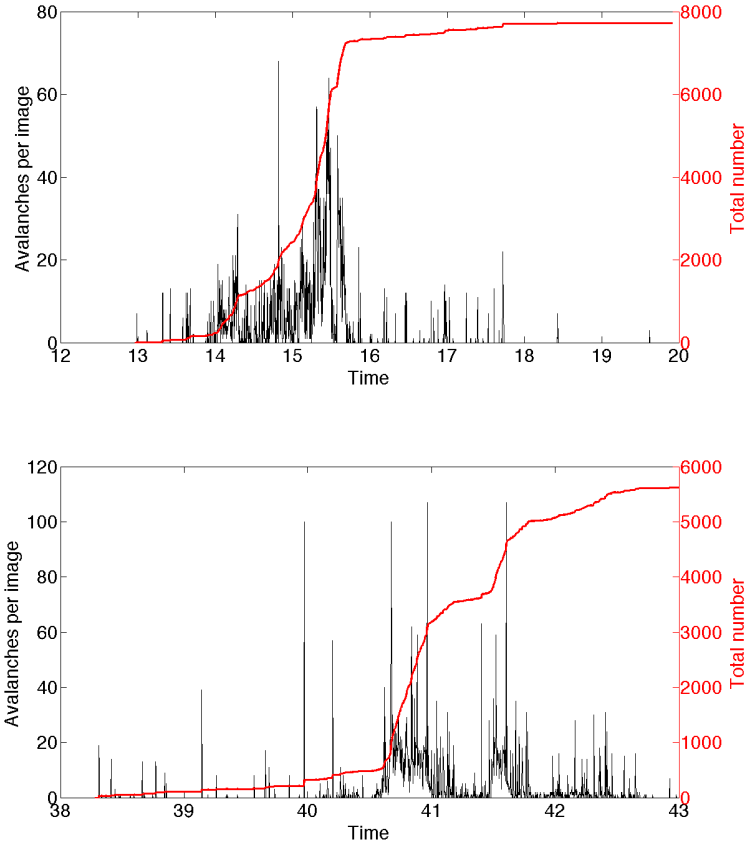

Figure 4.7: Number of avalanches for each image (black) and total number of avalanches versus time (red) for loading, on the left, and unloading, on the right.

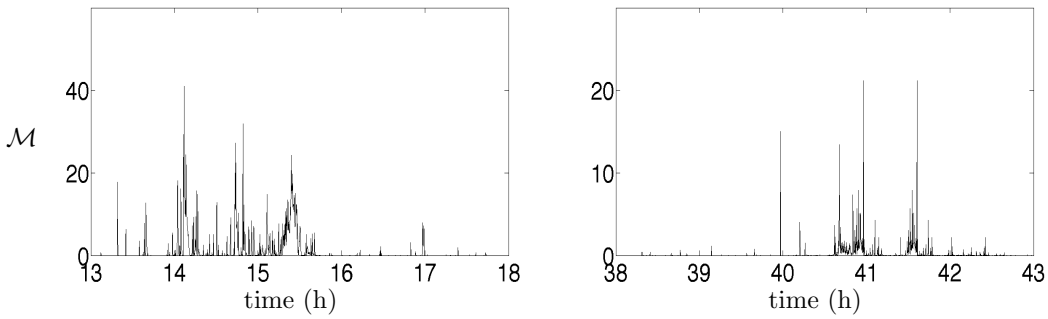

Figure 4.8: Magnitude $\mathcal{M}$ versus time during loading (left) and unloading (right).

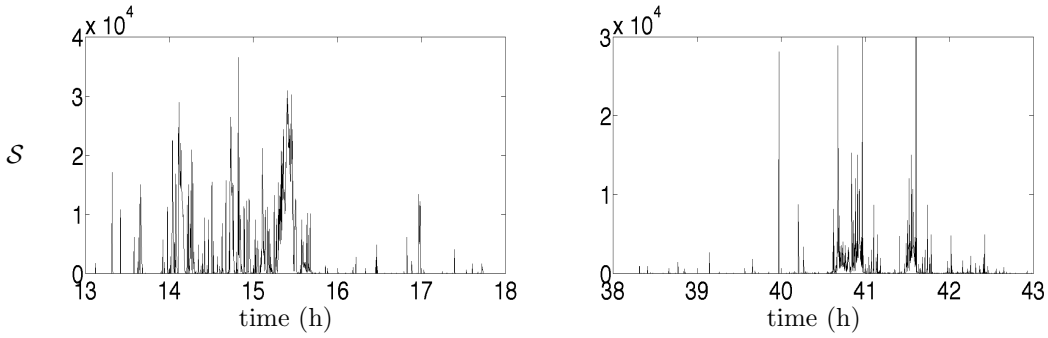

Figure 4.9: Size $\mathcal{S}$ versus time during loading (left) and unloading (right).

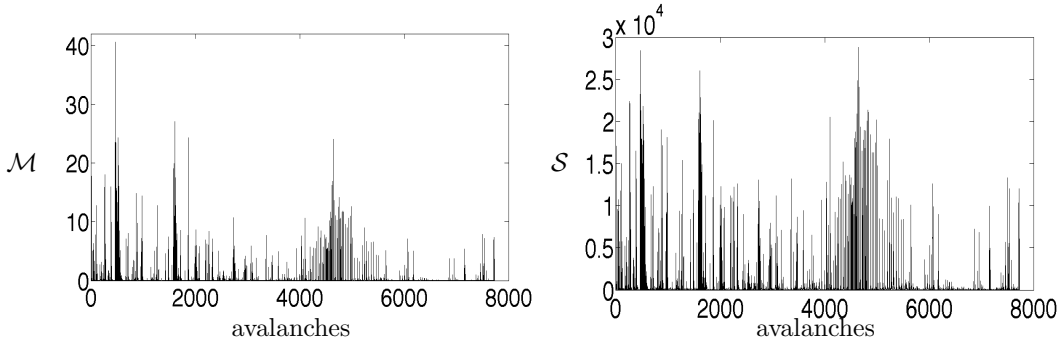

Figure 4.10: Magnitude $\mathcal{M}$ (left) and size $\mathcal{S}$ (right) for each avalanche V during the loading phase.

Figure 4.11: Epicenters of the avalanches during loading (left) and unloading (right).

(black) and its cumulative sum, that is the total number of avalanches in time. We find around 7700 avalanches during the loading phase and 5900 for the unloading phase, for a total amount around 13600. We immediately notice the jerky behavior of the signal as already found for the other quantities, like ν, $\Delta\overline{\varepsilon}_{yy}$ and $\Delta\varepsilon_{yy}$. Exactly like for those quantities, we have another hint of the non-stationarity with which we shall deal in Section 4.3.4.
Figure 4.8 shows the magnitude of the avalanches of each figure for both loading and unloading, while Figure 4.9 shows the behavior of the avalanche size in time. These are the kinds of signals that can be obtained by using acoustic emission or by measuring the total latent heat, since we consider a unique information for each image. Actually, we have the underlying information on the single different avalanches. The signals we statistically analyze are thus represented in Figure 4.10 (only for loading), in which we do not consider the temporal information.
We also have some spatial information. For example, Figure 4.11 shows the position in the specimen of all the epicenters for loading (left) and unloading (right). We find again the characteristic slopes on which we focused in Section 3.2.2 for the selection of the martensite variant. This result is quite reassuring on the good detection of the avalanches, since it is related to the martensite needles proceeding across the specimen along their favorite direction. Moreover, there are no epicenters in the upper part of the specimen where no martensite appears during all the test.

4.3 Statistical Characterization of the Avalanche

In this section we try to characterize the behavior of our system from a statistical point of view. First of all, we analyze the relationship between size and magnitude of avalanches. After that, we provide an estimate of the exponent through the Maximum Likelihood method. Eventually, we analyze the non-stationarity of our signals.

4.3.1 Conditional distribution of magnitude and size

In one-dimensional measurements we usually do not have the information regarding both the size of an avalanche and its magnitude, or its energy. Thus, in our case it becomes interesting to look at the relation between $\mathcal{M}$ and $\mathcal{S}$. Figure 4.12 shows the ratio between magnitude and size, $\mathcal{M}/\mathcal{S}$, of an avalanche and the logarithm of its size. This figure leads to two observations.
First, the points are all distributed above a straight line with positive slope in the semi-

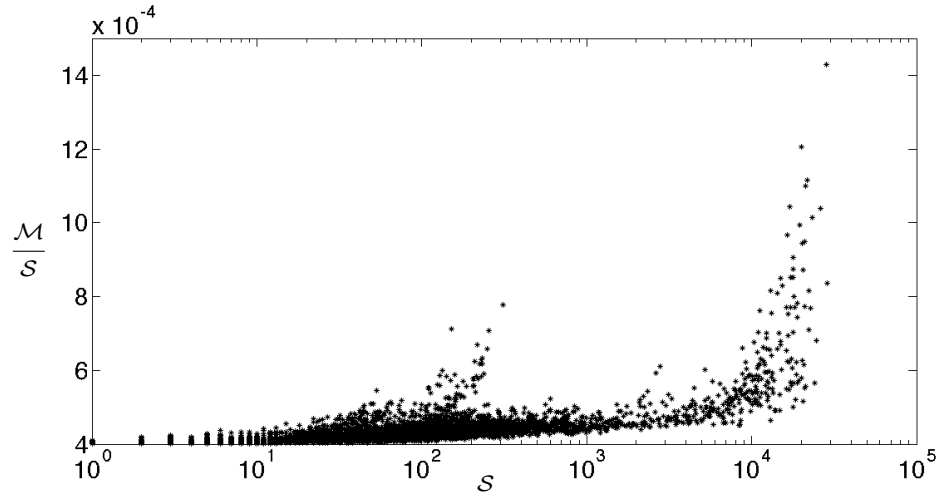

Figure 4.12: Semi-log plot of the ratio $\mathcal{M}/\mathcal{S}$ of each avalanche V versus the size $\mathcal{S}$ (logarithmic scale on the horizontal axis), during the loading phase.

log plot. This means that we have a relation of the following type

$$\frac{\mathcal{M}}{\mathcal{S}} \propto \rho \log \mathcal{S} \quad \Rightarrow \quad \frac{\mathcal{M}}{\mathcal{S}} \propto \log \mathcal{S}^{\rho}, \ \rho > 1.$$

By consequence the only think that we can say is that $\mathcal{M}\mathcal{S}^{\rho+1}$ with $\rho > 0$, but we do not have the possibility to deduce some further information.
Second, the points are vertically spread for certain values of the size. This is due to the different contribution that each pixel in the avalanche can give to $\mathcal{M}$ or $\mathcal{S}$. The contribution to the size is always equal to 1. Conversely, as regards the magnitude, each pixel can have a different $||\Delta\varepsilon||$ that can vary within an order of magnitude (as it is possible to notice from Figure 4.4 for the $\Delta\varepsilon_{yy}$, which is the main strain component in our case). This implies that the contribution of each pixel to $\mathcal{M}$ is in a range whose width is around one decade. By consequence, $\mathcal{M}$ and $\mathcal{S}$ can basically be considered almost equivalent in our case but they can be substantially different in cases in which $||\Delta\varepsilon||$ has the possibility to vary in wider intervals.

4.3.2 Estimate of the exponent

The quantity that characterizes a power law is obviously the exponent α in the probability density function introduced in Section **??**.
The estimate of this exponent is not so straightforward when dealing with empirical data, so that we followed the method used in [15, 24, 43, 66, 67] and introduced by Clauset in [27].

In general, we analyze a signal that we suppose to be distributed according to

$$p(x)dx = Cx^{-\alpha}dx,$$

where C is a normalization constant. Since this law diverges for $x \to 0$, we introduce a lower bound x_{min} to the power-law. By consequence, we also obtain the expression of the normalizing constant

$$C = \frac{\alpha - 1}{x_{\text{min}}^{1-\alpha}}.$$

In [27] Clauset provides an expression for the estimate of the exponent α through the method of maximum likelihood, as follows

$$\hat{\alpha} = 1 + n \left[\sum_{i=1}^{n} \ln \left(\frac{x_i}{x_{\text{min}}} \right) \right]^{-1},$$

where the hat indicates that it is an estimate and $x_i,\ i = 1, \ldots, n$ are the values of x bigger than the lower bound x_{min}. Moreover, there is also an expression for the standard error on this estimate

$$\sigma_\alpha = \frac{\hat{\alpha} - 1}{\sqrt{n}}.$$

Since we do not have the information about x_{min} in our data, the kind of analysis that is usually performed consists in choosing a set of values for x_{min} throughout all x and estimate the exponent for all the values $x \geq x_{\text{min}}$. By plotting the behavior of $\hat{\alpha}$ versus x_{min} we should find a range of stability for the estimate $\hat{\alpha}$.

4.3.3 Probability distribution of magnitude and size

We can now look at the statistical behavior of the quantities plotted in Figure 4.10, that is the magnitude and the size of the different avalanches.
Figure 4.13 shows the log-log plot of the probability distribution function of the magnitude $\mathcal{M}$ during the transformation (both loading and unloading). We obtain a heavy-tailed distribution spanning more or less four decades. According to what explained in Section 4.3.2, let us suppose to have a law of the kind $p(\mathcal{M}) = \mathcal{M}^{-\mu}$ for the magnitude and let us compute the estimates $\hat{\mu}$ for different values of $\mathcal{M}_{\text{min}}$, that we show in Figure 4.14. Small values of $\mathcal{M}_{\text{min}}$ usually consider also some noise in the distribution, so that the exponent is slightly smaller than the real one, while for big values of $\mathcal{M}_{\text{min}}$ the statistic is based on a number of points too small to be reliable. In a certain range of more than two decades for $\mathcal{M}_{\text{min}}$,there is a quite constant value of μ that ranges between 1.5 and 1.8. This kind of behavior is not enough to claim the presence of a power-law distribution but indicates a certain stability of behavior for many scales.

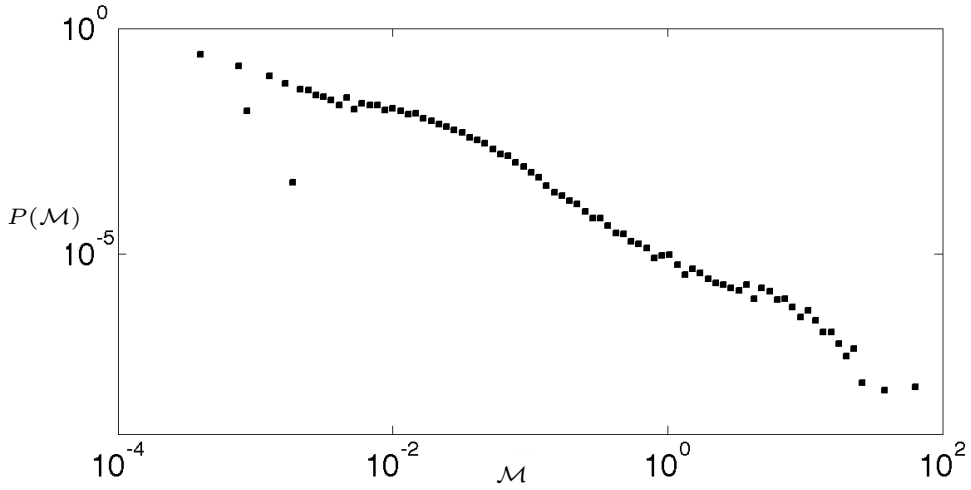

Figure 4.13: Log-log plot of the probability distribution function of $\mathcal{M}$ for all the avalanches of the transformation.

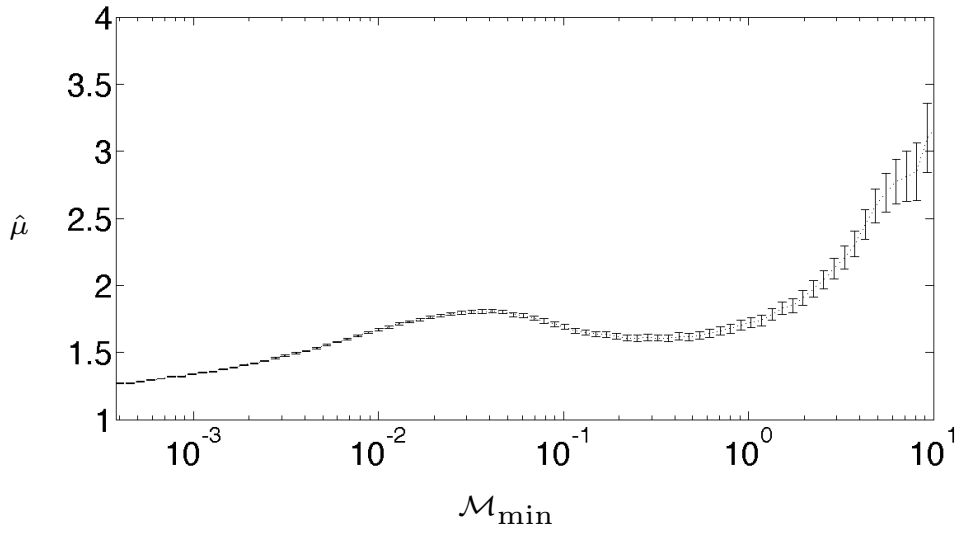

Figure 4.14: Behavior of the estimate $\hat{\mu}$ versus $\mathcal{M}_{\min}$.

Analogously, we make the same analysis for the size $\mathcal{S}$, for which we assume the law $p(\mathcal{S}) = \mathcal{S}^{-\delta}$. Thus, Figure 4.15 shows the log-log plot of the probability distribution function of the size while Figure 4.16 shows the behavior of the exponent estimate $\hat{\delta}$ versus the lower value $\mathcal{S}_{\text{min}}$. As expected, we can see the same kind of behavior for $\mathcal{S}$

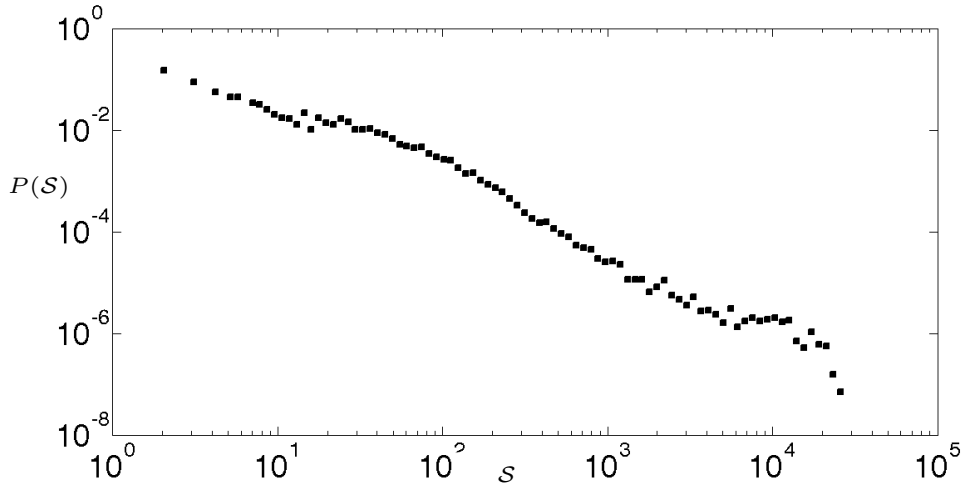

Figure 4.15: Log-log plot of the probability distribution function of $\mathcal{S}$ for all the avalanches of the transformation.

as for the magnitude $\mathcal{M}$, since we stated in Section 4.3.1 that the two quantities can be considered as equivalent. At the same time, it is possible to notice that the number of decades in $\mathcal{S}$ is slightly smaller than in $\mathcal{M}$ where we clearly see four decades. This is the consequence of $||\Delta\varepsilon||$ spanning over a decade, as explained in Section 4.3.1.

It would be interesting to compare our distributions with the already known experimental results in shape memory alloys, for example the ones obtained by acoustic emission measurements. Unluckily, there are two issues that make this comparison difficult to be made. The first one is that we are analyzing the distribution of magnitude and size for all the avalanches while in acoustic emission we have a temporal information and we do not distinguish among the events taking place in different parts of the specimen. This issue is easily solvable since it is sufficient to analyze the signals shown in Figures 4.8 and 4.9, by considering only the dependence on time. The second issue is that acoustic emission takes into account all the events in the specimen, both within it and on its surface while we only have the information on the surface. At the moment, there are no results on the scaling between three-dimensional and two-dimensional intermittency, so we cannot compare the different statistical distributions.

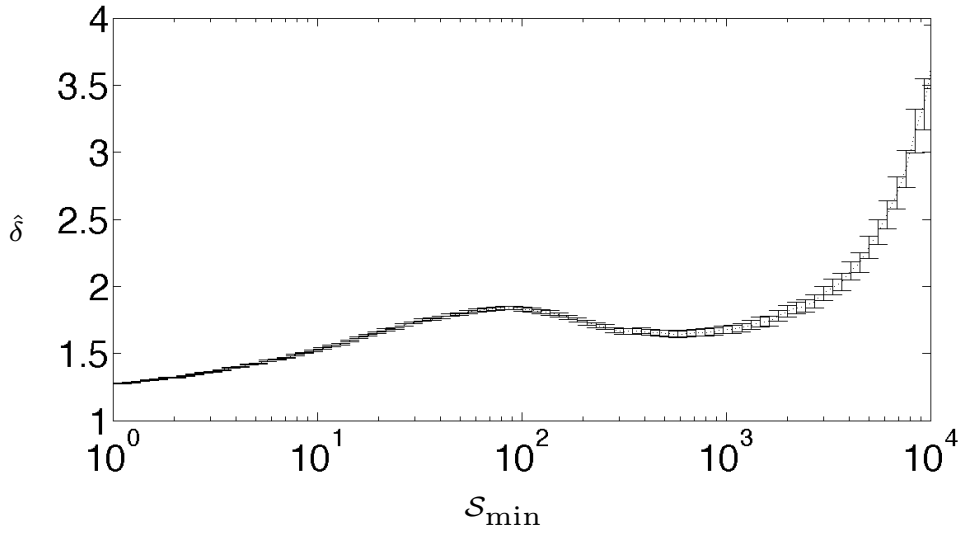

Figure 4.16: Behavior of the estimate $\hat{\delta}$ versus $\mathcal{S}_{\min}$.

4.3.4 Non-stationarity

The richness of data allows us to analyze also the non-stationarity of the transformation that we are testing. An intermittent process is said to be in a *stationary state* if its statistical features do not depend on time. It is important to underline that a non-stationary state is not an indication of non-equilibrium, since the system can be in equilibrium but still show different features in different moments, thus being non-stationary. It has been shown, for example in [33] in the case of magnetic intermittency, that whether there is stationarity or not actually influences the scaling of the avalanche distributions and provides different exponents.

By looking at the martensite variation or at the strain variation in all the previous sections, we can already notice that the signals are not uniformly distributed along the plateau, so that we can easily guess to be in a non-stationary state. The most immediate way to check if the system is in a stationarity state or not is to analyze the transformation in small time intervals. Different behaviors in different parts of the transformation will indicate the lack of stationarity. In order to do this kind of analysis, we divide the loading and unloading plateaus in three parts each, for a total of six blocks. Figure 4.17 shows the distribution of the avalanche magnitude for the different parts. The different curves do not collapse on the same heavy-tailed distribution but create a thick overall distribution. This suggests that each block is actually providing a different kind of con-

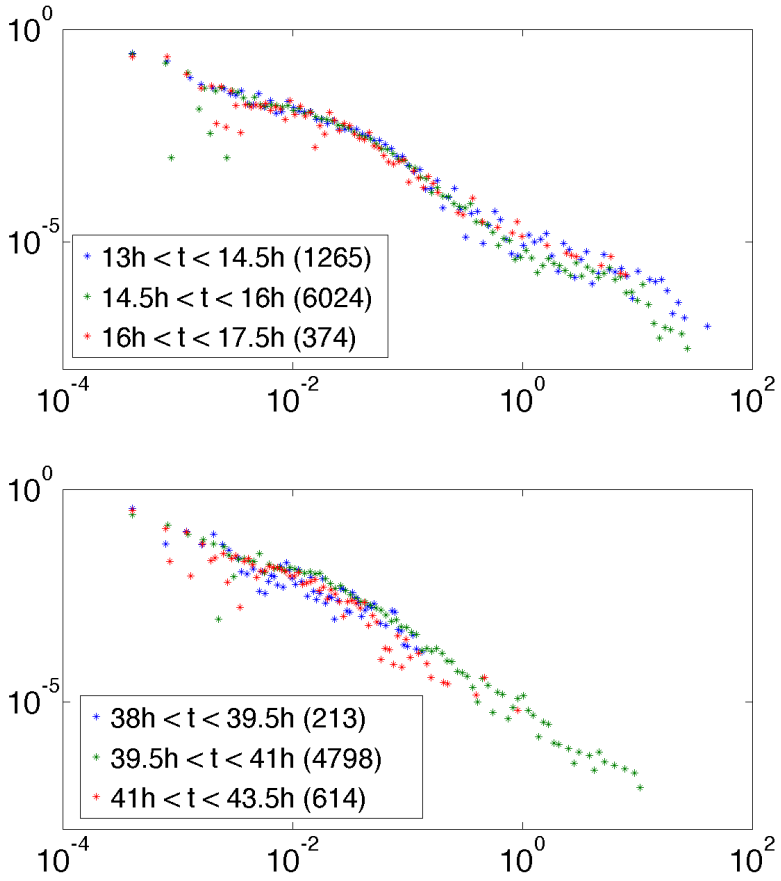

Figure 4.17: Log-log plot of the distributions of the avalanche magnitude $\mathcal{M}$ for six different time intervals in the transformation plateaus corresponding to loading (top) and unloading (bottom).

tribution to the final distribution in Figure 4.13.

The non-stationarity of the process is even clearer when comparing the estimates of the exponents for the distributions. Figure 4.18 shows the behavior of these estimates for different values of the lower bound $\mathcal{M}_{\text{min}}$. The differences among the various parts of the transformation are very easy to see: while for some intervals there is some stability in the estimate, for some others there are less decades and a more unstable behavior.

Since we have more than one distribution to compare, we can also provide an indicator of the goodness-of-fit for our empirical data. One of the most known tests in this sense is the *Kolmogorov-Smirnoff* test. In general, this test requires an empirical

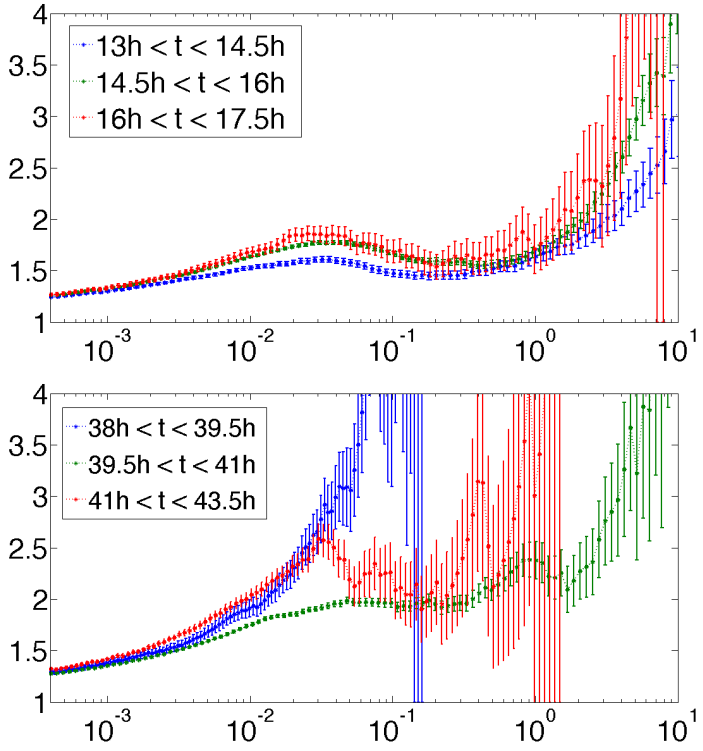

Figure 4.18: Estimates of the exponents for the avalanche magnitude $\mathcal{M}$ for the different time intervals during loading (top) and unloading (bottom).

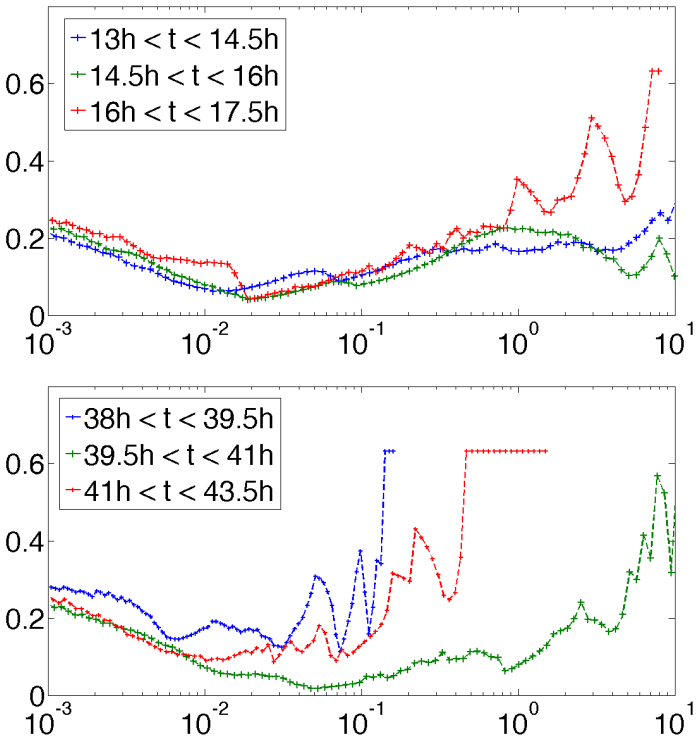

Figure 4.19: Kolmogorov-Smirnoff statistics for the avalanche magnitude $\mathcal{M}$ for the different time intervals during loading (top) and unloading (bottom).

distribution function F_n defined as

$$F_n(x) = \frac{1}{n}\sum_{i=1}^{n} I_{X_i \leq x},$$

where X_i are n i.i.d. observations and

$$I_{X_i \leq x} = \begin{cases} 1 & \text{if } X_i \leq x, \\ 0 & \text{if } X_i > x, \end{cases}$$

Given a theoretical cumulative distribution function $F(x) = Pr(X \leq x)$, the *Kolmogorov-Smirnoff (KS) statistic* is defined as

$$D_n = \sup_x |F_n(x) - F(x)|.$$

This statistic is very useful since it uses the cumulative distribution function so that the result does not depend on the kind of binning (logarithmic or linear) or on the amplitude of the bins.

The KS statistic thus provides a distance between the empirical distribution and the theoretical one. For non-parametrical tests, it is sufficient to compare this statistic with the quantiles of the Kolmogorov distribution to have a goodness-of-fit indicator. This is not possible when there is an estimated parameter in the theoretical distribution, like in our case. The only thing that we can do consists in comparing the KS statistics of the different parts of the plateaus among them. Figure 4.19 shows exactly the behavior of the KS statistics when varying $\mathcal{M}_{\text{min}}$. The distance seems to be comparable for most of the time intervals, except for the same two blocks (during the unloading) whose estimated exponent was unstable.

4.4 Conclusions

The global results in Chapter 3 supported the idea of an overall continuous behavior of the martensitic transformation. In this Chapter, thanks to the quantity and quality of our data, we managed to go into detail and see how this continuity is actually fictitious: the transformation occurs through intermittent events at different scales.

The two-dimensionality of the data allowed us to well characterize these events. Thus, we showed the relation between the magnitude and the size of avalanches. The two quantities are apparently equivalent since the possible jumps for each pixel of the avalanche can span for at maximum a decade. More freedom in the strain jumps, for example in case of plasticity, would provide a bigger difference between magnitude and size.

Moreover, we showed that both these quantities follow a heavy-tailed distribution that can be approximated by a power-law for a good number of decades. An estimate with the Maximum Likelihood method also shows a quite stable exponent for both the laws. Finally, we also proved the non-stationarity of our process, by obtaining different probability distributions for events in different parts of the transformation plateaus.

In conclusion, the combination of a suitable experimental device with a high-resolution full-field measurement technique allowed us to analyze various aspects (also some poorly investigated ones) of intermittency in a martensitic transformation.

CHAPTER 5

Macroscopic Modeling of Functional Fatigue

Until this moment, we focused on martensitic transformations without taking into account that this kind of materials usually shows fatigue and plastic effects. Microscopic models that satisfactorily explain this aspect are not available, yet. For this reason, in this chapter we present a macroscopic theory that focuses on the heart of the matter of permanent effects in SMAs.

5.1 Souza-Auricchio model

In this section we describe the Souza-Auricchio macroscopic model for SMAs [7, 90], with the plasticity description introduced in [9].

The first assumption of the Souza-Auricchio SMA model is the small-strain (though not necessarily small displacement) approximation [7, 56]. This conjecture allows for the use of a linear elastic approximation for the stored energy function. Moreover, we focus on a *quasi*-static regime for the microscopic evolution, in the sense of [80, §VI] as explained in Section 1.3.4. In words, we suppose that the time-scales of the macroscopic processes are much slower than the microscopic relaxation times. Moreover, we suppose the temperature to be homogeneous in the specimen, so that we do not need

a diffusion equation to be considered in the model. Some further modification to the model can be done in order to take into account for thermal diffusion [4, 7].

The thermo-mechanical model combines two different levels of evolution. On the macroscopic level, we consider the strain $\boldsymbol{E}$, defined in terms of the deformation gradient $\boldsymbol{F}$ as $\boldsymbol{E} = \frac{1}{2}(\boldsymbol{F}^T\boldsymbol{F} - \boldsymbol{I})$, where $\boldsymbol{I}$ is the identity tensor. We further take into account the spherical and deviatoric parts of $\boldsymbol{E}$ by considering $\boldsymbol{E} = \boldsymbol{e} + \frac{1}{3}E\,\boldsymbol{I}$, with $E = \mathrm{tr}\,\boldsymbol{E}$. Analogously, we use the Piola-Kirchhoff stress tensor $\boldsymbol{S}$ and its decomposition $\boldsymbol{S} = \boldsymbol{s} + \frac{1}{3}S\,\boldsymbol{I}$, with $S = \mathrm{tr}\,\boldsymbol{S}$
On the microscopic level, we introduce the transformation strain tensor $\boldsymbol{e}_{\text{tr}}$ and the functional fatigue tensor $\boldsymbol{q}$.
As regards the transformation strain tensor, it describes the martensitic microstructural transformation. In particular, its zero-value corresponds to complete austenitic phase, while a non-zero value indicates the presence of martensite. This martensite can be the combination of different variants, since we are not introducing any kind of information on its microstructural features. The aim is to model a multi-grain material, such that in every point it is possible to have several small grains with martensite variants that can be different among them. This approximation we introduced is not necessary in the original model, that can also be used to study non-homogeneity by considering a field of microscopic variables $\boldsymbol{e}_{\text{tr}}$ and $\boldsymbol{q}$.
Moreover, we assume the homogeneity of the material, i.e. we focus on a non-zero natural strain induced by the micro structural transformation, without taking into account for a spatial information within the specimen. In this sense, the transformation strain can be considered as equivalent to the volume fraction of martensite, that is a classical internal variable for this kind of models, like in the *State-Kinetic coupling theory* from Lemaitre and Marquis [57].
Furthermore, several experimental results exhibit small or negligible volume variations in most martensitic transitions [18]. In our case, to focus on isochoric microscopical transformations means to consider $\boldsymbol{e}_{\text{tr}}$ to be traceless. In order to understand this relation, let us introduce $\boldsymbol{F}_{\text{tr}}$ such that $\boldsymbol{e}_{\text{tr}} = \frac{1}{2}(\boldsymbol{F}_{\text{tr}}^T\boldsymbol{F}_{\text{tr}} - \boldsymbol{I})$. Now, let us suppose to have a small $\boldsymbol{e}_{\text{tr}}$, that is $\boldsymbol{F}_{\text{tr}} = \boldsymbol{I} + \boldsymbol{V}$ where $|\boldsymbol{V}| = \epsilon \ll 1$, and let us consider an isochoric deformation such that $\det(\boldsymbol{F}_{\text{tr}}) = 1$. The first assumption implies

$$\boldsymbol{e}_{\text{tr}} = \frac{1}{2}(\boldsymbol{V}^T + \boldsymbol{V} + o(\epsilon)) \quad \Rightarrow \quad \mathrm{tr}(\boldsymbol{e}_{\text{tr}}) = \mathrm{tr}\boldsymbol{V}.$$

As a consequence of the Jacobi's formula for the derivation of the determinant of a

matrix, it holds

$$\det(\boldsymbol{A}+\boldsymbol{X})-\det(\boldsymbol{A})=\det(\boldsymbol{A})\mathrm{tr}(\boldsymbol{A}^{-1}\boldsymbol{X})+o(\varepsilon).$$

If we substitute $\boldsymbol{A}=\boldsymbol{I}$ and $\boldsymbol{X}=\epsilon\boldsymbol{V}$ in the previous approximation, we obtain

$$\det(\boldsymbol{F}_{\mathrm{tr}}^{T}\boldsymbol{F}_{\mathrm{tr}})=1=1+\boldsymbol{V}+o(\varepsilon)\Rightarrow\mathrm{tr}(\boldsymbol{V})=o(\varepsilon),$$

thus relating the absence of volume change with a null trace for $\boldsymbol{e}_{\mathrm{tr}}$ (on a first order approximation). In any case, an adaptation to non-isochoric transformation can be easily obtained if the transformation dilation coefficient is provided.
As regards the functional fatigue $\boldsymbol{q}$, it can be seen as a measure of the microscopical plasticity induced by both macro and micro stresses.

These constitutive elements, together with the absolute temperature T, are related through the following expression of the Helmholtz potential density

$$\begin{aligned}\psi(\boldsymbol{E},\boldsymbol{e}_{\mathrm{tr}},\boldsymbol{q};T)=&\tfrac{1}{2}KE^{2}-3KE\alpha(T-T_{0})+G\left|\boldsymbol{e}-\boldsymbol{e}_{\mathrm{tr}}\right|^{2}\\&+\beta\left\langle T-M_{\mathrm{f}}\right\rangle\left|\boldsymbol{e}_{\mathrm{tr}}-\boldsymbol{q}\right|+\tfrac{1}{2}h\left|\boldsymbol{e}_{\mathrm{tr}}-\boldsymbol{q}\right|^{2}+\tfrac{1}{2}H\left|\boldsymbol{q}\right|^{2}+\mathscr{I}_{\mathcal{E}_{\mathrm{tr}}}(\boldsymbol{e}_{\mathrm{tr}}),\end{aligned}\tag{5.1}$$

where α (not explicitly included in [9], but present in [7]) is the thermal expansion coefficient, while K and G are respectively the bulk and shear modulus.

Let us analyze the different terms in the energy density, by keeping in mind that the equilibrium state of our continuum has to minimize it.

- $\frac{1}{2}KE^{2}$ is proportional to the trace of the macroscopic strain. This implies that it penalizes any macroscopic volume change since its contribute is small for small E;
- $-3KE\alpha(T-T_{0})$ is proportional to E as above but it is negative, so that it allows for volumes changes due to thermal expansion. Actually, α is usually very small, so that this term can be easily neglected with respect to the others;
- $G\left|\boldsymbol{e}-\boldsymbol{e}_{\mathrm{tr}}\right|^{2}$ is the elastic energy obtained by considering $\boldsymbol{e}_{\mathrm{tr}}$ as relaxed strain. The idea is that we can decompose the total deformation in a part due to the macroscopic transformation, $\boldsymbol{e}_{\mathrm{tr}}$, plus an elastic deformation whose zero-energy state corresponds to $\boldsymbol{e}_{\mathrm{tr}}$ itself;
- $\beta\left\langle T-M_{\mathrm{f}}\right\rangle\left|\boldsymbol{e}_{\mathrm{tr}}-\boldsymbol{q}\right|$ where $\left\langle\,\cdot\,\right\rangle:=\max\{\,\cdot\,,0\}$. This term is active for high temperatures, above M_{f}, that is when austenite starts being preferred instead of martensite. Let us imagine to have $\boldsymbol{q}=\boldsymbol{0}$ and $T>M_{\mathrm{f}}$, then this term pushes the microscopic strain $\boldsymbol{e}_{\mathrm{tr}}$ towards the null value, that is towards austenite. When $\boldsymbol{q}\neq\boldsymbol{0}$, $\boldsymbol{e}_{\mathrm{tr}}$ is pushed exactly towards $\boldsymbol{q}$, that is its reference value when fatigue arises;

- $\frac{1}{2}h\,|\boldsymbol{e}_{\text{tr}} - \boldsymbol{q}|^2$. As the previous one, this term pushes $\boldsymbol{e}_{\text{tr}}$ towards the functional fatigue $\boldsymbol{q}$. But the two terms are obviously different. First of all, this h-term does not show any dependence on temperature. Moreover, the β-term dependence on $\boldsymbol{e}_{\text{tr}}$ is linear while the h-term exhibits a quadratic dependence. This implies that, when $T > M_{\text{f}}$, a driving force is induced by the β-term even for small residual transformation strains;
- $\frac{1}{2}H\,|\boldsymbol{q}|^2$ models the plastic hardening of the material, *i.e.* it penalizes an excessive growth of the functional fatigue;
- The indicator function

$$\mathscr{I}_{\mathcal{E}_{\text{tr}}}(\boldsymbol{e}_{\text{tr}}) = \begin{cases} 0 & \text{if } (\boldsymbol{e}_{\text{tr}}) \in \mathcal{E}_{\text{tr}} \\ \infty & \text{if } (\boldsymbol{e}_{\text{tr}}) \notin \mathcal{E}_{\text{tr}} \end{cases}$$

  introduces a constrain on the microscopic deformation through the definition of a microscopic transformation domain $\mathcal{E}_{\text{tr}}$.

We already said that we are considering a multi-grain material in which each grain can transform into a different variant of martensite. Now, $\boldsymbol{e}_{\text{tr}}$ can be seen to represent the total strain by linearly combining the local strains of the different grains.
Obviously, there is an upper bound for $\boldsymbol{e}_{\text{tr}}$ and we denote it by ε_{L}. The value of ε_{L} can be interpreted as the total maximum strain when all the local grains are oriented in the same direction. It is related to the size of the Bain matrices associated to the underlying austenite-martensite transition (see Section 1.2.2).

For simplicity, we assume the microscopic domain to be a ball of constant radius ε_{L}

$$\mathcal{E}_{\text{tr}} = \Big\{ \boldsymbol{e}_{\text{tr}} : \boldsymbol{e}_{\text{tr}} = \boldsymbol{e}_{\text{tr}}^T,\ \text{tr}\,\boldsymbol{e}_{\text{tr}} = 0,\ |\boldsymbol{e}_{\text{tr}}| \leq \varepsilon_{\text{L}} \Big\}. \tag{5.2}$$

Some changes in this domain will be introduced and detailed in Section 5.2.2.

We further introduce the velocity fields associated to the microscopic variables

$$\boldsymbol{L}_{\text{tr}} = \dot{\boldsymbol{e}}_{\text{tr}} \qquad \text{and} \qquad \boldsymbol{L}_{\text{q}} = \dot{\boldsymbol{q}}, \tag{5.3}$$

together with the driving forces, obtained by derivation of the Helmholtz potential [9, 80]

$$\boldsymbol{X} = -\frac{\partial \psi}{\partial \boldsymbol{e}_{\text{tr}}} \qquad \text{and} \qquad \boldsymbol{Q} = -\frac{\partial \psi}{\partial \boldsymbol{q}}. \tag{5.4}$$

In order to complete the model, we need a rate of dissipation density as required in the Rajagopal theory introduced in Section 1.3.2. This density should depend on the internal variables $\boldsymbol{e}_{\text{tr}}$ and $\boldsymbol{q}$ and on their velocities $\boldsymbol{L}_{\text{tr}}$ and $\boldsymbol{L}_{\text{q}}$. Though, the *maximum rate of dissipation criterion* (according to theorem 1.3.5 in Section 1.3.3), the dissipation

actually depends on $(\boldsymbol{L}_{\mathrm{tr}}, \boldsymbol{L}_{\mathrm{q}})$ through the driving forces $(\boldsymbol{X}, \boldsymbol{Q})$ [80]. This implies that our last ingredient is a dissipation density function of the form

$$\xi(\boldsymbol{e}_{\mathrm{tr}}, \boldsymbol{q}, \mathbf{X}, \mathbf{Q}) = \xi(\mathbf{X}, \mathbf{Q}). \tag{5.5}$$

The possible choices for this function and its interpretation are detailed in Section 5.2.3.

According to the Rajagopal theory, the *quasi*-static evolution assumption implies that the macroscopic evolution occurs only when the rate of dissipation is non-positive (see Section 1.3.4). In this sense, the rate of dissipation function defines an elastic domain as explained in Section 1.3.1. This domain depends on $\boldsymbol{X}$ and $\boldsymbol{Q}$ and shows the following features:

- the macroscopic evolution is forced to take place within this domain or at most on its boundary;
- the microscopic order parameters evolve only in correspondence to the border of the elastic domain.

Moreover, one of the main consequences of the maximum rate of dissipation criterion is that the pair of the velocity fields $(\boldsymbol{L}_{\mathrm{tr}}, \boldsymbol{L}_{\mathrm{q}})$ is parallel to the outward unit normal to the boundary of the elastic domain defined by $\xi(\mathbf{X}, \mathbf{Q}) \leq 0$. Accordingly to this criterion, it is possible to introduce the flow rules for the microscopic variables according to (1.15) as follows

$$\dot{\boldsymbol{e}}_{\mathrm{tr}} = \lambda \frac{\partial \xi}{\partial \boldsymbol{X}}, \qquad \dot{\boldsymbol{q}} = \lambda \frac{\partial \xi}{\partial \boldsymbol{Q}}. \tag{5.6}$$

These equations have to be coupled with the condition on the rate of dissipation density, in order to stay on the boundary of the elastic domain. Thus, we introduce the following Karush-Kuhn-Tucker conditions

$$\lambda \geq 0, \qquad \xi \leq 0, \qquad \lambda \xi = 0, \tag{5.7}$$

so that the multiplier λ is null within the elastic domain ($\xi < 0$) and can be different from zero only for $\xi = 0$, that is on the boundary of the elastic domain where the evolution of the interval variables is allowed.

5.2 Functional fatigue in the Souza-Auricchio model

The model that we described in the previous section is our starting point for the introduction of new features in order to better predict the appearance of functional fatigue. In this section, we present the novelties we included with the purpose of improving the Souza-Auricchio model. We start by inserting a macroscopic-plasticity term in the

Helmholtz potential, then we detail the evolution for the microscopic domain and we compare different choices for the dissipation function.

5.2.1 Macroscopic plasticity

Let us decompose the deformation gradient by taking into account the different parts of the total process

$$\boldsymbol{F} = \boldsymbol{F}_{\text{el}}\,\boldsymbol{F}_{\text{tr}}\,\boldsymbol{F}_{\text{pl}}.$$

Actually, we can interpret our total deformation as a previous plastic deformation from a reference configuration, followed by a further deformation due to the microscopic transformation and concluded by an elastic deformation with respect to this last deformed state, as represented in Figure 5.1.

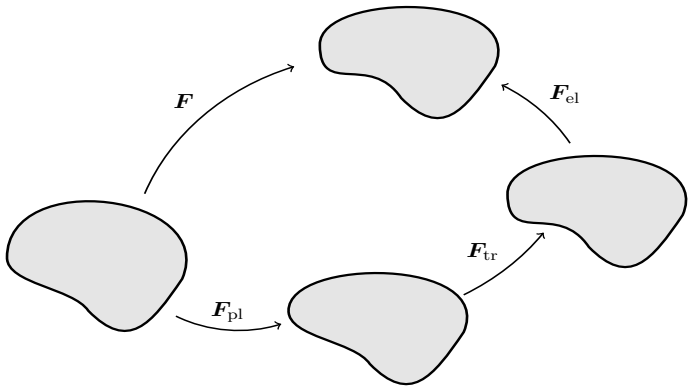

Figure 5.1: Decomposition of the macroscopic strain $\boldsymbol{F}$ in its elastic, transformation and plastic component.

The small deformation hypothesis under which we work allows us to suppose the following form for the different factors, as explained in [47]

$$\boldsymbol{F}_{\text{pl}} = \boldsymbol{I} + \boldsymbol{H}_{\text{pl}}, \qquad \boldsymbol{F}_{\text{tr}} = \boldsymbol{I} + \boldsymbol{H}_{\text{tr}}, \qquad \boldsymbol{F}_{\text{el}} = \boldsymbol{I} + \boldsymbol{H}_{\text{el}},$$

where $|\boldsymbol{H}_{\text{pl}}|, |\boldsymbol{H}_{\text{tr}}|$ and $|\boldsymbol{H}_{\text{el}}|$ are of order $\varepsilon \ll 1$. We can thus compute the strain tensor $\boldsymbol{E} = \frac{1}{2}(\boldsymbol{F}^T\boldsymbol{F} - \boldsymbol{I})$ by taking into account the decomposition of $\boldsymbol{F}$ and the small deformation hypothesis and obtain

$$\boldsymbol{E} = \frac{1}{2}(\boldsymbol{H}_{\text{el}}^T + \boldsymbol{H}_{\text{el}}) + \frac{1}{2}(\boldsymbol{H}_{\text{tr}}^T + \boldsymbol{H}_{\text{tr}}) + \frac{1}{2}(\boldsymbol{H}_{\text{pl}}^T + \boldsymbol{H}_{\text{pl}}) + o(\varepsilon) = \boldsymbol{E}_{\text{el}} + \boldsymbol{E}_{\text{tr}} + \boldsymbol{E}_{\text{pl}} + o(\varepsilon).$$

By focusing only on the traceless parts of the deformation tensors, we can write

$$\boldsymbol{e} = \boldsymbol{e}_{\text{el}} + \boldsymbol{e}_{\text{pl}} + \boldsymbol{e}_{\text{tr}},$$

where $\boldsymbol{e}_{\text{el}} = \boldsymbol{E}_{\text{el}} - \frac{1}{3}\operatorname{tr}(\boldsymbol{E}_{\text{el}})\boldsymbol{I}$ and $\boldsymbol{e}_{\text{el}} = \boldsymbol{E}_{\text{pl}} - \frac{1}{3}\operatorname{tr}(\boldsymbol{E}_{\text{pl}})\boldsymbol{I}$.
Thus, we modify the shear elastic term in the Helmholtz potential as
$G\,|\boldsymbol{e} - \boldsymbol{e}_{\text{tr}} - \boldsymbol{e}_{\text{pl}}|^2$.
At this point, it is necessary to settle an expression for $\boldsymbol{e}_{\text{pl}}$. For simplicity, we assume a linear proportionality between the plastic macroscopic strain and the functional fatigue tensor $\boldsymbol{q}$, by prescribing $\boldsymbol{e}_{\text{pl}} = a\,\boldsymbol{q}$.
This modification implies a further adjustment as regards the rate of dissipation function, and by consequence the evolution of the functional fatigue, as explained in section 5.2.3

5.2.2 Evolving microscopic domain

We already described the interpretation of the microscopic domain $\mathcal{E}_{\text{tr}}$ in Section 5.1. Until this moment, the internal variable $\boldsymbol{q}$ was not involved in the definition of $\mathcal{E}_{\text{tr}}$ or in the choice of ε_{L}. Here, we modify the microscopic domain in order to take into account the influence of the functional fatigue $\boldsymbol{q}$ on this constrain.
As already said, the functional fatigue is a measure of the microscopic plasticity, that is the part of the non-recoverable transformation strain. An increase of $\boldsymbol{q}$ can be seen as freezing the orientation of some of the mentioned grains. This fact implies that, whenever $\dot{\boldsymbol{q}} \neq \boldsymbol{0}$, the material loses the possibility to reach previously available configurations.
In order to provide an evolution law for the microscopic domain we start by supposing a spherical domain in the space of symmetrical traceless tensors centered in $\boldsymbol{q}$, so that $\mathcal{E}_{\text{tr}}(\boldsymbol{e}_{\text{tr}}, \boldsymbol{q}, t)$ is actually a $\mathcal{E}_{\text{tr}}(\boldsymbol{r}, t)$ where $\boldsymbol{r} = \boldsymbol{e}_{\text{tr}} - \boldsymbol{q}$. Moreover, the domain has the possibility to shrink but cannot expand because the transformation loses freedom without gaining new possible configurations. This means that, given $t_2 \geq t_1$ we require that $\mathcal{E}_{\text{tr}}(\boldsymbol{r}, t_2) \subseteq \mathcal{E}_{\text{tr}}(\boldsymbol{r}, t_1)$. At the same time, we do not want the shrinking to be excessive thus we select the largest ball among those which satisfy our criteria.

This kind of evolution is described by the following proposition.

Proposition 5.2.1. *The radius ε_L of the transformation domain evolves along solutions of the differential equation*

$$\dot{\varepsilon}_L(\boldsymbol{r}, t) = \begin{cases} -|\dot{\boldsymbol{q}}(\boldsymbol{r}, t)| & \text{if } \varepsilon_L(\boldsymbol{r}, t) > 0 \\ 0 & \text{if } \varepsilon_L(\boldsymbol{r}, t) = 0, \end{cases} \qquad \text{with} \quad \varepsilon_L(\boldsymbol{r}, t_0) = \varepsilon_{L0}. \tag{5.8}$$

Proof. Let $\boldsymbol{q}(\boldsymbol{r}, t)$ denote the value of the functional fatigue tensor at the material point

$\boldsymbol{r}$ at time t (see Figure 5.2 for reference). The transformation domain will then be

$$\mathcal{E}_{\rm tr}(\boldsymbol{r},t)=\Big\{\boldsymbol{e}_{\rm tr}:\boldsymbol{e}_{\rm tr}=\boldsymbol{e}_{\rm tr}^{T},\ {\rm tr}\,\boldsymbol{e}_{\rm tr}=0,\ |\boldsymbol{e}_{\rm tr}-\boldsymbol{q}(\boldsymbol{r},t)|\leq\varepsilon_{\rm L}(\boldsymbol{r},t)\Big\}. \tag{5.9}$$

When $\boldsymbol{q}$ evolves (say, from $\boldsymbol{q}^{\rm old}$ to $\boldsymbol{q}^{\rm new}$ as illustrated in Figure 5.2), we need to identify the largest ball, among those centered in $\boldsymbol{q}^{\rm new}$, which is completely within $\mathcal{E}_{\rm tr}^{\rm old}$. The radius of such ball is clearly to be decreased (with respect to $\varepsilon_{\rm L}^{\rm old}$) exactly by the amount $|\boldsymbol{q}^{\rm new}-\boldsymbol{q}^{\rm old}|$. When passing to differential evolution, equation $(5.8)_1$ is thus easily recovered. Evolution of the transformation domain ends when the domain itself is turned to a point ($\varepsilon_{\rm L}=0$). □

It is important to notice that the sign of the variation of the functional fatigue does not affect the evolution of $\varepsilon_{\rm L}$: not only the increasing but also the decreasing of $\boldsymbol{q}$, even to the initial null value, entails irreversibility.

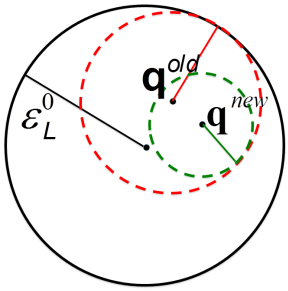

Figure 5.2: Representation of the evolving transformation domain. Any change in the functional fatigue tensor automatically turns into a reduction of the radius of the transformation domain.

5.2.3 Dissipation functional

A further modification arises from the necessity of taking into account plastic effects that are not related to microscopic transformations. Actually, the causes of plasticity in shape memory alloys can be of two kinds: repeated microscopic phase transitions, but also the enforcement of a macroscopic strain beyond a certain threshold [50]. At the same time, it is possible to have a microscopic transformation without any creation of plasticity. Indeed, it is possible to experimentally prove that after a limited number of thermal cycles (*training* of the sample [6, 60]), no more macroscopic plasticity emerges for up to thousands of cycles, though the microstructure keeps on changing [51, 99]. Since in section 5.2.1 we related the macroscopic plasticity to the functional fatigue $\boldsymbol{q}$, it becomes necessary to modify the original dissipation rate function (5.5) in order to obtain a greater independence between microscopic strain and plasticity. As already

stated, the evolution of the internal variables occurs only when the driving forces $\boldsymbol{X}$ and $\boldsymbol{Q}$ reach the boundary of the elastic domain defined by the 0-level state of the dissipation rate function. As explained in Section 5.1 and specified by (5.6), the shape of the elastic domain affects also the direction of the evolution, since the pair $(\dot{\boldsymbol{e}}_{\text{tr}}, \dot{\boldsymbol{q}})$ is parallel to the normal vector on the boundary. This means that a slight change in the definition of the dissipation rate can deeply modify the kind of evolution.

Let us define the norm $\|\cdot\|_{\kappa,p}$ on $(\boldsymbol{X}, \boldsymbol{Q})$ such that

$$\|(\boldsymbol{X}, \boldsymbol{Q})\|_{\kappa,p} = \begin{cases} (|\boldsymbol{X}|^p + \kappa^p |\boldsymbol{Q}|^p)^{1/p} & p < \infty, \\ \max\{|\boldsymbol{X}|, \kappa|\boldsymbol{Q}|\} & p = \infty. \end{cases}$$

By using this definition, we can rewrite the rate of dissipation density that is introduced in [7, 9] in the following way:

$$\xi_1 = \max\{\|(\mathbf{X}, \mathbf{Q})\|_{\kappa,1} - R,\, 0\} \quad \text{(weighted } \ell_1 \text{ or taxicab norm)}. \tag{5.10}$$

The parameter κ settles a scaling between the transformation effect related to $\mathbf{X}$ and the fatigue related to $\mathbf{Q}$. The parameter R can be interpreted as the radius of the elastic domain introduced in Section 5.1 and defined by the general condition $\xi \leq 0$.
In addition to this expression for the dissipation density function, we propose and analyze two further possible choices:

$$\xi_2 = \max\Big\{\|(\boldsymbol{X}, \boldsymbol{Q})\|_{\kappa,2} - R,\, 0\Big\}, \qquad \text{(weighted } \ell_2 \text{ or Euclidean norm)} \tag{5.11}$$

$$\xi_\infty = \max\Big\{\|(\boldsymbol{X}, \boldsymbol{Q})\|_{\kappa,\infty} - R,\, 0\Big\}. \qquad \text{(weighted } \ell_\infty \text{ or supremum norm)} \tag{5.12}$$

Figure 5.3 shows the different shapes of the elastic domains induced by the different choices for the dissipation function, together with the unit normals to the boundary.

- **Weighted taxicab norm.** The main limit of this choice for the dissipation rate function lies in the too strong dependence between the evolution of $\dot{\boldsymbol{e}}_{\text{tr}}$ and $\dot{\boldsymbol{q}}$. Indeed, the unit normal determines an angle with the $|\boldsymbol{X}|$ axis which is constant and equal to $\phi = \arctan\kappa$. In this case, equation (5.6) has the following form

  $$\dot{\boldsymbol{e}}_{\text{tr}} = \lambda \frac{\boldsymbol{X}}{|\boldsymbol{X}|}, \qquad \dot{\boldsymbol{q}} = \lambda\, \kappa \frac{\boldsymbol{Q}}{|\boldsymbol{Q}|}$$

  so that the evolution of the internal variables is strongly coupled as

  $$|\dot{\boldsymbol{q}}| = \kappa |\dot{\boldsymbol{e}}_{\text{tr}}| = \tan\phi\, |\dot{\boldsymbol{e}}_{\text{tr}}|.$$

  This kind of interaction implies that every microscopic transformation creates plasticity. At the same time, the creation of plasticity is possible only when caused

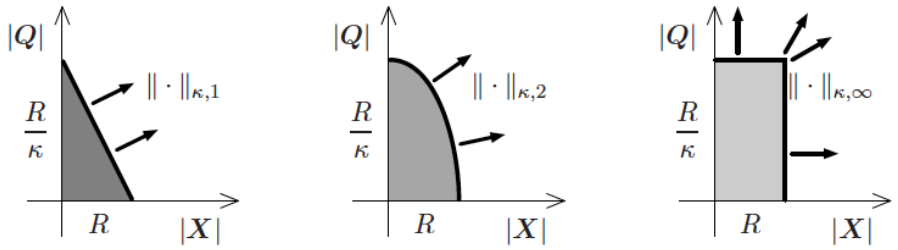

Figure 5.3: Different elastic domains induced by different rate of dissipation functions. In all plots, the scaling modulus κ has been set equal to $\frac{1}{2}$.

by a microscopic transformation. This behaviour is not in agreement with the experimental evidence cited at the beginning of this section.

- **Weighted Euclidean norm.** In this case, the angle ϕ between the horizontal axis and the unit normal varies along the boundary. In particular, the two limit behaviors that cannot be described by the choice of the taxicab norm are now reproducible by considering the points $(R, 0)$ and $(0, R/\kappa)$ in the domain in the middle of Figure 5.3. In the first case, it is possible to model the effect of microscopic transformations with negligible plasticity creation. By approaching the point $(R, 0)$ we move towards having $|\dot{\boldsymbol{e}}_{\text{tr}}| \gg |\dot{\boldsymbol{q}}|$, as for the experimental cycles after the training phase.
  The $(0, R/\kappa)$ configuration is almost the opposite. Let us suppose to pull the specimen in order to reach the complete martensitic phase. In this case, the constrain induced by the indicator function $\mathscr{I}_{\mathcal{E}_{\text{tr}}}$ impedes the evolution of $\boldsymbol{e}_{\text{tr}}$, by forcing $\boldsymbol{X}$ within the elastic domain. By keeping on stretching the specimen, we obtain an increasing in $\boldsymbol{Q}$ eventually touching the boundary of the elastic domain in a neighborhood of the point $(0, R/\kappa)$. Thus, this is the case of development of macroscopic plasticity without evolution in the microscopic strain.

- **Weighted supremum norm.** This case shows the same modeling abilities as the choice of the Euclidean norm but with even more freedom. The two microscopic variables can now evolve completely independently, by reaching two different thresholds (R for $|\boldsymbol{X}|$ and R/κ for $\boldsymbol{Q}$). Thus, three outcomes are possible: evolving microscopic strain with negligible plasticity (vertical boundary, $\dot{\boldsymbol{e}}_{\text{tr}} \neq 0$ and

$\dot{\boldsymbol{q}} = 0$), plasticity without phase transformation (horizontal boundary, $\dot{\boldsymbol{e}}_{\text{tr}} = 0$ and $\dot{\boldsymbol{q}} \neq 0$) and microscopic strain with plasticity, *i.e.* the evolution of both the internal variables (upper-right corner of the domain in Figure 5.3). This freedom is due to the use of two different Lagrange multipliers for the evolution of the two variables, since equations (5.6)-(5.7) take the following form

$$\dot{\boldsymbol{e}}_{\text{tr}} = \begin{cases} \lambda\, \boldsymbol{X} & \text{if } |\boldsymbol{X}| \geq R\,(\lambda \geq 0), \\ \\ \mathbf{0} \text{ otherwise} \end{cases} \tag{5.13}$$

$$\dot{\boldsymbol{q}} = \begin{cases} \mu\, \boldsymbol{Q} & \text{if } \kappa|\boldsymbol{Q}| \geq R\,(\mu \geq 0), \\ \mathbf{0} & \text{otherwise.} \end{cases} \tag{5.14}$$

5.3 Thermally-induced transformation

In this section we focus on a thermally-induced experiment, usually important in many SMA applications (for example as actuators). In particular, we describe the main numerical experiment that has been done in order to test the model. Afterwards, we detail a possibility of parameter calibration and we analyze the effects of functional fatigue.

5.3.1 Description of the numerical experiment

We study the *quasi*-static evolution of a specimen under constant uniaxial stress, both traction and compression, applied to both the extremities. While the stress is held constant, we uniformly vary the temperature, by performing cycles from high to low temperatures and viceversa and thus inducing the microscopic transformation. We assume uniaxial symmetry and homogeneity for all the induced deformations.
The momentum balance equation

$$\operatorname{div} \boldsymbol{S} = \mathbf{0} \tag{5.15}$$

is automatically satisfied because of the homogeneity of the deformations, so that the stress tensor is determined by the boundary conditions. The use of a static equilibrium equation is justified by the assumption of *quasi*-static evolution, since the variation of the control parameters (temperature and stress) is assumed to be much slower than the microscopic relaxation times. Thus, we need the flow rules (5.6)-(5.7) for the internal variables while we fix the external loading. The Piola-Kirchhoff stress tensor that has to be used in (5.15) is related to the variables through the Helmholtz potential (5.1) as

$$S = \frac{\partial \psi}{\partial E}, \qquad \boldsymbol{s} = \frac{\partial \psi}{\partial \boldsymbol{e}}. \tag{5.16}$$

The origin of this expression is detailed in Section 1.3.2 where equation (1.11) is obtained.

The results will be characterized by the presence of an hysteresis loop in the evolution of the strain with respect to the temperature. The existence of this loop is due to the non uniqueness of the solution to our problem in correspondence of the same external load. The physical equilibrium is chosen at each step in order to respect continuity.

Let us detail the experiment. We start at a temperature corresponding to stable austenitic phase and we move towards low temperatures. By lowering the temperature, we make $\boldsymbol{X}$ reach the border of the elastic domain, thus initiating the microscopic transformation. The constant load stops the transformation before the martensite final temperature, that is for $T_1 > M_\mathrm{f}$. Once the temperature variation is reversed, austenite starts re-appearing at a temperature $T_2 > T_1$, since the point on the boundary of the elastic domain in which $\boldsymbol{X}$ ends up is different than for the forward transformation. The temperature interval $[T_1, T_2]$, that characterizes the hysteresis loop, corresponds to a high probability of developing plasticity, since $\boldsymbol{q}$ evolves towards a high value of $\boldsymbol{e}_\mathrm{tr}$. This is also in agreement with the general idea of linking plasticity to the width of the hysteresis loop (measured as $T_2 - T_1$ for thermal experiments) [107].Eventually, a non-zero value of the functional fatigue at the end of the loop may influence the following cycles, according with its interpretation as microscopic plasticity.

The test is performed under symmetry assumptions which simplify the equations introduced in section 5.1. Let us define the following tensor $\boldsymbol{i} = \boldsymbol{e}_z \otimes \boldsymbol{e}_z - \frac{1}{3}\boldsymbol{I}$, to which all the other traceless, axially symmetric tensors are proportional, so that we can write

$$\boldsymbol{s} = s\,\boldsymbol{i},\ \boldsymbol{e} = e\,\boldsymbol{i},\ \boldsymbol{e}_\mathrm{tr} = e_\mathrm{tr}\,\boldsymbol{i},\ \boldsymbol{q} = q\,\boldsymbol{i},\ \boldsymbol{X} = X\,\boldsymbol{i} \text{ and } \boldsymbol{Q} = Q\,\boldsymbol{i}.$$

We recall that, after the modifications introduced in the previous sections, the Helmholtz free energy of equation (5.1) now has the following expression:

$$\begin{aligned}\psi(\boldsymbol{E}, \boldsymbol{e}_\mathrm{tr}, \boldsymbol{q}; T) = {} & \tfrac{1}{2}KE^2 - 3KE\alpha(T - T_0) + G\,|\boldsymbol{e} - \boldsymbol{e}_\mathrm{tr} - a\boldsymbol{q}|^2 \\ & + \beta\,\langle T - M_\mathrm{f}\rangle\,|\boldsymbol{e}_\mathrm{tr} - \boldsymbol{q}| + \tfrac{1}{2}h\,|\boldsymbol{e}_\mathrm{tr} - \boldsymbol{q}|^2 + \tfrac{1}{2}H\,|\boldsymbol{q}|^2 + \mathscr{I}_{\mathcal{E}_\mathrm{tr}}(\boldsymbol{e}_\mathrm{tr} - \boldsymbol{q}).\end{aligned} \tag{5.17}$$

By using this expression and the relation (5.16), we obtain the following equations:

$$E = \frac{S}{K} + 3\alpha(T - T_0), \qquad s = 2G(e - e_\mathrm{tr} - aq).$$

Analogously, we can obtain the expressions for $\boldsymbol{X}$ and $\boldsymbol{Q}$ by differentiation of the Helmholtz free energy and by recalling that for a generic tensor in the direction $\boldsymbol{d}$,

$\boldsymbol{T} = T\boldsymbol{d}$, it holds

$$\frac{\partial|\boldsymbol{T}|}{\partial \boldsymbol{T}} = \operatorname{sgn} T.$$

This relation helps in dealing with the last two terms of the Helmholtz free energy so that for the β-term we have

$$\begin{aligned}\frac{\partial}{\partial \boldsymbol{e}_{\text{tr}}}\beta \langle T - M_{\text{f}}\rangle|\boldsymbol{e}_{\text{tr}} - \boldsymbol{q}| &= \beta \langle T - M_{\text{f}}\rangle \frac{\partial|\boldsymbol{e}_{\text{tr}} - \boldsymbol{q}|}{\partial(\boldsymbol{e}_{\text{tr}} - \boldsymbol{q})}\frac{\partial(\boldsymbol{e}_{\text{tr}} - \boldsymbol{q})}{\partial \boldsymbol{e}_{\text{tr}}} \\ &= \beta \langle T - M_{\text{f}}\rangle \operatorname{sgn}(\boldsymbol{e}_{\text{tr}} - \boldsymbol{q}). \end{aligned} \tag{5.18}$$

Moreover, we denote by γ the following derivative:

$$\gamma = \frac{\partial \mathscr{I}_{\mathcal{E}_{\text{tr}}}(\boldsymbol{e}_{\text{tr}} - \boldsymbol{q})}{\partial|\boldsymbol{e}_{\text{tr}} - \boldsymbol{q}|},$$

so that

$$\begin{aligned}\gamma &= 0 \quad \text{if } |\boldsymbol{e}_{\text{tr}} - \boldsymbol{q}| \in \mathcal{E}_{\text{tr}} \setminus \partial\mathcal{E}_{\text{tr}} \\ \gamma &\geq 0 \quad \text{if } |\boldsymbol{e}_{\text{tr}} - \boldsymbol{q}| \in \partial\mathcal{E}_{\text{tr}}\end{aligned} \tag{5.19}$$

and

$$\frac{\partial \mathscr{I}_{\mathcal{E}_{\text{tr}}}(\boldsymbol{e}_{\text{tr}} - \boldsymbol{q})}{\partial \boldsymbol{e}_{\text{tr}}} = \gamma \operatorname{sgn}(\boldsymbol{e}_{\text{tr}} - \boldsymbol{q}).$$

Under our assumptions on symmetry, we thus obtain

$$X = s + h(q - e_{\text{tr}}) + \Big(\gamma + \beta \langle T - M_{\text{f}}\rangle\Big) \operatorname{sgn}(q - e_{\text{tr}}), \tag{5.20}$$

$$Q = as + h(e_{\text{tr}} - q) - Hq + \beta \langle T - M_{\text{f}}\rangle \operatorname{sgn}(e_{\text{tr}} - q), \tag{5.21}$$

together with the flow rules (5.6)-(5.7) for the internal variables, whose actual expression depends on the choice of the dissipation function ξ.

5.3.2 Parameter calibration

We now use the experiment that has been introduced in the previous section to calibrate the value of the relevant parameters in the model. Figure 5.4 shows the results of a thermal cycle performed by choosing the rate of dissipation function ξ_∞, though qualitatively similar results could be obtained with the Euclidean choice ξ_2. Figure 5.5a shows the position of points B, C, E and F of Figure 5.5 in the elastic domain induced by the choice of ξ_∞, together with the direction of the evolution of the internal variables. Moreover, Figure 5.5b describes the evolution of the microscopic domain $\mathcal{E}_{\text{tr}}$ during the same cycle. Since the test is performed under the symmetry conditions introduced in the previous section, both $\boldsymbol{e}_{\text{tr}}$ and $\boldsymbol{q}$ will evolve along the same direction $\boldsymbol{i} = \boldsymbol{e}_z \otimes \boldsymbol{e}_z - \frac{1}{3}\boldsymbol{I}$, so that we can represent our spherical domain as a line.

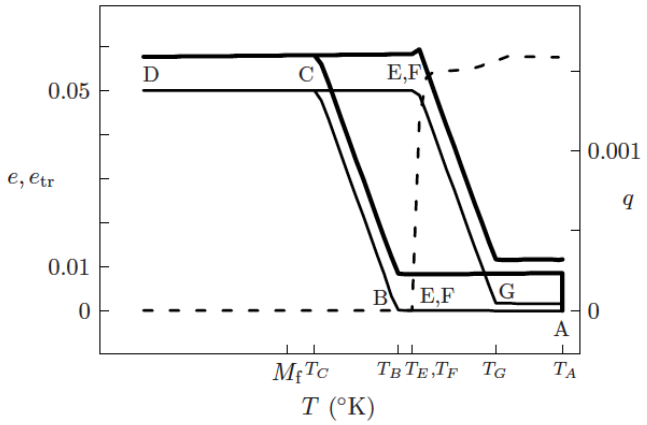

Figure 5.4: Evolution of a specimen subject to a thermal cycle across the martensite finish temperature M_f, under a constant uniaxial load $s = 150$MPa. The bold line displays the macroscopic strain e, the thin line indicates the transformation strain e_{tr} (both in the left scale), while the dashed plot reports the behavior of the functional fatigue q (in a different scale, illustrated on the right). The value of the constitutive parameters have been set equal to the following realistic values: $K = 34.3$GPa, $G = 13.2$GPa, $\alpha = 10^{-5}/°$K, $\beta = 6.71$MPa/°K, $h = 2$GPa, $H = 4$GPa, $\varepsilon_L = 6.12 \times 10^{-2}$, $R = 75.1$MPa, $\kappa = 0.14$, $a = 0.9$, $M_f = 330°$K.

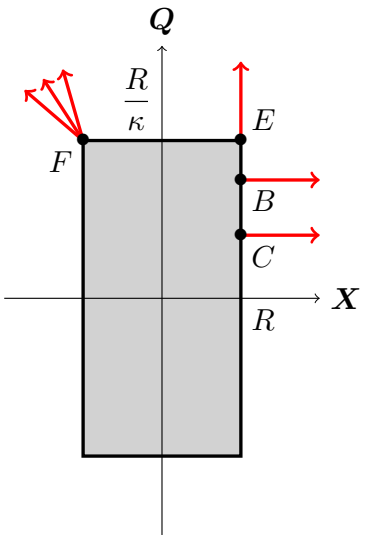

(a) Positions in the elastic domain corresponding to points B, C, E and F of Figure 5.5 and direction of the microscopic evolution.

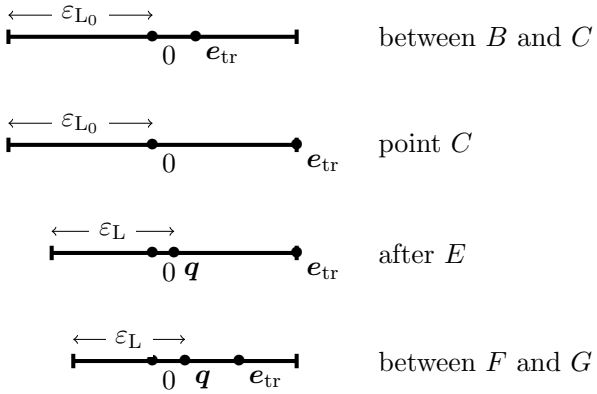

(b) Evolution of the microscopic domain during the cycle of Figure 5.4.

Figure 5.5: Scheme of the evolution of elastic and microscopic domain during the thermal cycle shown in Figure 5.4

We start from point A in the figure, corresponding to a stable austenitic configuration, and we apply a constant load s while we start lowering the temperature. Let us also suppose to work with a new material without any trace of fatigue, so that $\boldsymbol{e}_{\text{tr}} = \boldsymbol{q} = \boldsymbol{0}$. From (5.20) we can write the initial expression for X as

$$X = s - \beta\,(T - M_{\text{f}}).$$

The specimen stays in complete austenite until the beginning of the transformation, at temperature T_B. The evolution of $\boldsymbol{e}_{\text{tr}}$ starts when we reach the border of the elastic domain determined by ξ_∞ as displayed in Figure 5.5a. In particular, it corresponds to reaching $X = R$, so that we can determine T_B as follows:

$$X = s - \beta\,(T_B - M_{\text{f}}) = R \quad \Rightarrow \quad T_B = M_{\text{f}} + \frac{s - R}{\beta}. \tag{5.22}$$

This expression can be used for the experimental determination of the parameter β: since T_B is linear with respect to s, it is sufficient to measure T_B while varying s and look at the slope of the T_B *vs* s line.

After the beginning of the evolution for $\boldsymbol{e}_{\text{tr}}$, the two driving forces assume the following form

$$\begin{aligned} X &= s - h e_{\text{tr}} - \beta\,(T - M_{\text{f}}), \\ Q &= as + h e_{\text{tr}} + \beta\,(T - M_{\text{f}}). \end{aligned} \tag{5.23}$$

The microscopic transformation $\boldsymbol{e}_{\text{tr}}$ keeps on evolving until it reaches the maximum value ε_{L} (we recall that the general constrain is $|\boldsymbol{e}_{\text{tr}} - \boldsymbol{q}| \leq \varepsilon_{\text{L}}$, but $\boldsymbol{q}$ is null at the beginning of the transformation and it is not yet activated). The corresponding temperature T_C can be obtained by substituting $e_{\text{tr}} = \varepsilon_{\text{L}}$ in $X = R$

$$s - h\varepsilon_{\text{L}} - \beta(T_C - M_{\text{f}}) = R \quad \Rightarrow \quad T_C = M_{\text{f}} + \frac{s - R}{\beta} - \frac{h\varepsilon_{\text{L}}}{\beta} = T_B - \frac{h\varepsilon_{\text{L}}}{\beta}. \tag{5.24}$$

A measure of the maximum strain ε_{L} can be experimentally obtained by looking at the macroscopic strain that is reached so that, together with the previous estimate on β, the difference $T_C - T_B$ provides information on h. Point D can be used to measure the thermal expansion coefficient α since the only effect between points C and D is the volume change due to the variation of temperature (considerably smaller than both microscopic and macroscopic deformation).

The reverse transformation gives an idea of the parameters related to plasticity. A numerical information that we can obtain corresponds to the beginning of the evolution of $\boldsymbol{q}$ (point E), that is when $\boldsymbol{Q}$ reaches the boundary of the elastic domain as shown in Figure 5.5a, that is

$$Q = as + h\varepsilon_{\text{L}} + \beta\,(T_E - M_{\text{f}}) = \frac{R}{\kappa} \quad \Rightarrow \quad T_E = T_C + \frac{(1+\kappa)R - (1+a)\kappa s}{\beta\kappa}. \tag{5.25}$$

It is important to underline that this information can be deduced only by the numerical results while we do not have any experimental estimate of T_E. Actually, T_E is related only to the evolution of the internal variable $\boldsymbol{q}$, whose behavior we do not see on the macroscopical level provided by the experimental data.
As regards the beginning of the reverse transformation, a simple way to compute the corresponding temperatures consists in neglecting $\boldsymbol{q}$ under the assumption of $q \ll \varepsilon_{\mathrm{L}}$, thus easily obtaining the temperatures corresponding to point F and G. Point F indicates the moment in which the microscopic strain $\boldsymbol{e}_{\mathrm{tr}}$ starts decreasing. This happens when the corresponding driving force $\boldsymbol{X}$ reaches the border of the elastic domain whose normal has a negative horizontal component (see Figure 5.5a), that is $|\boldsymbol{X}| = R \Rightarrow X = -R$. Since when $\boldsymbol{e}_{\mathrm{tr}}$ starts decreasing we are at the maximum $e_{\mathrm{tr}} = \varepsilon_{\mathrm{L}}$ and we are neglecting q, we obtain

$$X = s - h\varepsilon_{\mathrm{L}} - \beta\left(T_C - M_{\mathrm{f}}\right) = -R \quad \Rightarrow \quad T_F = T_C + \frac{2R}{\beta}. \tag{5.26}$$

As regards G, it indicates to the complete return of e_{tr} to its referece value. Since we now have some fatigue, this ending point corresponds to the condition $e_{\mathrm{tr}} = q \neq= 0$. The corresponding temperature T_G is thus provided by

$$X = s - \beta\left(T_G - M_{\mathrm{f}}\right) = -R \quad \Rightarrow \quad T_G = T_B + \frac{2R}{\beta}. \tag{5.27}$$

We thus relate the width of the hysteresis loop $T_G - T_B$ (namely, $T_2 - T_1$ in the previous section) to the quantity $2R/\beta$, thus giving a measure of the radius of the elastic domain R.
It is interesting to notice that the hypothesis $q \ll \varepsilon_{\mathrm{L}}$ implies $T_G - T_F = T_B - T_C$, that is an identical width for the forward and the reverse transformation. The estimation of the parameters is completed by obtaining M_{f} through the use of the expression for T_B (known, like R, β and s).
Obviously, the values that we obtain through this process are only a first estimate of the actual values to be used. It is possible to start from these estimates for an optimization of the fitting and find even more suitable values for the model parameters.

5.3.3 Permanent effects

In section 5.2.1 we introduced the macroscopic plasticity as $\boldsymbol{e}_{\mathrm{pl}} = a\,\boldsymbol{q}$. This implies that after every thermal cycle that creates functional fatigue an increased macroscopic deformation $\boldsymbol{e}$ is induced. On the other hand, there are two factors that hinder this effect: first of all the evolution of the microscopic domain that introduces a stronger constraint on $\boldsymbol{e}_{\mathrm{tr}}$; second, the plastic hardening introduced through the parameter H. The

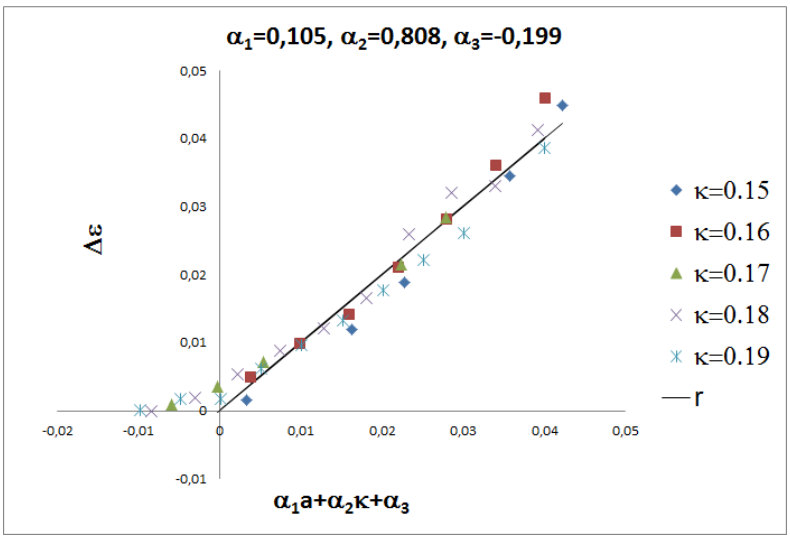

Figure 5.6: Plastic deformation as a function of the constitutive parameter a, for different values of κ. The remaining constitutive parameters are as in Figure 5.4.

consequence of this juxtaposition is that after a certain number of cycles the material approaches a balanced limit cycle (*training* effect [6, 60]).

There are two important parameters to be taken into account: a and κ. The former represents how much the microscopic plasticity induces a macroscopic one. The second corresponds to the ratio between the driving force that is necessary to induce microscopic fatigue and the one needed to obtain a microscopic transformation. Since it is easier to start the microscopic transformation evolution than to create plasticity, the value of κ is requested to be less than one in order to be physically acceptable.

The dependance of the plastic-induced deformation on these two parameters, a and κ, is shown in Figure 5.6. In particular, on the y-axis there is the difference $\Delta\epsilon$ between the uniaxial strain after the training, that is corresponding to a stationary regime, and the uniaxial strain in the first cycle. It is possible to notice that a good linear approximation seems to hold in the relation between $\Delta\epsilon$ and the couple (a,κ) but only after a threshold value under which there is no plastic effect. This suggests the existence of a bound for a and κ, that can be obtained by looking at the linear regression on the plot. Indeed, we have plastic effects only for $\alpha_1 a + \alpha_2\kappa + \alpha_3 \geq 0$, that in our case implies $a \geq a_{\text{thr}}$, with $a_{\text{thr}}(\kappa) = 1.9 - 7.7\kappa$. The values thus obtained may obviously depend on the other parameters so that a_{thr} should be computed for each case.

Analytically, it is possible to give some theoretical bounds for these plastic parameters. First of all, in section 5.3.2 we indicated by T_E the temperature at which the functional fatigue starts evolving and by T_G the temperature of the completed reverse

transformation. It is easy to understand that in the case $T_E > T_G$ it is impossible to activate the microscopic plasticity. Thus, it is crucial to require $T_E \leq T_G$, which implies the following *necessary* condition on a and κ

$$(1+a)\kappa s \geq (1-\kappa)R - h\kappa\varepsilon_{\mathrm{L}}. \tag{5.28}$$

At the same time, a *sufficient* condition for plasticity to occur can be provided by the request $T_E \leq T_F$, where T_F is the starting temperature of the reverse transformation. We thus obtain

$$(1+a)\kappa s \geq (1-\kappa)R. \tag{5.29}$$

The value we found for a_{thr} satisfies both conditions (by using the parameters listed in Figure 5.4).

The other important point in the introduction of permanent effects is represented by the irreversible evolution of the microscopic domain. In order to understand the influence of this part of the model, let us consider a slightly different experiment. We perform a first cycle with a constant positive load (as above) and afterwards an analogous cycle but with an identical and opposite load. We repeat this whole double-cycle twice.

The importance of this experiment is that at the end of such a double-cycle the functional fatigue $\boldsymbol{q}$ can simply return to the initial zero value. Indeed, the pushing process completely cancel the previous pulling one. In the case of a constant microscopic domain, this implies that the second double-cycle has no memory of the first one, since at its beginning every variable is back to the initial value. By varying the microscopic domain, though at the end of the first cycle all the variables are back to the initial condition, there still is a memory of the previous transformation in the contracted domain. In order to notice this effect, let us look at Figure 5.7. On the horizontal axis there is a linear combination of κ and of the applied load s. On the vertical axis there is the difference between the maximum uniaxial strain during the first cycle and during the second one.

First of all, it is possible to notice that the variation in the strain between the second complete cycle and the first one is always negative, that is the maximum strain that we are able to reach in the second case is lower. This is due to the shrinking of the microscopic domain. As already explained, the maximum strain that we can obtain corresponds to the parameters ε_{L} and, actually, the only effect we retain after the first load-unload cycle is a decreasing in ε_{L}. This explains why during the second cycle we cannot obtain higher maximum strain values. The quantity of lost strain from one cycle to the other one is then related to the decreasing in ε_{L} that we assumed to be directly

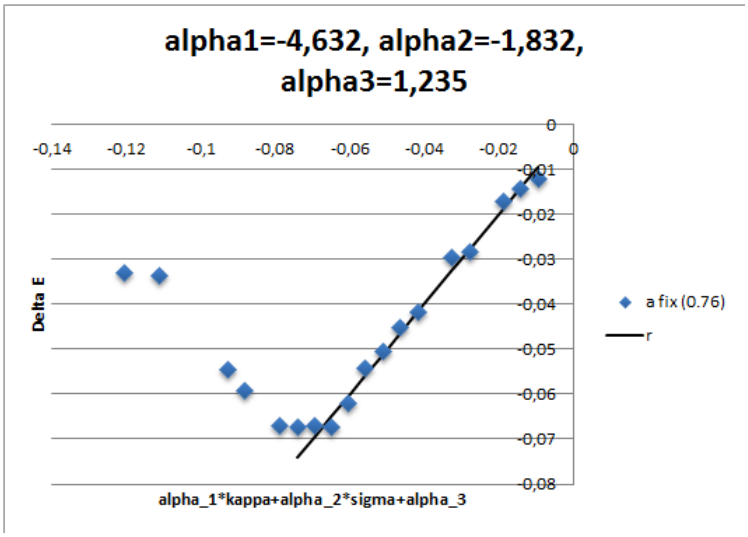

Figure 5.7: Lost strain deformation as a function of the constitutive parameter κ and the load s, for $a = 0.76$. The remaining constitutive parameters are as in Figure 5.4.

correlated to the (negative and positive) variations of the fatigue functional $\boldsymbol{q}$ in Section 5.2.2. Bigger variations $\dot{\boldsymbol{q}}$ correspond to bigger values for the parameter κ (the derivative $\partial\xi/\partial\boldsymbol{Q}$ is always proportional to κ for all the proposed choices of ξ) and the load s (higher s means higher $\boldsymbol{Q}$ and $\partial\xi/\partial\boldsymbol{Q}$ is proportional to $\boldsymbol{Q}$ when closing ξ_2 and ξ_∞.) Since the variation of strain has the same behavior for both κ and $\boldsymbol{q}$, we obtain the same sign for the coefficients of the linear regression α_1 and α_2. Moreover, bigger negative values of the strain variation correspond to bigger positive values of κ and s and this explains the negative sign for both the coefficients.

5.4 Comparison with experimental data

Here we test our numerical predictions by comparing them with some experimental results: a thermal-induced transformation and a stress-induced one.

5.4.1 Thermally-induced hysteresis

The data of the thermally-induced experiment were collected in the SAES Getters Laboratories by testing a $Ti_{51}Ni_{49}$ SMA wire with a diameter of $75\,\mu$m. A linear motor controlled in close loop by a load cell applies a constant uniaxial stress of 360 MPa at the extremities of the wire [97]. The cycle starts from high temperature corresponding to complete austenite. The experiment is performed as described in section 5.3.1, by cooling and then heating again the wire. The temperature is varied through an electric current induced in the wire and controlled by using a thermographic camera.

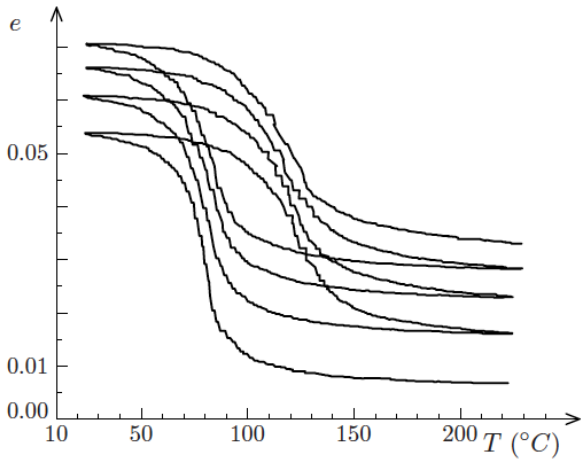

Figure 5.8: Experimental results for a TiNi micro-wire, subject to a thermal cycle under a constant uniaxial load, as specified in the text.

Figure 5.8 shows the hysteresis loop obtained by plotting experimental strain versus temperature. It is possible to notice the increasing of the maximum strain corresponding to repeated cycles and the saturation of this quantity after a certain number of transformations. This behavior proves the importance of the plastic deformation $a\boldsymbol{q}$ in the Helmholtz potential. On the other hand, it is not possible to see the effects of the evolution of the microscopical transformation domain since its influence on the outcomes is evident above all when a double-loading cycle is performed, as explained in section 5.3.3.

We calibrated the parameters of the model in order to reproduce the first loop in Figure 5.8. We fix the uniaxial external load and we already know the material parameters for bulk and shear moduli, together with an estimate of the martensite finish temperature M_{f}. This estimate allows the further use of (5.22) for the determination of R and β since we have measures only for a value of the external load and we cannot use the technique suggested in 5.3.2 that requires a T_B *vs* s curve. The calibration can thus be done in the following way: ε_{L} and the main temperatures T_B, T_C and T_F can be estimated from the plot of the experimentally obtained hysteresis loop. By using the expressions for these quantities as shown in 5.3.2, it is possible to estimate R, β and h. Finally, a, κ and H can be obtained by fitting the experimental data, paying attention to the necessary condition (5.28). The result of this process and the different nature of the estimate of the parameters is shown in Table 5.1.

In Figure 5.9 the comparison between the numerical and the experimental curve is

Parameter	Value	Method
K	60.7 GPa	Known
G	23.3 GPa	Known
M_{f}	296°K	Known
ε_{L}	0.0595	Estimated
R	60.6 MPa	Computed
β	3.03 MPa/°K	Computed
h	510 MPa	Computed
a	0.20	Fitted
κ	0.25	Fitted
H	3.7 GPa	Fitted

Table 5.1: Values of the constitutive parameters used in Figure 5.9.

shown. We can notice a good qualitative agreement but at the same time it seems not possible to obtain a complete match between the two loops.
We can also try to estimate a goodness-of-fit indicator: we interpolate both the experimental data and the numerical ones on a set of N points thus obtaining respectively $\boldsymbol{y}^{\mathrm{exp}}$ and $\boldsymbol{y}^{\mathrm{fit}}$. We complete by computing

$$g = 1 - \frac{1}{N} \sum_{i=1}^{N} \frac{|y_i^{\mathrm{exp}} - y_i^{\mathrm{fit}}|}{y_i^{\mathrm{exp}}}. \tag{5.30}$$

A good fit corresponds to values of g close to one while the closer we are to zero the worse the fit has to be considered. For Figure 5.9 we obtain $g = 0.895$, thus quantifying a good qualitative fit though we do not have a perfect match. This problem is obviously due to the assumptions on which the model is based, in particular the homogeneity hypothesis. Actually, not only the wire is not homogeneous because of the presence of defects and different grain structure, but also the microscopical transformation does not occur in a homogeneous way. It is likely going to take place through domain creation and growth, thus not at the same time in all the wire.
The experimental non-homogeneity that concerns the microscopical transformation $\boldsymbol{e}_{\mathrm{tr}}$ also affects $\boldsymbol{q}$. Indeed, experimental evidence suggests that plasticity usually starts close to fixed boundary conditions were the specimen is particularly constrained.

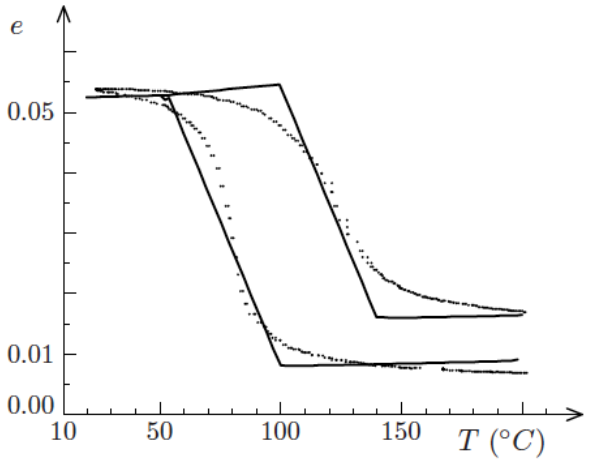

Figure 5.9: Comparison of experimental (points) and theoretical (line) results for the first cycle of the TiNi microwire illustrated in Figure 5.8, with the constitutive parameters described in the text.

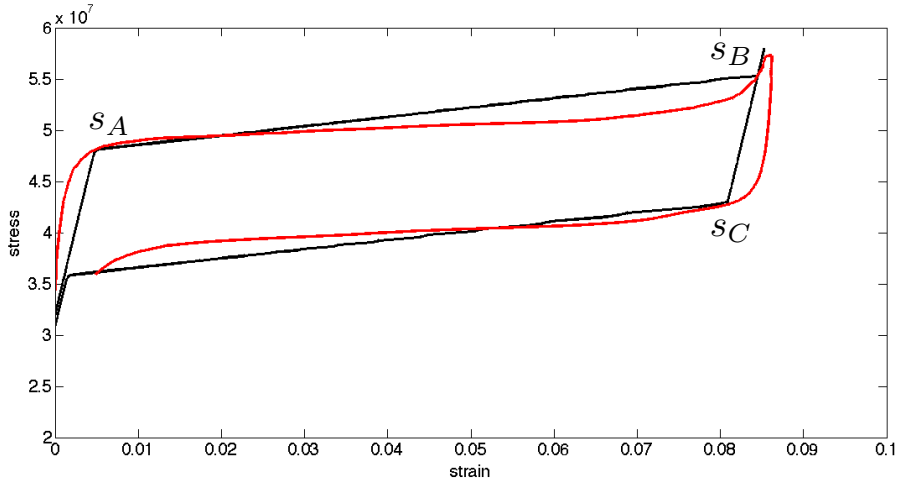

Figure 5.10: Comparison of experimental (red) and theoretical (black) results for the stress-controlled test detailed in section 2.1.2. The constitutive parameters are obtained as described in the text: $K = 1.53$GPa, $G = 1.5$GPa, $\alpha = 10^{-5}/°$K, $\beta = 2.71$MPa/°K, $h = 62$MPa, $H = h$, $\varepsilon_L = 9.5 \times 10^{-2}$, $R = 5$MPa, $\kappa = 0.001$, $a = 0.9$, $M_f = 330°$K.

5.4.2 Stress-induced hysteresis

The same kind of reasoning as in section 5.4.1 can be done for another kind of experiment, for example in the case of a stress-induced transformation instead of the temperature-induced one. In this section, we describe how to choose the parameters of the model to reproduce the outcome of the experiment detailed in section 2.1.2. The hysteresis loop that we want to numerically obtain is shown in Figure 3.2 in section 3.1.2. In a few words, the experiment consists in loading the specimen with an increasing uniaxial stress at a constant temperature, thus inducing the austenite-martensite transition. Afterwards, the specimen is unloaded again and returns to the initial state.

Since in this case there is no interest in the development of plasticity, let us suppose to have a functional fatigue $\boldsymbol{q}$ which is negligible with respect to the transformation strain $\boldsymbol{e}_{\text{tr}}$. This assumption corresponds to choosing a small value for the parameter κ which defines the scaling between the transformation and the fatigue. Moreover, it implies that we can assume ε_{L} to be constant. We also assume $T > M_{\text{f}}$ since the test is performed at room temperature, at which the specimen is austenitic. The quantity $\beta\langle T - M_{\text{f}}\rangle$ is actually constant and does not play an important role in this kind of experiment.

We initially know T, M_{f}, K and G. Let us choose the dissipation function ξ_1 in section 5.2.3 (the computation is easily doable for the other choices of the dissipation function). Since in this case the varying variable is stress instead of temperature, we use the estimate of stresses corresponding to characteristic points in the experimental plot to infer the relations between the parameters. The same symmetry as in section 5.3.1 holds so that we can use 5.20 and 5.21 to write down the form of the elastic domain

$$|(1+\kappa\, a)\, s - (1-\kappa)\, h\, (e_{\text{tr}} - q) - H\, q + \beta(T - M_{\text{f}})| \leq R. \tag{5.31}$$

At the beginning of the loading phase the deformation is only elastic, with $e_{\text{tr}} = q = 0$ until we reach point A_s in Figure 5.10 and the microscopic transformation begins. This means that we have reached the boundary of the elastic domain (*i.e.* equality holds in 5.31) and we obtain

$$s_A = \frac{R + (1-\kappa)\beta(T - M_{\text{f}})}{1 + a\,\kappa}. \tag{5.32}$$

As stated in section 5.2.3, the choice of ξ_1 implies a coupled evolution for the two internal variables of the kind

$$q = \kappa e_{\text{tr}},$$

so that the evolution of both is determined by satisfying

$$(1+\kappa\, a)\, s - [(1-\kappa)^2\, h + \kappa^2\, H]\, e_{\text{tr}} - (1-\kappa)\beta(T - M_{\text{f}}) = R. \tag{5.33}$$

The plateau ends (point B_s in Figure 5.10) when the transformation reaches its maximum, that is ε_{L}. The corresponding stress s_B is thus obtained by imposing $e_{\mathrm{tr}} = \varepsilon_{\mathrm{L}}$ in 5.33.
The following interesting point corresponds to the beginning of the reverse transformation (point s_C). At this point, the microscopic strain is equal to ε_{L} and the opposite side of the elastic domain is reached, that is

$$(1+\kappa\, a)\, s_C - [(1-\kappa)^2\, h + \kappa^2\, H]\, \varepsilon_{\mathrm{L}} - (1-\kappa)\beta(T - M_{\mathrm{f}}) = -R. \tag{5.34}$$

By subtracting 5.34 to 5.33 we obtain a relation to compute R, that is

$$s_B - s_C = \frac{2R}{1+\kappa\, a}.$$

The knowledge of R allows for the computation of β by using 5.32. At the same time, by subtracting 5.32 to 5.33 we obtain

$$s_B - s_A = \frac{((1-\kappa)^2 h + \kappa^2 H)\varepsilon_{\mathrm{L}}}{1+\kappa\, a},$$

depending only on h and H. Let us assume to have $H = h$ (having required small values for κ and being h and H of the same order we could also neglect the H-term). The difference between the stress at the end and at the beginning of the plateau thus provides an estimate for h.
As in the temperature-driven case in section 5.4.1, it is possible to estimate the goodness of the numerical fit by using (5.30) and obtaining $g = 0.97$. Also in this case, the homogeneity assumption makes the numerical curve slightly different from the experimental one, though in qualitative agreement. Actually, the results shown in Section 3.1.2 prove that the trasformation is definitely non homogenous. Moreover, we are approximating a basically two-dimensional object (the experimental specimen described in section 2.1.1) with a one-dimensional geometry, thus obviously inducing a further difference between experimental and numerical results.

5.5 Conclusions

In the last chapter we showed a macroscopic theory that establishes a further step in describing functional fatigue in Shape Memory Alloys.
The hypothesis at the basis of our model are the presence of small strains and the homogeneity of the material. Though these hypothesis are quite strong, the model is able to reproduce the overall behavior of the material. This is proven by comparing the model results with some experimental data, both for temperature-induced transformations and

for stress-induced ones. The numerical results have been obtained by solving the essentially three-dimensional model in a one-dimensional approximation. In this case, the simplicity of the model equations allows for a calibration of the parameters through some analytical consideration.
Thus, the model is able to catch the features of the martensitic transition from a macroscopic point of view when varying the material composition and the loading conditions. In this sense, this theory adds a further knowledge of the martensitic transformations to the experimental and statistical descriptions of the previous chapters.

Conclusions and Future Work

In this thesis we provided an analysis of martensitic transformations from different points of view.
We combined an experimental device with a technique for the treatment of data that gave us different kinds of information: from classical macroscopical results to the proof of the presence of intermittency in our transformation. Alongside this experimental study, we put a macroscopic mathematical model for the investigation of arising of fatigue in shape memory alloys.

All these results are tiles in the knowledge of martensitic transformations and shape memory alloys. By consequence, there are several possible developments to take into account.
For starters, it would be interesting to have a microscopic mathematical model to numerically reproduce our test. This would provide further information on some aspects of the transformation, like the favorite martensite variant or the detection of avalanches within the specimen, not only on the surface.
We are currently working on a microscopic model for the description of intermittent behavior. The basic idea consists in combining the crystallographic theory introduced in Section 1.2 and the literature on automaton-type models [71, 72, 82]. In order to provide some information on intermittency, the model has to work at the spatial scale of the crystal and at a temporal scale slower than the loading. The idea behind automaton models is that a certain variable, for example the transformation gradient, in a certain point can have only a finite number of values (in our case, the identity for the austenite and the Bain matrices of the martensite variants). The means of crystallographic theory can be used to choose the actual value of the variable for each point, for example by

minimizing a suitable energy density for a fixed external load. By iterating this step, the model takes into account for consecutive changes due to the influence of the neighboring points, thus providing the evolution of the strain events.

From the experimental point of view, within the same experimental setting there still are many other tests that can and should be done in order to improve the results. A more specific tuning of the loading rates should be done to check the actual quasi-staticity of the process, together with a study on the image acquisition rates. Moreover, shorter loading-unloading cycles could be performed to test the rate-indipendency.

Finally, the mathematical model could be combined with a wider experimental analysis by using our experimental techniques together with other methods that have already been used for SMAs, like acoustic emission or calorimetry and thermography for the measurement of local heat sources. In this way, we could conciliate the acoustic, the spatial and the energetic descriptions of the transformation, thus obtaining an even more accurate characterization.

Bibliography

[1] R. Abeyaratne, J.K. Knowles: *A continuum model of a thermoelastic solid capable of undergoing phase transitions*. Journal of the Mechanics and Physics of Solids **41** (1993), 541-571.

[2] F. Anscombe:*The transformation of poisson binomial and negativebinomial data*. Biometrika **35** (1948), 246–254.

[3] G. Attanasi, F. Auricchio, and M.F. Urbano: *Theoretical and Experimental Investigation on SMA Superelastic Springs*. J. Mater. Eng. Perform. **20** (2011), 706-711.

[4] F. Auricchio and E. Bonetti: *A new flexible 3D macroscopic model for shape memory alloys*. Discrete and continuous dynamical system series S **6** (2013), 277-291.

[5] F. Auricchio, A. Coda, A. Reali, and M.F. Urbano: *SMA Numerical Modeling Versus Experimental Results: Parameter Identification and Model Prediction Capabilities*. J. Mater. Eng. Perform. **18** (2009), 649-654.

[6] F. Auricchio, S. Marfia, and E. Sacco: *Modelling of SMA materials: Training and two way memory effects*. Comp. Struct. **81** (2003), 2301-2317.

[7] F. Auricchio and L. Petrini: *A three-dimensional model describing stress-temperature induced solid phase transformations: thermomechanical coupling and hybrid composite applications*. Int. J. Numer. Meth. Engng **61** (2004), 716-737.

[8] F. Auricchio and L. Petrini: *A three-dimensional model describing stress-temperature induced solid phase transformations: solution algorithm and boundary value problems*. Int. J. Numer. Meth. Engng **61** (2004), 807-836.

[9] F. Auricchio, A. Reali, and U. Stefanelli: *A three-dimensional model describing stress-induced solid phase transformation with permanent inelasticity*. Int. J. Plasticity **23** (2007), 207-226.

[10] C. Badulescu, M. Grédiac, J. D. Mathias, D. Roux, *A Procedure for Accurate One-Dimensional Strain Measurement Using the Grid Method*. Experimental mechanics **49** (2009), 841-854.

[11] C. Badulescu, M. Grédiac, J. D. Mathias, *Investigation of the grid method for accurate in-plane strain measurement*. **20** (2009).

[12] X. Balandraud and G. Zanzotto: *Stressed microstructures in thermally induced M*9*R–M*18*R martensites*. Journal of the Mechanics and Physics of Solids **55** (2007), 194-224.

[13] X. Balandraud, D. Delpueyo, M. Grédiac, G. Zanzotto, Almost compatible microstructures in shape memory alloys, Acta Materialia, Vol. 58, 4559-4577, 2010.

[14] J.M. Ball and R.D. James: *Fine phase mixture as minimizers of energy*. Arch. Ration. Mech. An. **100** (1987), 13-52.

[15] J, Baró and E. Vives: *Analysis of power-law exponents by maximum-likelihood maps*. Physical Review E **85**, 066121 (2012).

[16] J. Baró, J.M. Martín-Olalla, F.J. Romero, M.C. Gallardo, E.K.H. Salje, E. Vives and A. Planes: *Avalanche correlations in the martensitic transition of a Cu–Zn–Al shape memory alloy: analysis of acoustic emission and calorimetry*. J. Phys. Condens. Matter **26** (2014), 125401.

[17] N. Barrera, P. Biscari and M.F. Urbano: *Macroscopic modeling of functional fatigue in Shape Memory Alloys*. European Journal of Mechanics - A/Solids (2013).

[18] K. Bhattacharya: *Self-Accommodation in Martensite*. Arch. Rational Mech. Anal. **120** (1992), 201-244.

[19] K. Bhattacharya: *Microstructure of martensite: Why it forms and how it gives rise to the shape memory effect?*. Ed. Oxford University Press (2003).

[20] K. Bhattacharya, S. Conti, G. Zanzotto, and J. Zimmer: *Crystal symmetry and the reversibility of martensitic transformations*. Nature **428** (2004), 55-59.

[21] K. Bhattacharya and R.D. James: *The material is the machine*. Science **307** (2005), 53-54.

[22] E. Bonnot, R. Romero, X. Illa, L. Mañosa, A. Planes and E. Vives: *Hysteresis in a system driven by either generalized force or displacement variables: Martensitic phase transition in single-crystalline CuZnAl*. Phys. Rev. B **76** (2008).

[23] L. Carrillo, J. Ortín: *Avalanches in the growth of stress-induced martensite*. Phys. Rev. B **56** (1997).

[24] P.O Castillo-Villa, J. Baró, A. Planes, E.K.H. Salje, P. Sellappan, W.M. Kriven and E. Vives:*Crackling noise during failure of alumina under compression: the effect of porosity*. J. Phys.: Condens. Matter **25**, 292202 (2013).

[25] L-Q. Chen: *Phase-field models for microsctructure evolution*. Annual Review of Materials Research **32** (2002), 113-140.

[26] A. Chrysochoos and Y. Surrel, Chapter 1: Basics of metrology and introduction to techniques. In: M. Grédiac, F. Hild (eds) *Full-field measurements and identification in solid mechanics*. Wiley (2012), 1-29.

[27] A. Clauset, C. Rohilla Shalizi: *Power-law distributions in empirical data*. eprint arXiv:0706.1062 (2007).

[28] P. Colli, M. Frémond and A. Visintin: *Thermo-mechanical evolution of shape memory alloys*. Quarterly of applied mathematics **48** (1990), 31-47.

[29] S. Conti and G. Zanzotto: *A variational model for reconstructive phase transformations in crystals, and their relation to dislocations and plasticity*. Arch. Rational Mech. Anal. **173** (2004), 69–88.

[30] D. Delpueyo, X. Balandraud, M. Grédiac, Applying infrared thermography to analyse martensitic microstructures in a Cu-Al-Be shape-memory alloy subjected to a cyclic loading, Materials Science and Engineering A, Vol. 528, 8249-8258, 2011

[31] D. Delpueyo, M. Grédiac, X. Balandraud, C. Badulescu, Investigation of martensitic microstructures in a monocrystalline Cu-Al-Be shape memory alloy with the grid method and infrared thermography, Mechanics of Materials, Vol. 45, 34-51, 2012

[32] D. De Tommasi, N. Millardi, G. Puglisi and G. Saccomandi: *An energetic model for macromolecules unfolding in stretching experiments*. J R Soc Interface **10** (2013), 20130651.

[33] G. Durin, S. Zapperi: *The role of stationarity in magnetic crackling noise*. Journal of Statistical Mechanics (2006).

[34] K.R. Elder and M. Grant: *Modeling elastic and plastic deformations in nonequilibrium processing using phase field crystals*. Phys. Rev. E **70** (2004), 051605.

[35] EMVA standard 1288: *Standard for characterization of image sensors and cameras*. Release 3.0 Eur. Mach. Vis. Assoc. (2010).

[36] J.L. Ericksen: *Special topics in elastostatics*. Adv. Appl. Mech **17** (1977), 189-244.

[37] J.L. Ericksen: *Symmetry of deformable crystals*. Arch. Rat. Mech. Anal. **72** (1979), 1-13.

[38] J.L. Ericksen: *The Cauchy and Born hypothesis for crystals*. In M.E. Gurtin *Phase Transformations and Material Instabilities in Solids*, Academic Press (1984), 61-78.

[39] S. Eucken and T.W. Duerig: *The effects of pseudoelastic prestraining on the tensile behaviour and two-way shape memory effect in aged NiTi*. Acta Metallurgica **37** (1989), 2245–2252.

[40] B. Fedelich and G. Zanzotto: *Hysteresis in discrete systems of possibly interacting elements with a double-well energy*. J. Nonlinear Sci. **2** (1992), 319-342.

[41] A. Foi, M. Trimeche, V. Katkovnik and K. Egiazarian: *Practical poissonian-gaussian noise modeling and fitting for single-image raw-data*. IEEE Trans. Image Process.**17** (2008), 1737–1754.

[42] M. Frémond: *Matériaux à mémoire de forme*. Comptes rendus de l'Académie des sciences. Série 2, Mécanique, Physique, Chimie, Sciences de l'univers, Sciences de la Terre **304** (1987), 239-244.

[43] M.C. Gallardo, J. Manchado, F.J. Romero, J. del Cerro, E.K.H. Salje, A. Planes, E. Vives, R. Romero and M. Stipcich: *Avalanche criticality in the martensitic transition of* $Cu_{67.64}Zn_{16.71}Al_{15.65}$ *shape-memory alloy: a calorimetric and acoustic emission study*. Physical Review B **81** (2010), 174102.

[44] P. Germain, Q.S. Nguyen and P. Suquet: *Continuum thermodynamics*. Journal of Applied Mechanics **50** (1983), 1010-1020.

[45] M. Grédiac, F. Sur, C. Badulescu and J.D. Mathias: *Using deconvolution to improve the metrological performance of the grid method*. Optics and Lasers in Engineering **51** (2013), 716-734.

[46] M. Grédiac and F. Sur: *50th Anniversary Article: Effect of Sensor Noise on the Resolution and Spatial Resolution of Displacement and Strain Maps Estimated with the Grid Method*. Strain **50** (2014) 1475-1305.

[47] M. E. Gurtin, E. Fried and L. Anand: *The mechanics and thermodynamics of continua*. Cambridge University Press, 2010.

[48] G. Healey and R. Kondepudy: *Radiometric CCD camera calibration and noise estimation*. IEEE Trans. Patt. Anal. Mach. Intell.**16**, (1994), 267-276.

[49] R. J. Harrison and E. K. H. Salje: *The noise of the needle: Avalanches of a single progressing needle domain in LaAl03*. Appl. Phys. Lett. **97** (2010).

[50] D.J. Hartl and D.C. Lagoudas: *Constitutive modeling and structural analysis considering simultaneous phase transformation and plastic yield in shape memory alloys*. Smart Mater. Struct. **18** (2009), #104017.

[51] E. Hornbogen: *Thermo-mechanical fatigue of shape memory alloys*. J. Mater. Sci. **39** (2004), 385-399.

[52] Y. Huo and I. Müller: *Nonequilibrium Thermodynamics of Pseudoelasticity*. Continuum Mech. Thermodyn. **5** (1993),163-204.

[53] J. James, K. Hane: *Martensitic transformations and shape memory materials*. Acta Mat. **48** (2000), 197–222.

[54] A.G. Khachaturyan: *Theory of structural transformations in solids*. John Wiley and Sons (1983).

[55] D.C. Lagoudas: *Shape Memory Alloys: Modeling and Engineering Applications*. Ed. Springer-Verlag (2008).

[56] S. Leclercq and C. Lexcellent: *A general macroscopic description of the thermomechanical behavior of shape memory alloys*. J. Mech. Phys. Solids **44** (1996), 953-980.

[57] J. Lemaitre, D. Marquis: *Modeling complex behavior of metals by ´´State-Kinetic Coupling Theory"*. J. Eng. Mater. Technol. **114** (1992), 250-254.

[58] C. Lexcellent, P. Robinet, J. Bernardini, D. Beke and P. Olier: *High temperature creep measurements in equiatomic Ni–Ti shape memory alloy*. Materialwissenschaft und Werkstofftechnik **36** (2005), 509–512.

[59] C. Lexcellent: *Shape-Memory Alloys Handbook*. Wiley-ISTE (2013).

[60] Yi. Liu, Yo. Liu, and J. Van Humbeeck: *Two-way shape memory effect developed by martensite deformation in NiTi*. Acta mater. **47** (1999), 199-209.

[61] J.J. Moreau: *Application of convex analysis to the treatment of elastoplastic systems*. Lecture Notes in Mathematics **503** (1976), 56-89.

[62] J.J. Moreau: *Evolution problem associated with a moving convex set in a Hilbert space*. Journal of Differential Equations **26** (1977), 347-374.

[63] I. Müller and H.Xu: *On the pseudo-elastic hysteresis*. Acta Met. et Mater. **39** (1991), 263-271.

[64] I. Müller and S. Seelecke: *Thermodynamic aspects of shape memory alloys*. Mathematical and Computer Modelling **34** (2001), 1307-1355.

[65] F. Murthagh, J. Starck and A. Bijaoui:*Image restoration with noise suppression using a multiresolution support*. Astron. Astrophys. **112** (1995), 179-189.

[66] G.F. Nataf, P.O. Castillo-Villa, J. Baró, X. Illa, E. Vives, A. Planes and E.K.H. Salje: *Avalanches in compressed porous SiO2-based materials*. Physical Review E **90**, 022405 (2014).

[67] R. Niemann, J. Baró, O. Heczko, L. Schultz, S. Fähler, E. Vives, L. Mañosa, and A. Planes: *Tuning avalanche criticality: Acoustic emission during the martensitic transformation of a compressed Ni-Mn-Ga single crystal*. Physical Review B **86**, 214101 (2012).

[68] R. Niemann, J. Kopeček, O. Heczko, J. Romberg, L. Schultz, S. Fähler, E. Vives, L. Mañosa, and A. Planes: *Localizing sources of acoustic emission during the martensitic transformation*. Phys. Rev. B **89** (2014), 214118.

[69] J. Notbohm, A. Rosakis, S. Kumagai, S. Xia and G. Ravichandran: *Three-dimensional displacement and shape measurement with a diffraction-assisted grid method*. Strain **49** (2013), 399–408.

[70] K. Otsuka, C.M. Wayman: *Shape memory materials*. Cambridge University Press, Cambridge, (1998).

[71] F.J. Perez-Reche, L. Truskinovsky and G. Zanzotto: *Plasticity mediated criticality in martensites*. Phys. Rev. Lett. **99** (2007), 075501.

[72] F.J. Perez-Reche, L. Truskinovsky and G. Zanzotto: *Martensitic transformations: from continuum mechanics to spin models and automata*. Continuum Mechanics and Thermodynamics **21** (2009), 17-26.

[73] R. Peyroux, A. Chrysochoos, C. Licht, M. Lobel:*Thermomechanical couplings and pseudoelasticity of shape memory alloys*. Int J Eng Sci **36** (1998), 489.

[74] J. L. Piro, M. Grédiac: *Producing and transferring low-spatial frequency grids for measuring displacement fields with Moiré and grid methods*

[75] M. Pitteri and G. Zanzotto: *Continuum Models for Phase Transitions and Twinning in Crystals*. Ed. Chapman & Hall (2003).

[76] G. Puglisi and L. Truskinovsky: *Rate independent hysteresis in a bi-stable chain*. Journal of the Mechanics and Physics of Solids **50** (2002), 165–187.

[77] G. Puglisi and L. Truskinovsky: *Thermodynamics of rate-independent plasticity*. Journal of Mechanics and Physics of solids **53** (2005), 655–679.

[78] G. Puglisi: *Nucleation and phase propagation in a multistable lattice with weak nonlocal interactions*. Continuum Mech. Thermodyn. **19** (2007), 299–319.

[79] K.R. Rajagopal and A.R. Srinivasa: *Mechanics of the inelastic behavior of materials – Part I, Theoretical underpinnings*. Int. J. Plasticity **14** (1998), 945-967.

[80] K.R. Rajagopal and A.R. Srinivasa: *Mechanics of the inelastic behavior of materials – Part II, Inelastic response*. Int. J. Plasticity **14** (1998), 969-995.

[81] E.K.H. Salje, J. Koppensteiner, M. Reinecker, W. Schranz and Antoni Planes: *Jerky elasticity: Avalanches and the martensitic transition in* $Cu_{74.08}$ $Al_{23.13}$ $Be_{2.79}$ *shape-memory alloy*- Applied Physics Letters **95** (2009), 231908.

[82] O.U. Salman and L. Truskinovsky: *Minimal integer automaton behind crystal plasticity*. Phys. Rev. Lett. **106** (2011), 175503.

[83] U. O. Salman, A. Finel, R. Delville, D. Schryvers: *The role of phase compatibility in martensite*. J. Appl. Phys. textbf111 (2012).

[84] P. Schlosser, D. Favier, H. Louche and L. Orgéas: *Experimental characterization of NiTi SMAs thermomechanical behaviour using temperature and strain full-field measurements*. Advances in Science and Technology **59** (2008), 140-149.

[85] J.P. Sethna, K.A. Dahmen and C.R. Myers: *Crackling noise*. Nature **410** (2001).

[86] J.A. Shaw and S. Kyriakides: *Thermomechanical aspects of NiTi*. Journal of the Mechanics and Physics of Solids **43** (1995), 1243-1281.

[87] J.A. Shaw and S. Kyriakides: *On the nucleation and propagation of phase transformation fronts in a NiTi alloy*. Acta Materialia **45** (1997), 683-700.

[88] T. W. Shield: *Orientation Dependence of the Pseudoelastic Behavior of Single Crystals of CuAlNi in Tension*. J. Mech. Phys. Solids **93** (1995), 869-895.

[89] Y. Song, X. Chen, V. Dabade, T.W. Shield, R.D. James: *Enhanced reversibility and unusual microstructure in a phase-transforming material*. Nature **502** (2013), 85-88.

[90] A.C. Souza, E.N. Mamiya, and N. Zouain: *Three-dimensional model for solids undergoing stress-induced phase transformations*. Eur. J. Mech. A/Solids **17** (1998), 789-806.

[91] Surrel Y., Photomechanics. Vol. 77 of Topics in Applied Physics, Springer, Chapter Fringe analysis, 55-102, 2000.

[92] F. Sur and M. Grédiac: *Sensor Noise Modeling by Stacking Pseudo-Periodic Grid Images Affected by Vibrations*. IEEE Signal Processing Letters, **21** (2014), 432-436.

[93] F. Sur and M. Grédiac: *Towards deconvolution to enhanced the grid method for in-plane strain measurement*. Inverse Problems and Imaging, American Institute of Mathematical Sciences **8** (2014), 259-291.

[94] F. Sur and M. Grédiac: *On noise reduction in strain maps obtained with the grid method by averaging images affected by vibrations*. Optics and Lasers in Engineering **66** (2015), 210-222.

[95] K. Tanaka, F. Nishimura, M. Matsui, H. Tobushi and P-H. Lin: *Phenomenological analysis of plateaus on stress-strain hysteresis in TiNi shape memory alloy wires*. Mechanics of Materials **24** (1996), 19-30.

[96] L. Truskinovsky and G. Zanzotto: *Mechanics of crystals with a triple points*. J. Mech. Phys. Solids. **50** (2002), 189-215.

[97] M. Urbano, A. Coda, and R. Giannantonio: *SMAq: A novel integrated instrument for the characterization of SMA wires*. SMST 2006 (Int. Conf. on Shape Memory and Superelastic Technologies) Proceedings. Ed. B. Berg, M.R. Mitchell, and J. Proft (2008), 177-184.

[98] M.F. Urbano: *Study of the Influence of Inclusions on the Behavior of NiTi Shape-Memory Alloys in Thermal Cycling by Means of Finite Element Method*. Metall. Mater. Trans. A **43** (2012), 2912-2920.

[99] J. Van Humbeeck: *Cycling effects, fatigue and degradation of shape memory alloys*. J. Phys. IV France **1** (1991), 189-197.

[100] E. Vives, I. Ráfols, L. Mañosa, J. Ortín, A. Planes: *Statistics of avalanches in martensitic transformations. I. Acoustic emission experiments*. Phys. Rev. B **52** (1995)

[101] E. Vives, D. Soto-Parra, L. Mañosa, R. Romero and A. Planes: *Driving-induced crossover in the avalanche criticality of martensitic transitions*. Phys. Rev. B **80** (2009).

[102] E. Vives, D. Soto-Parra, L. Mañosa, R. Romero and A. Planes: *Imaging the dynamics of martensitic transitions using acoustic emission*. Phys. Rev. B **84** (2011), 060101.

[103] Y. Wang and A.G. Khachaturyan: *Three-dimensional field model and computer modeling of martensitic transformations*. Acta materialia, **45** (1997), 759-773.

[104] C.M. Wayman: *Introduction to the Crystallography of Martensitic Transformations*. Macmillan, New York (1977).

[105] A. Zanzottera, Ph.D. Thesis, Politecnico di Milano, Italy (2014).

[106] G. Zanzotto: *The Cauchy-Born Hypothesis, Nonlinear Elasticity and Mechanical Twinning in Crystals*. Acta Cryst. A **52** (1996), 839-849.

[107] Z. Zhang, R.D. James and S. Müller: *Energy barriers and hysteresis in martensitic phase transformations*. Acta Mater. **57** (2009), 4332-4352.

Aknowledgements

I would like to express my deep gratitude to Professor Paolo Biscari, that has fully encouraged and motivated me for all these years, since my first approach to Continuum Mechanics. In the same way, I would like to thank Professor Xavier Balandraud, who has introduced me to the wonders of Experimental Mechanics and has shown me a different point of view to look from.
I am particularly grateful to Professor Giovanni Zanzotto and Professor Michel Grédiac, for their priceless help in many occasions, through frequent and inspiring conversations.
My special thanks are extended to Doctor Marco Urbano, who has closely followed my first steps in the world of Shape Memory Alloys.
I also wish to thank Doctor Anna Zanzottera, for the constant help and the fruitful discussions.
I would like to sincerely thank all these people for having supported me with enthusiasm and curiosity during this experience.

Finally, I wish to thank my parents and my sister for their unceasing assistance throughout my study.